# ACCRETING NEUTRON STARS IN GALACTIC GLOBULAR CLUSTERS

By

Teresa Panurach

A DISSERTATION

Submitted to
Michigan State University
in partial fulfillment of the requirements
for the degree of

Astrophysics and Astronomy—Doctor of Philosophy

2023

# ABSTRACT

# ACCRETING NEUTRON STARS IN GALACTIC GLOBULAR CLUSTERS

## By

## Teresa Panurach

Accreting neutron stars in low-mass X-ray binaries show outflows—and sometimes jets—in the general manner of accreting black holes. However, the quantitative link between the accretion flow (traced by X-rays) and outflows and/or jets (traced by radio emission) is much less well understood for neutron stars than for black holes because of observational challenges. Their distances are generally unknown or poorly constrained and black holes tend to be radio brighter, therefore limiting the ability to draw accurate conclusions about the physics of neutron star's accretion. Despite the challenge, radio continuum studies of neutron stars are needed to understand their broad range of physical properties that are likely to affect their jets/outflows.

In this thesis, we use data from the radio continuum survey, MAVERIC and *Swift*/XRT and *Chandra* X-ray Telescope to do a systematic study of accreting neutron star X-ray binaries in globular clusters to understand the connection of their jets and accretion disk. We first explore the behaviors of eight persistently accretion neutron star X-ray binaries. In this work, we show that these neutron stars show an even larger range in radio luminosity than previously observed and do not follow a single relation between inflow and outflow. Next, we delve further into a peculiar source from our first study, X1850-087 that showed extreme radio variability within a short time-scale. Lastly, we present our work on imaging seven globular clusters taken as the final tranche of the MAVERIC Survey, along with a

radio source catalog of NGC 6522.

”i used to rebel by destroying myself, but i realized that’s awfully convenient to the world.
for some of us, our best revolt is self-preservation.”
— Mitski (2016 December 2)

*I dedicate this thesis to me, myself and I.*

# ACKNOWLEDGMENTS

The wise woman Lady Gaga said, ”Tooth and nail, blood, sweat, and leather every night. No sleep. Bus, club, ’nother club, ’nother club, plane, next place, no sleep, no fear, nobody believed in me.” – This thesis was not made in peace. This thesis was made with the eye of the tiger. I’m so grateful for all of you for supporting me every step of the way.

I want to firstly acknowledge my advisors Jay Strader and Laura Chomiuk who without them I would not be writing this thesis. I know I am an annoying underachiever and probably the most slacker PhD student in the whole field of astronomy but thank you for always being my biggest ally. If it wasn’t for you two I would probably have left astronomy a long time ago. I’m so lucky to have both of you in my life.

I want to thank my thesis committee: Ed Brown, Nathan Whitehorn, Kaitlin Cook, and Seth Jacobson for their support and challenging me to become a better scientist. I also want to thank my scientific collaborators, especially Ryan Urquhart and Arash Bahramian, who know how to push my buttons and keep my head from getting too big.

MSU astro grad program would be nothing without its graduate students. I want to acknowledge my girls (Adam Kawash, Mike Pakjos, Justin Grace, and Claire Kopenhafer) who made sure I ate and had my head on straight as a first-year. To the “first-years” who are not baby sharks anymore (Brandon Barker, CJ Llorente, Erica Thygesen, Josh Shields, and Katie Bowen) who pulled me out of a severe depressive burn-out. Also Hailey Moore, Noah Vowell, Sierra Casten, and Jack Schulte, and especially Bella Molina for being my radio reduction sister.

The MSU alums that hold a special place in my heart: Kristen Dage, Megan Davis, Carl Fields, Forrest Glines, Jessica Maldanado and Huei Sears.

Thank you to my AstroCom NYC and CUNYAstro family who supported me at the beginning of my career; Ellie Abrahams, Aurora Cid, Victoria DiTomasso, and JP Ventura.

To the Drew Scholars and the other REU students who entrusted me as their PAREDS director. I am so grateful and excited to watch your careers flourish.

To the other MSU professors and admins who have supported me: Danny Caballero, Paul Guèye, Lerena Heintzelman, Kim Crosslan, Susie Harwood-Brown, and Brenda Wenzlick.

I want to thank my family: my sister and my parents who love me at my worst and aren't afraid to tell me I am f—g up. Thank you to Sonny, who is constantly pushing me to be my best self. My bestie Esther, who is the face of reason and joy in my life. Most importantly, I want to thank my little monsters: Kujo and Hiso, who have been there since the beginning of my academic journey.

Lastly, I want to acknowledge support from from the National Science Foundation Graduate Research Fellowship Program under grant number DGE 1848739.

# TABLE OF CONTENTS

# LIST OF TABLES

# LIST OF FIGURES

# Chapter 1

# Introduction

*"You're less unhinged than you pretend! I know the truth."* — LBC

## 1.1 Neutron Stars

Over time, a massive main sequence star ($\sim 8M_{\odot}$) will follow the path of stellar evolution and exhaust their nuclear fuel. Once their iron-core exceeds the Chandrasekhar limit, it will succumb to its own gravity and collapse into itself, creating a stellar remnant known as the neutron star. These remnants are extremely compact and dense ($\rho \sim 10^{15}$ g cm$^{-3}$) with their structures supported primarily through neutron degeneracy pressure. Newly born neutron stars tend to have high magnetic fields ($\leq 10^{15}$ G) and rapidly rotate.

Neutron stars will cool and fade over time due to the lack of nuclear fusion. We have only detected thermal emission from very nearby and young neutron but have been discovered through other detection methods: radio pulsations from pulsars and accretion in X-ray binaries.

Radio pulsars are highly magnetized and rapidly spinning neutron stars. Because of the misalignment of their magnetic field and rotational axis, the pulsar produces strong beams of light. Pulsars was discovered by Jocelyn Bell Burnell in the late 60's through strong radio pulsations (Hewish et al., 1968) and were the first direct observations of a neutron star. Today, astronomers have discovered thousands of Galactic pulsars with large single-dish timed radio surveys from telescopes such as the Lovell Telescope in Jodrell Bank Observatory or Green Bank Telescope, and the addition of arrays like MeerKAT to advance the finding of pulsars. Modern searches have also enabled us to search for even fainter pulsed signals through advances in computational techniques (Andersen & Ransom, 2018; Cadelano et al., 2018). The launch of Fermi Gamma-ray Space Telescope has allowed the detection of pulsars via their pulsed gamma-ray emission rather than radio emission. Pulsars have proven crucial in detailed tests of the theory of general relativity. Perhaps the most famous example is that of the Hulse-Taylor pulsar binary (Hulse & Taylor, 1975).

### 1.1.1 Neutron Star X-ray Binaries

Gravitational accretion onto compact objects such as neutron starsn and black holes is the most efficient way to generate energy, with the possibility of turning a substantial fraction of the infalling mass into energy. Accretion can affect the fundamental properties of the compact object, such as its mass and spin. Accretion is a common phenomena for compact object regardless of the nature and size as we see it in supermassive black holes (active galatic nuclei) to accreting white dwarfs (catalysmic variables). The high radiative efficiency of accretion allows one to trace the mass accretion history of an object such as a neutron star in detail. In this body of work, we will focus on accreting neutron stars in low-mass X-ray binary systems.

Neutron star X-ray binaries belong to a larger class of system called low-mass X-ray binaries (LMXBs). These systems can contain either a neutron star or stellar-mass black hole with a main sequence, evolved giant star or a stellar degenerate like a white dwarf (Katz, 1975). Most LMXBs accrete material through Roche-lobe overflow; where the secondary fills its Roche lobe either by expansion or through a loss of angular momentum by another cause, such as magnetic braking or gravitational radiation. The material lost through Roche lobe overflow can form an accretion disk around the neutron star due to conservation of angular momentum. This not to be confused with high-mass X-ray binaries where their companions are more massive ($\sim 10 M_{\odot}$) and their accretion process are primarily driven by stellar winds from the stars' radiation pressure and do not have accretion disks.

Today we know that X-ray binaries systems can be seen in a variety of wavelengths but originally were found via X-ray surveys in the late seventies by Uhuru and OSO-7 (Clark, 1975). Most sources are often X-ray luminous, $L_X > 10^{36}$ erg $s^{-1}$ up to the Eddington limit (Grindlay et al., 1976) but numerous quiescent systems ($L_X < 10^{34}$) has been found mostly in globular clusters through deep Chandra X-ray Telescope studies (Heinke et al., 2003; Bahramian et al., 2014), however we note that this lower limit is based on the telescope's observational sensitivity limit. Galactic neutron star LMXBs have been found to produce various accreting behaviors depending on their accretion rates and companion. They are further are separated into various sub-classes based on their luminosity and hardness during their stages of accretion.

### 1.1.2 Other Neutron Star LMXBs: Accreting Millisecond Pulsars and Transitional Millisecond Pulsars

Neutron star LMXBs are thought to be the progenitors of millisecond pulsars. The neutron star accretes material from its companion and over time the system will gain mass and angular momentum, spinning it up. At birth, the neutron star spins rapidly but, over time it will start to lose its spin. If a millisecond pulsar is in a binary, it can be possible for

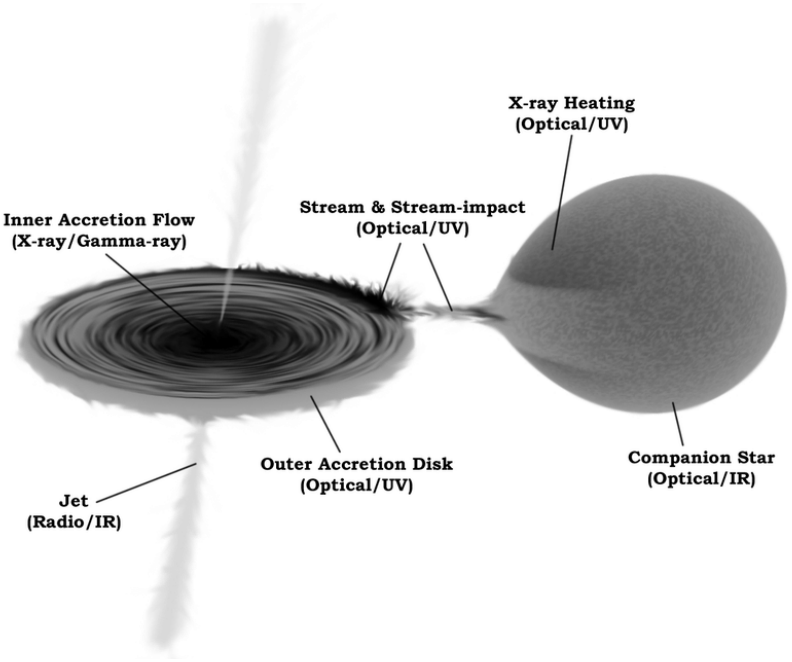

Figure 1.1: Artist depiction of low-mass X-ray binary (Rob Hynes).

the neutron star to regain a faster spin via accretion of a companion. This process of the neutron star quickly rotating after birth, losing its spin, and then being spun up again is by its companion, is called ”recycling” (Alpar et al., 1982).

If the accretion continues once the neutron star has been recycled to a high spin rate, then accretion would flow onto the magnetic poles of the neutron star in the LMXB and create a sweeping lighthouse effect, similar to millisecond pulsars. General relativity modifies the pulse in a manner that does not happen for the pulsed radio emission, which occurs at larger radii. The first of its kind was discovered in 1998 (Wijnands & van der Klis, 1998) and was aptly named accreting millisecond X-ray pulsar cause they accrete and show X-ray pulsations during millisecond pulsar spin period. Once accretion stops, the system switches back to a pulsar.

Millisecond pulsar systems called ”spiders” have been recently discovered. They are known to have short orbital periods, often only a few hours, and have hydrogen-rich main-sequence like secondaries. Spiders can be split into two sub-classes of either "redbacks" or "black widows" depending on the mass of the stellar companion (split above and below $\sim 0.1 M_\odot$, respectively; Fruchter et al. (1988); Lyne et al. (1990); Ferraro et al. (2001); Roberts (2013). Previous radio pulsar surveys overlooked these sources because lack of pointed observations as spiders show extensive radio eclipses due to the accreted material being ablated by the millisecond pulsar. A small number of redback pulsars belong to a new class of millisecond pulsars, transitional millisecond pulsars. Transitional millisecond pulsars may represent the very last stages of the recycling process, where the magnetosphere of the fast-spinning neutron star and the ram pressure of infalling material are almost balanced. These systems switch between a typical rotational- powered pulsar and an accretion powered system (Radhakrishnan & Srinivasan, 1982; Alpar et al., 1982). Only three of these transitional systems have been confirmed, one of which is in globular cluster M28 (Papitto et al., 2013).

## 1.2 Accretion Processes

Neutron star LMXBs accrete material through Roche-lobe overflow. The star becomes teardrop-shaped and material is only lost through the $L_1$ Lagrangian point because that is the only point where the tiny perturbation puts the material into the potential of the compact object rather than the donor star (Figure1.2). Many factors affect the mass accretion rate from the companion: magnetic breaking, gravitational wave emission for low-mass donors, or nuclear evolution if the secondary is a subgiant/red giant star. Because of angular momentum, neutron star LMXBs will form an accretion disk. The material comes from the companion to the outer disk, and moves through the disk and loses angular momentum to be pushed outward. Once the system loses its angular momentum, it will accrete its material onto the compact object from the inner disk.

In a standard accretion disk model (Shakura & Sunyaev, 1973), the material will flow through the disk due to magnetorotational instability that is controlled by the viscosity parameter, $\alpha$. Standard disk have a temperature profile,

$$T \sim r^{-3/4} \dot{M}^{1/4},$$

making it hotter towards the center and for higher accretion rates. Viscosity depends strongly on ionization rates of hydrogen, or in rare cases helium. If the accretion rate is high, then hydrogen is always ionized at all radii and the viscosity is also high, which makes accretion rates onto the compact object high. These are persistent neutron star LMXBs and are less common. If accretion rate from the secondary is lower, there is some hydrogen in the outer disk, therefore viscosity is lower and accretion onto the compact object is low. But as mass builds up temperature starts to rise and the radius of hydrogen ionization is enough to trigger a jump in viscosity. This creates an increase of accretion rate at the radius that could spread and lead to a process known as a Type I X-ray burst (Grindlay et al., 1976; Kuulkers et al., 2003). The bulk of the disk ends up hot and is dumped onto the compact object over a few days, weeks, or months (King et al., 1998). Sources that undergo this high and low accreting stages are called transients and the most common behavior of LMXBs. This process is most useful in determining whether the compact object in a LMXB is a neutron star, since black holes cannot produce these bursts as they have no surfaces.

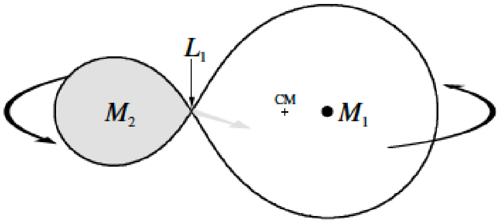

Figure 1.2: A binary system where the companion ($M_2$) is filling its Roche-lobe and accreting material onto the compact object ($M_1$). Illustration from King et al. (1998).

### 1.2.1 The Radio/X-ray Correlation Plane of Neutron Star X-ray Binaries

The connection between the accretion/inflow of material in neutron stars (observed by X-ray wavelengths) and the launching of their jets/outflows (observed in the radio wavelengths) is a process that has yet to be fully understood. Simultaneous observations of both wavelengths have been useful in offering us insights to how these two processes connect in compact objects (Hannikainen et al., 1998; Corbel et al., 2000).

Figure 1.1 Bahramian et al. (2014) shows the radio/X-ray correlation plane for accreting hard-state black hole X-ray binaries and NSXBs. Additional other diverse neutron star systems like accreting millisecond X-ray pulsars and transitional millisecond pulsars, as well as accreting and non-accreting white dwarfs. Neutron stars that have observed on this show that their jet/outflows are significantly less bright than black holes at the same X-ray luminosity (Gallo et al., 2018). Some neutron stars do deviate from this path and shown to be as bright as the black hole population but mostly follow this trend. The surest way of determining if the systems harbours a neutron star is if it shows Type I X-ray bursts. However, this method cannot be used to determine all neutron stars as some systems may accrete too low to show Type I X-ray bursts or if the system's inclination happens to be on an edge-on orientation that the accretion disk eclipses all potential bursts (e.g. AC211 in M15). Even if, neutron stars and black holes can be distinguished based on the radio/X-ray correlation plane, the slope of the correlations is shallower if the binary has an unknown distance which can fall to either correlations depending on the assumed distance. In the absence of accurate distances to individual sources, a fixed distance of 8 kpc or one based on the assumed luminosity of Type I X-ray bursts is assumed, which can be substantially in error. An alternative approach to understanding neutron stars behavior is to focus on sources whose distance is well-constrained: those in globular clusters.

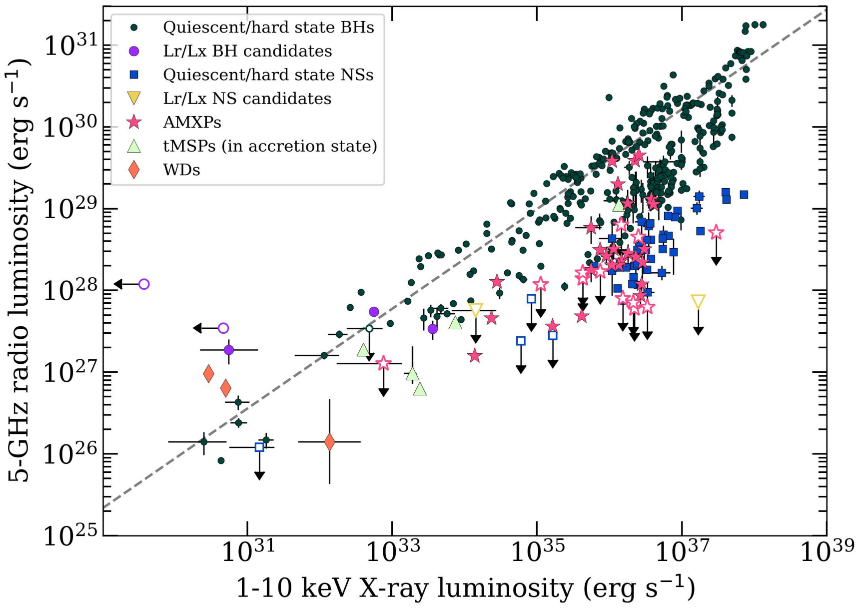

Figure 1.3: The radio/X-ray correlation plan for compact objects from (Bahramian et al., 2018).

## 1.3 Neutron Star LMXBs in Globular Clusters

Globular clusters are massive, dense collection of stars as shown in 47Tuc in Figure 1.4, ranging from $M \approx 10^5 - 10^6 M_{\odot}$. The Milky Way contains of $\sim$ 160 globular clusters, mostly residing towards the Galactic center and some towards the halo. Observations of globular cluster reveal an overabundant population of millisecond pulsars and neutron star LMXBs (Bhattacharya & van den Heuvel, 1991; Pooley et al., 2003; Ivanova et al., 2008). Studying these systems in globular clusters gives us an advantage of a large sample with accurate distances which is much needed to understand the behaviors of accreting neutron stars.

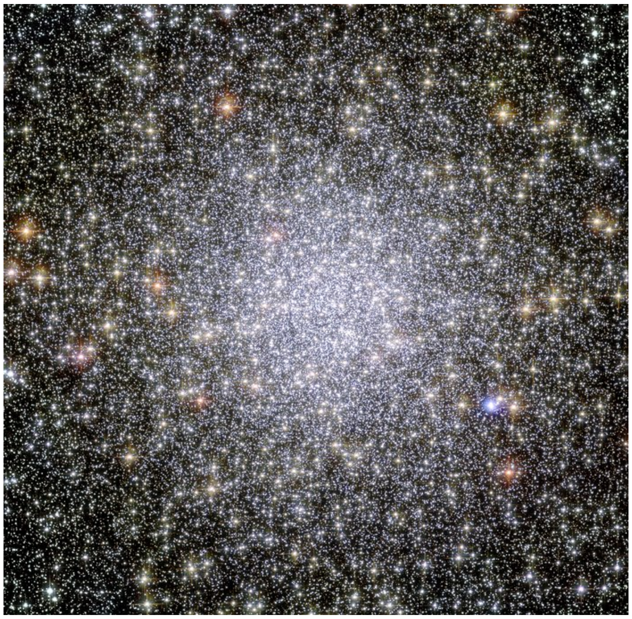

Figure 1.4: NASA/ESA Hubble Space Telescope image of 47 Tucanae, also known as NGC 104.

## 1.4 Motivations of This Work

### 1.4.1 Increasing Radio Studies of Neutron Stars to Understand Jet–Accretion Coupling

Understanding the mechanisms behind jet production in compact objects is still an unsolved astrophysical problem. Although there has been models for black hole jet production Blandford & Znajek (1977), this has been limited for neutron stars. Understanding how these jets form and launch in neutron stars can give of insights to understanding jet production for all accreting compact objects.

The radio/X-ray correlation plane has been a useful observational tool in understanding the jet–accretion coupling behaviors for accreting compact objects. However, objects on this plot tend to bias more towards black hole X-ray binaries because a larger fraction of them are transient and their outbursts last longer than neutron stars. Accretion dynamics for neutron stars are more complicated than black holes. Numerous works have suggested explanations of the radio/X-ray variations for neutron stars by subdividing their populations into different classes of accreting neutron stars and fitting relations to those (Migliari & Fender, 2006; Tetarenko et al., 2018; Gallo et al., 2018), but this has not been successful in fully explaining what is driving the population's scatter. Additional previous work have including physical mechanisms into their relations like spin rate and magnetic field (Tetarenko et al., 2018; Gallo et al., 2018; van den Eijnden et al., 2018a) but none with conclusive answers. Increasing our observations of neutron stars will aid us in what sort of mechanisms are at play.

### 1.4.2 What is the Origin of Neutron Stars in Globular Clusters?

The origin of neutron stars in globular clusters still remain a mystery. The most well-known formation channel of neutron stars is through the explosion of massive stars known as core-collapse supernovae. The associated explosion would have the neutron star receive a strong natal kick of hundreds of km s$^{-1}$ (Hobbs et al., 2005), which is much larger than than the escape velocity of typical globular clusters. However, in today's observations, we see an overabundant population of neutron stars in globular clusters. One prediction of how globular clusters were able to retain neutron stars is through electron-capture supernovae, which are thought to arise in stars about 8 times as massive as our Sun, and are thought to produce a less energetic natal kick ( 20 km $s^{-1}$), leading to retention of the neutron star in the cluster (Kiel et al., 2008; Ye et al., 2019). Accretion-induced collapse is the other possible route of retaining neutron stars in globular clusters; an oxygen-neon white dwarf in a binary system could accrete from or merge with its companion star, creating a neutron star if the product exceeds the Chandrasekhar limit (Ye et al., 2022). Attaining more observations of neutron star systems in globular clusters will reinforce our understanding in what settings are needed to produce these sources.

### 1.4.3 How Do We Differentiate Black Holes and Neutron Stars?

The overabundance of millisecond pulsars and NS LMXBs gives the strongest evidence for dynamical formation and interaction of compact binaries in globular clusters. The detection of many binary black hole mergers via gravitational waves has renewed interest in globular cluster dynamics, including suggestions that a large number of merging black holes could have originally be formed dynamically. Models to produce such mergers also make predictions about the present-day properties of globular clusters, including their neutron star and black hole populations. Hence continued study of compact objects in Galactic globular clusters, including the relationship between neutron star and black hole populations in individual clusters, has broad implications in astrophysics. Clusters such as, Terzan 5 and 47 Tuc, were observationally shown to have a large number of stellar-mass black hole candidates with large populations of neutron stars, specifically pulsars (Miller-Jones et al., 2015; Bahramian et al., 2018; Urquhart et al., 2020). Observing more neutron star systems will allow us to constrain the relationship between these two compact objects.

## 1.5 Outline

Chapter two consists of the peer reviewed article written by Panurach et al. (2021) which is published in the Astrophysical Journal. It uses a sample of strictly/quasi-simultaneous radio and X-ray observations of six persistently accreting neutron star X-ray binaries and two transients systems in Galactic globular clusters to understand the quantitative link between the accretion flow (traced by X-rays) and outflows and/or jets (traced by radio emission) for luminous systems. With this study, we find that these neutron star systems show a broader range of radio luminosity than previously observed and do not follow a single relation between inflow and outflow.

Chapter three consists of the peer reviewed article written by Panurach et al. (2022) which is submitted to the Astrophysical Journal. This work stems from our previous work in Panurach et al. (2021) where we saw the ultracompact neutron star X-ray binary, X1850-087 in globular cluster NGC 6712 show unusual radio variability on short timescales. We undertook a radio monitoring campaign using the Karl G. Jansky Very Large Array with quasi-simultaneous Swift/X-Ray Telescope observations for each epoch from Feburary to June 2022. The system is detected in two of the six radio epochs with no X-ray spectral change however, it shows a slightly increased X-ray luminosity during these times. At all detected epochs X1850–087 has a flat-to-inverted radio spectral index, more consistent with the partially absorbed optically thick synchrotron of a compact jet rather than the evolving optically thick to thin emission associated with transient expanding synchrotron blobs. If the radio emission in X1850–087 is indeed associated with a compact jet, then it is plausibly being launched and quenched in the hard state on timescales as short as a few days.

Chapter four consists of the ongoing work of the final observations of our MAVERIC

Survey. We describe the data reduction process and show the radio continuum images of each cluster, as well as a radio source catalog for one of them. In Chapter five, we summarize our findings and discuss future work.

# Chapter 2

# The MAVERIC Survey: Variable Jet–accretion Coupling in Luminous Accreting Neutron Stars in Galactic Globular Clusters

*"I was in high school in Minneapolis in 1995, i like Semisonic too."* — JMS

## 2.1 Introduction

Neutron star low-mass X-ray binaries (LMXBs) contain a neutron star primary accreting through a disk from a $< 1M_\odot$ secondary, which can be a low-mass main sequence star, an evolved star, or a degenerate star such as a white dwarf. Neutron star LMXBs are enormously overabundant (by a factor of $\sim 100$) in globular clusters, where they form dynamically due to the high stellar densities (e.g., Clark (1975); Katz (1975); Ivanova et al. (2008)).

The observed neutron star LMXBs in Galactic globular clusters include both persistent and transient sources (Bahramian et al., 2014; van den Berg, 2020). The former are always X-ray luminous ($L_X > 10^{35}$ erg s$^{-1}$), due to their high companion mass transfer rates, which keep the disk consistently in a hot, ionized state. The transient sources tend to have lower mass transfer rates from the secondary. This leads to the standard accretion disk ionization instability in which the disk alternates between a cool state with little accretion onto the neutron star ("quiescence") and a hot "outbursting" state with substantial accretion (Smak, 1984; van Paradijs, 1996; Lasota, 2001).

Since neutron stars have surfaces, it should be possible to trace the details of the accretion flow from the secondary to the disk, and thence as material accretes onto the neutron star, with some being ejected in an outflow or jet. X-ray observations primarily probe the inner regions of the accretion flow as well as the neutron star surface, while radio continuum data trace synchrotron emission associated with the outflow/jet.

Although extensive radio and X-ray observations have been made to constrain jet and accretion disk properties of all accreting compact objects (e.g., Merloni et al. 2003; Migliari & Fender 2006; Gallo et al. 2018; Coppejans & Knigge 2020; van den Eijnden et al. 2021), existing studies are biased towards black holes. Newly discovered transient X-ray sources in the field that can be accurately classified tend to be black holes rather than neutron stars, as black holes are on average brighter in the X-ray and far more radio-loud than neutron stars at nearly all accretion rates (e.g., Corbel et al. 2000; Migliari & Fender 2006; Tudor et al. 2017; Gallo et al. 2018), with the caveat that some black holes and neutron stars deviate from this typical behavior (e.g., Coriat et al. 2011; Migliari et al. 2011; Rushton et al. 2016; Tudor et al. 2017; Russell et al. 2018; van den Eijnden et al. 2018b; Gusinskaia et al. 2020a). Despite the challenge, radio continuum studies of neutron stars are needed: there is a broad range of physical properties that are likely to affect the outflows/jets from these sources (such as their spin frequencies and surface magnetic field strengths), and there is strong observational evidence that accreting neutron stars show a greater variety of radio properties than accreting black holes (e.g., Migliari et al. 2011; Tudor et al. 2017; Gusinskaia et al. 2017; van den Eijnden et al. 2021).

One difficulty in studying field LMXBs is that their distances are generally unknown or poorly constrained (Jonker et al., 2004), limiting the ability to draw accurate conclusions about the physics of the accretion. For example, distances inferred from X-ray bursts can have substantial systematic uncertainties (e.g., Galloway et al. (2008)), and some ultracompact neutron star LMXBs do not show X-ray bursts at all. This issue is ameliorated in globular clusters, which have well-determined distances as well as a substantial population of neutron star LMXBs.

Here we present a radio and X-ray study of a sample of neutron star X-ray binary systems in Galactic globular clusters, focusing on eight luminous systems. In Section 2, we discuss the sample and observations. We use radio data from the Karl G. Jansky Very Large Array (VLA) or Australia Telescope Compact Array (ATCA) and we use X-ray data from Swift/X-Ray Telescope (Swift/XRT) and the Chandra X-ray Telescope (Chandra). In Section 3, we consider the results from individual sources. We present discussion and a summary in Sections 4 and 5, respectively.

## 2.2 Observational Data

### 2.2.1 Our Sample

Our sample includes all of the luminous ($L_X > 10^{34}$ erg s$^{-1}$) persistent LMXBs from the MAVERIC (Milky Way ATCA and VLA Exploration of Radio-sources in Clusters) radio continuum survey of 50 Galactic globular clusters (Tremou et al. 2018; Shishkovsky et al. 2020, Tudor et al. 2021, in prep). This survey includes all of the nearest ($< 9$ kpc) massive

($> 10^5$ $M_\odot$) clusters.

The persistent LMXBs included in this study are: 4U 1746–37 (NGC 6441); 4U 1820–30 (NGC 6624); XB 1832–330 (NGC 6652); X1850–087 (NGC 6712); and AC 211 and M15 X-2 (M15). These represent 6 of the 8 persistent globular cluster sources known, excluding only 4U 0513–40 (NGC 1851; Zurek et al. 2009) and 4U 1722–30 (Terzan 2; in't Zand et al. 2007) as their host clusters are not in MAVERIC and have no deep ATCA or VLA data. To this initial sample we also add two other luminous transient sources. The first is GRS 1747–312 (Terzan 6), which shows approximately biannual outbursts (Pavlinsky et al., 1994; in't Zand et al., 2003a). The other is M15 X-3, an X-ray transient with limited existing studies of its radio properties (Heinke et al., 2009; Strader et al., 2012b) and one of two globular cluster LMXBs that has been observed at $L_X \sim 10^{34}$ erg s$^{-1}$ over timescales of years (the other is N6652B; Paduano et al. 2021). Other known bright X-ray transients in globular clusters were either not in outburst during our observations or were not in the original MAVERIC data release. For all sources we assume the cluster distances from Tremou et al. (2018).

| ID | Cluster | RA (a) (H:M:S) | Dec (a) (°:':") | Date of Radio Obs. (UT) | $S_{5.0\ \mathrm{GHz}}$ (b) (uJy) | Date of X-ray Obs. (UT) | X-ray Flux (c) (ergs $\mathrm{s}^{-1}\mathrm{cm}^{-2}$) |
|---|---|---|---|---|---|---|---|
| 4U 1746–37 | NGC 6441 | 17:50:12.695 | –37:03:06.56 | 2015 April 15.250 (14.542–15.958) | $< 13.7$ (e) | 2015 April 13.045 (13.027–13.063) | $(8.6 \pm 2.0) \times 10^{-10}$ |
| GRS 1747–312 | Terzan 6 | 17:50:46.912 (d) | –31:16:29.18 (d) | 2015 April 18.250 (17.542–18.958) | $221 \pm 6.4$ | 2015 April 16.690 (16.672–16.709) | $(5.3^{+4.0}_{-2.4}) \times 10^{-12}$ |
|  |  |  |  | 2018 March 25.594 (25.557–25.630) | $< 12.9$ | 2018 March 26.567 (26.549–26.586) | $(8.0^{+13.6}_{-4.8}) \times 10^{-12}$ |
|  |  |  |  | 2018 April 30.380 (30.344–30.417) | $26.9 \pm 4.3$ | 2018 May 01.569 (01.550–01.587) | $(1.3^{+1.2}_{-0.8}) \times 10^{-12}$ |
| 4U 1820–30 | NGC 6624 | 18:23:40.499 | –30:21:40.10 | 2014 July 17.521 (17.417–17.625) | $241 \pm 28$ | 2014 July 19.492 (19.459–19.524) | $(9.6 \pm 0.2) \times 10^{-9}$ |
|  |  |  |  | 2015 April 25.250 (24.542–25.958) | $241 \pm 5.1$ | 2015 April 24.861 (24.810–24.912) | $(1.5 \pm 0.1) \times 10^{-9}$ |
| XB 1832–330 | NGC 6652 | 18:35:43.656 | –32:59:26.35 | 2017 May 22.415 (22.350–480) | $< 6.6$ (e) | 2017 May 22.783 (22.343–23.223) | $(1.9 \pm 0.1) \times 10^{-11}$ |
| X1850–087 | NGC 6712 | 18:53:04.867 | –08:42:20.34 | 2014 April 05.626 (05.590–05.661) | $<12.9$ | 2014 April 06.463 (06.424-06.502) | $(1.6 \pm 0.1) \times 10^{-10}$ |
| AC 211 | M15 | 21:29:58.310 | 12:10:02.66 | 2011 May 30.512 (30.455–30.568) | $292 \pm 6.3$ | 2011 May 31.017 (30.691–31.343) | $(4.46 \pm 0.05) \times 10^{-10}$ |
| M15 X-2 | M15 | 21:29:58.132 | 12:10:02.24 | 2011 May 30.512 (30.455–30.568) | $205 \pm 6.3$ | 2011 May 31.017 (30.691–31.343) | $(9.46 \pm 0.03) \times 10^{-10}$ |
| M15 X-3 | M15 | 21:29:58.161 | 12:09:39.93 | 2011 May 30.512 (30.455–30.568) | $<16.1$ | 2011 May 31.017 (30.691–31.343) | $3.5^{+1.4}_{-0.8} \times 10^{-13}$ |

Table 2.1: Quasi-Simultaneous Radio and X-ray Observations.

**Note.**

(a) ICRS coordinates.

(b) Radio flux density at 5.0 GHz.

(c) Unabsorbed X-ray flux at 1–10 keV.

(d) This is an average of the VLA 5.0 and 7.1 GHz positions.

(e) Assuming $\alpha = 0$.

### 2.2.2 Radio Observations

The radio continuum data used in this paper come primarily, though not entirely, from the MAVERIC survey. Observations for the survey were obtained with ATCA or the VLA, depending on the declination of the source.

Three clusters in this paper have ATCA data: NGC 6441, NGC 6624, and Terzan 6. The ATCA observations are discussed in detail in Tremou et al. (2018) and Tudor et al. (2021, in prep). In brief, for each of these clusters, the observations were made in April 2015 in the extended 6 km configuration. Data were taken in two basebands centered at 5.5 and 9.0 GHz, each with 2 GHz of bandwidth. These data were flagged and calibrated in Miriad (Sault et al., 1995) and imaged in CASA (Common Astronomy Software Applications; McMullin et al. 2007), resulting in median synthesized beams of $\sim$ 2–3”, depending on frequency.

Four of the clusters we study in this work have VLA data: M15, NGC 6652, NGC 6712, and Terzan 6 (which also has ATCA data). M15 was observed in 2011 during an brightening/flaring event of M15 X-2, prior to the official start of MAVERIC but with similar observing frequencies and depth. The M15 data were calibrated and imaged in AIPS (Astronomical Image Processing System; Greisen 2003) and CASA. Additional data reduction details for M15 can be found in Strader et al. (2012a). NGC 6712 was observed as part of the initial MAVERIC VLA program in 2014, with deep C band observations imaged at central frequencies of 5.0 and 7.4 GHz, and calibrated and imaged in AIPS (Shishkovsky et al., 2020).

The 2018 Terzan 6 data were obtained as part of the final tranche of MAVERIC VLA observations (program 18A-081, PI: Shishkovsky). These observations were made from 2018 March 25 to June 3 in five separate 1 or 2-hr blocks observed when the VLA was in its most extended A configuration. Data were taken in two 2 GHz basebands with 3-bit receivers, with central frequencies of 5.0 and 7.1 GHz after flagging. These data were calibrated and imaged in AIPS, resulting in a typical synthesized beam of $\sim 1.1" \times 0.4"$.

Finally, NGC 6652 was observed in May 2017 as part of a MAVERIC follow-up program to study the transitional millisecond pulsar candidate N6652B with joint Chandra and VLA data (program SI0399, PI: Tudor; see Paduano et al. 2021 for the analysis of N6652B). The VLA observations consist of a single $\sim 2.5$ hr block in C configuration at X band, using 3-bit receivers and two 2 GHz basebands centered at 9.0 and 11.0 GHz. The data were flagged, calibrated, and imaged in CASA. The synthesized beam at the average frequency of 10 GHz was $5.3 \times 2.1$.

The observation times and 5.0 GHz flux densities (or upper limits) for all sources with accompanying X-ray measurements are listed in Table 2.1, and each source is discussed in detail in Section 3. For the ATCA observations, which are centered at 5.5 GHz rather than 5.0 GHz, we infer the 5.0 GHz density from the 5.5 GHz flux density and the the measured (or assumed) spectral index between 5.5 and 9.0 GHz. We give the details of the calculation for each source in the appropriate subsection.

All radio flux densities were measured by fitting the appropriate point source models to the individual images. Unless otherwise stated, the radio continuum flux density measurements list $1\sigma$ uncertainties (including a minimum 1% systematic uncertainty), and upper limits are given at the $3\sigma$ level, where $\sigma$ for the upper limits is measured as the root mean square noise in the local region around the source. Radio spectral indices or limits were determined using the Bayesian fitting method described in Shishkovsky et al. (2020). Representative radio continuum images for each source are shown in the Appendix in Figures 2.8 and 2.9.

### 2.2.3 X-ray Observations

A key aspect of the MAVERIC survey was obtaining X-ray observations close in time to at least one radio observing block for each cluster, allowing for close-to-simultaneous radio and X-ray measurements for more luminous sources. For clarity, we define "strictly simultaneous" measurements to be those for which the X-ray and radio data at least partially overlap in time (typically the radio observations last longer). We take "quasi-simultaneous" observations to be those without overlapping data, but with an offset between the X-ray and radio data of 2 d.

The simultaneous X-ray measurements for most globular clusters in this paper come from Swift/XRT, excepting M15 and NGC 6652, which are from Chandra. Chandra can resolve individual sources even in dense clusters. By contrast, individual sources are not typically well-resolved in Swift/XRT data, but all of the targets in our observations are sufficiently X-ray luminous that they dominate the cluster emission, and hence any Swift/XRT counts can be ascribed to the targets of interest. We analyzed all Swift/XRT (Gehrels et al., 2004; Burrows et al., 2005) and Chandra observations of our sample that were taken close to (or simultaneously with) radio observations of these targets. These observations are listed in Table **??**. The Swift/XRT observations were all made in Photon Counting mode. Unless otherwise stated, all reported X-ray fluxes and luminosities are in the 1–10 keV band, and all X-ray parameter uncertainties are at the 90% confidence level.

All Swift/XRT observations were reduced and analyzed using HEASOFT[1] (version 6.25, NASA High Energy Astrophysics Science Archive Research Center, 2014). We reprocessed XRT data using `xrtpipeline`, and extracted spectra with `xselect`, following standard

---

[1] `https://heasarc.gsfc.nasa.gov/docs/software/lheasoft/`

procedures.[2] For observations where the observed source count rate was high enough to cause pileup, we followed the recommended methods to estimate and exclude the piled up region.[3]

We also reduced and analyzed the Chandra data fitting our simultaneity criteria using CIAO 4.10 with CalDB 4.7.4 (Fruscione et al., 2006). These data include Chandra/ACIS-S data for NGC 6652 (Obs. ID 18987) and Chandra/HRC data for M15 (Obs. ID 13420).

NGC 6652 is the host cluster to XB 1832–330. Observed with a subarray on the ACIS-S S3 chip, XB 1832–330 is likely piled up in this observation. We extracted spectra from the source point spread function and modeled the pileup using the model produced by Davis (2001). For this model we froze the frame time to 0.4s (based on the subarray mode used), the maximum number of photons considered for pileup in a single frame (`max_ph`) to 5, grade correction to 1, pileup PSF fraction to 0.95, and left grade migration ($\alpha$) variable. To complement this analysis, we also modeled the faint, un-piled up readout streak from XB 1832–330 that is also present in this observation. This streak has a relatively low signal-to-noise ratio and so does not offer a precise independent spectral constraint. Nonetheless, analysis of the streak gave a consistent result. This source is discussed in more detail in Section 3.3.

For the analysis of the Chandra/HRC data of M15, after standard reprocessing, we estimated count rates and background for each of the three sources, then determined the X-ray fluxes using the model of White & Angelini (2001) (for AC 211 and M15 X-2) or Arnason et al. (2015) (for M15 X-3). These data are discussed in more detail in Section 3.6.

We used XSPEC (Arnaud, 1996), with Verner et al. (1996) photoelectric cross section and

---

[2] `https://www.swift.ac.uk/analysis/xrt/`

[3] `https://www.swift.ac.uk/analysis/xrt/pileup.php`

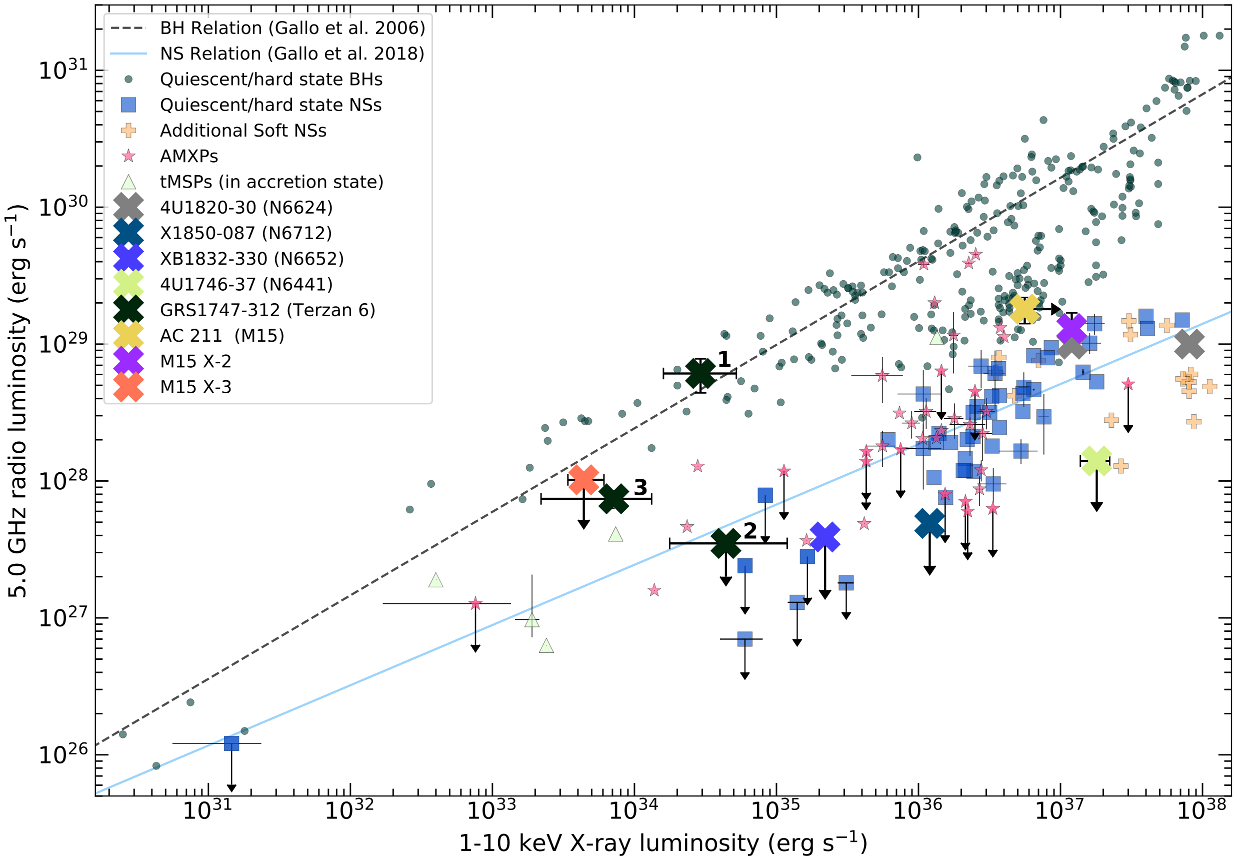

Figure 2.1: Radio luminosity (at 5.0 GHz) vs. X-ray luminosity (1–10 keV) for accreting black hole and neutron star low-mass X-ray binaries, adapted from the compilation of Bahramian et al. (2018). Only sources with simultaneous or quasi-simultaneous data are plotted. The globular cluster sources from this paper are represented as large crosses (the letter "X"); those with multiple points are sources with more than one quasi-simultaneous data point. For clarity, we have also labeled the points for GRS 1747–312 (in Terzan 6) with numbers, denoting the first (1: 2015 April 18), second (2: 018 March 25), and third (3: 2018 April 30) quasi-simultaneous epochs for this source. The radio flux densities and X-ray fluxes from Table **??** have been converted to luminosities using the cluster distances from Tremou et al. (2018). Dark green circles show quiescent/hard state black holes. Quiescent/hard state neutron stars are shown as blue squares, with additional data points from Aql X-1 (Gusinskaia et al., 2020b), and soft sources shown as orange pluses from (Ludlam et al., 2019). Pink stars are accreting millisecond X-ray pulsars and light green triangles are transitional millisecond X-ray pulsars. The dashed gray line shows the best-fit relation ($L_R \propto L_X^{0.61}$) for black holes from Gallo et al. (2006) and solid blue line represents a proposed correlation ($L_R \propto L_X^{0.44}$) for hard-state neutron stars from Gallo et al. (2018).

Wilms et al. (2000) abundances for spectral analysis. In cases where the number of extracted source events were more than 100, we binned the spectra to have at least 20 counts per bin and used $\chi^2$ statistics for fitting. In other cases, we binned the spectra to have at least 1 count per bin, and used w-statistics as implemented in XSPEC.[4]

The X-ray data used in this paper primarily plays a supporting role to help contextualize the radio observations. Therefore, we do not attempt comprehensive fitting of X-ray models, but instead choose the simplest model(s) that allow us to characterize the flux and spectral state. For some sources, the X-ray flux is low enough that only a simple absorbed power-law or blackbody fit is possible. For other, typically more luminous sources, more complex models such as `Nthcomp` (a thermal comptonized continuum with blackbody seed photons) or composite models are justified and provide good fits. In making these choices we are guided by both the quality of the data and by previous work on these sources. For some of the brighter sources, data from MAXI (all using the Gas Slit Camera; GSC) and Swift/Burst Alert Telescope (BAT) are used to contextualize the Swift/XRT or Chandra data, providing additional constraints on the spectral state or luminosity of the source.

### 2.2.4 New HST Optical Positions

To ensure high-fidelity astrometric matching between the X-ray binaries and the radio continuum observations, we determined more precise positions of most of the sources in our sample using new Hubble Space Telescope (HST)/WFC3 observations. For all of M15, NGC 6441, NGC 6624, NGC 6652, and NGC 6712, there are ultraviolet ($F275W$) data that clearly show the sources in question and for which we calculate new positions. The exceptions are AC 211 in M15, which has a precise position from very long baseline interferometry (Kirsten et al., 2014), and Terzan 6, which has no ultraviolet data (and indeed the optical counterpart to GRS 1747–312 is unknown). The position of GRS 1747–312 is discussed in more detail in

---

[4] `https://heasarc.gsfc.nasa.gov/xanadu/xspec/manual/XSappendixStatistics.html`

Section 3.5.

For all HST data, we used a large number of stars detected by HST and in Gaia DR2 (Gaia Collaboration et al., 2018) for the ICRS astrometric solutions, finding rms values in the range of 8 to 15 mas per coordinate. We assign conservative uncertainties of 0.02 arcsec per coordinate to our final positions, which are listed in Table 2.1. These are more accurate and precise than existing X-ray positions, and are ideal for use in this paper and for future work. Note that we have made the small necessary adjustments to put the literature positions on ICRS for consistency.

## 2.3 Results for Individual Sources

### 2.3.1 4U 1820–30 in NGC 6624

4U 1820–30 is a persistent ultracompact binary with a period of 0.0079 d ($\sim 11.4$ min; Stella et al. 1987). The short period and high mean X-ray luminosity of the system are consistent with a low-mass ($\sim 0.07 M_{\odot}$) He white dwarf donor (Rappaport et al., 1987). The accretor is a neutron star that shows frequent X-ray bursts (e.g., Strohmayer et al. 2019). While the orbital X-ray variations are of low amplitude (3%), the binary is also observed to have strong X-ray luminosity variations with a superorbital period of $\sim 171$ d (Priedhorsky & Terrell, 1984; Zdziarski et al., 2007). This superorbital period is typically explained as being due to orbital dynamics in a hierarchical triple (e.g., Chou & Grindlay 2001; Prodan & Murray 2012), such that the binary has an as-yet undetected outer companion.

Here we report strictly simultaneous ATCA (radio) and Swift (X-ray) observations of 4U 1820–30 on 2015 April 24–25. We infer a 5.0 GHz flux density of $241.0 \pm 5.1$ $\mu$Jy based on the measured 5.5 and 9.0 GHz values, and there is an excellent astrometric match (separation of only 16 mas) between the HST optical and ATCA radio positions of 4U 1820–30 (Tremou et al., 2018). The radio spectral slope is $\alpha = -0.26 \pm 0.05$ for an assumed power law with $S_\nu \propto \nu^\alpha$ where $S_\nu$ is the radio flux density at frequency $\nu$ and $\alpha$ is the spectral index (this convention is used throughout this work).

The simultaneous Swift/XRT X-ray observations give an unabsorbed 1–10 keV flux of $(1.5 \pm 0.1) \times 10^{-9}$ erg s$^{-1}$ cm$^{-2}$ when fit by an absorbed `Nthcomp` model. This model is a substantially better fit ($\chi^2$/d.o.f. $= 55/40 \sim 1.4$) than a simple absorbed power law ($\chi^2$/d.o.f. $= 118/59 \sim 2.0$). The respective photon indices for these fits are $\Gamma \sim 1.6$ and $\Gamma \sim 1.3$. In Figure 2.2 we show the MAXI (4–10 keV) and Swift/BAT (15–50 keV) X-ray light curves for several hundred days around our simultaneous observations. By serendipity, our data were taken nearly perfectly at an unusually low minimum of the superorbital light curve, which corresponds to local maximum of the hardness of the system. Together these measurements strongly suggest that 4U 1820–30 was in the "island" state of this atoll neutron star LMXB, which is the lowest and hardest state observed for 4U 1820–30 (Bloser et al., 2000).

These strictly simultaneous observations place 4U 1820–30 well in the midst of the typical neutron star radio emission observed for sources in the hard/island state at $L_X \sim 10^{37}$ erg s$^{-1}$ (Figure 3.1).

Two previous works also placed 4U 1820–30 on the radio/X-ray correlation, though in the more luminous soft ("banana") state. Díaz Trigo et al. (2017) presented the 2014 radio continuum detection of 4U 1820–30 with ATCA ($236 \pm 27\mu$Jy at 5.5 GHz) and ALMA ($400 \pm 20\mu$Jy at 300 GHz; 10 days before the ATCA data). In these 2014 ATCA data, 4U 1820–30 was not detected at 9.0 GHz, with an upper limit of 200$\mu$Jy, implying $\alpha - 0.34$. We infer a 5.0 GHz flux density of $241 \pm 28$ $\mu$Jy at this epoch by assuming $\alpha = -0.5$. It is possible that in the soft state 4U 1820–30 sometimes has a steeper radio spectrum than

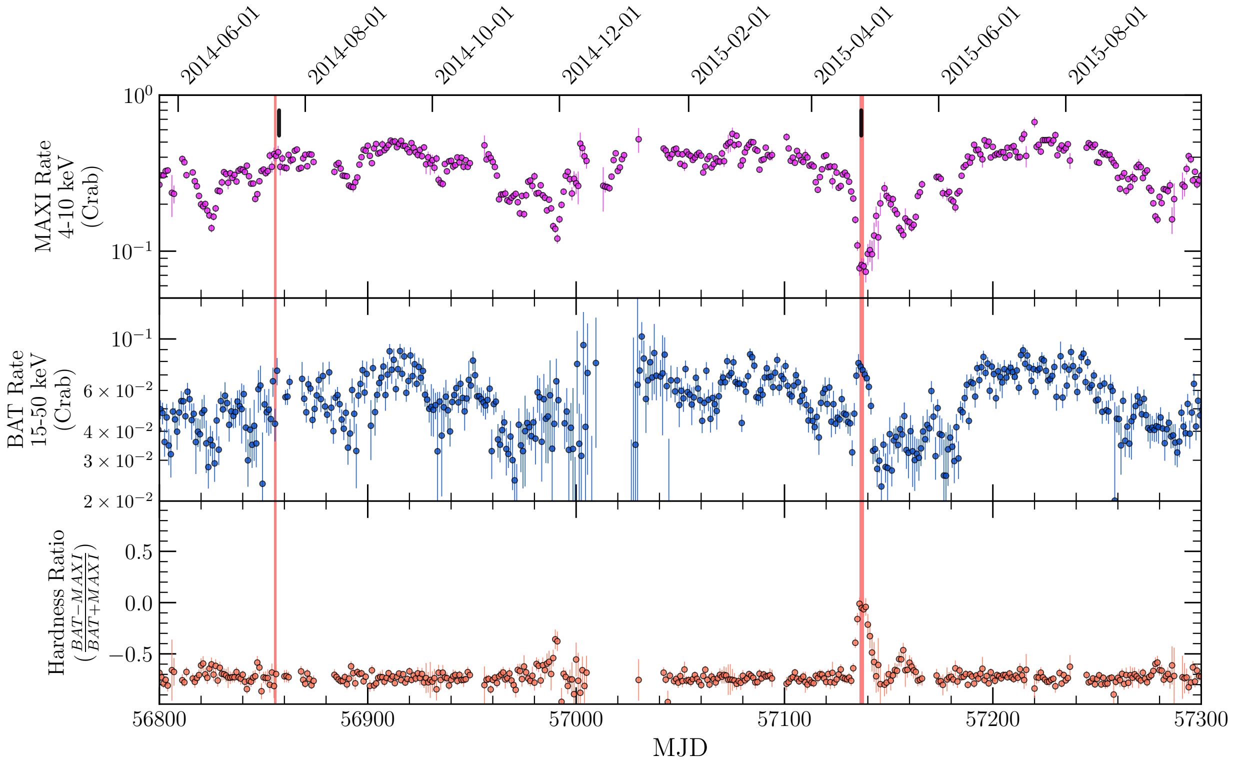

Figure 2.2: 2014 April to 2015 October X-ray light curve of 4U 1820–30 from MAXI (4–10 keV; top) and Swift/BAT (15–50 keV; middle), with hardness ratio in the bottom panel. The epochs of our strictly simultaneous 2015 April Swift/XRT and ATCA data (thick vertical salmon line for radio, short black line for X-ray) as well as the previously published 2014 July quasi-simultaneous radio/X-ray observations (thin vertical salmon line for radio, short black line for X-ray) are also plotted. The new simultaneous data from 2015 April occur during a local minimum in the MAXI flux and a local maximum in the hardness ratio, implying that the system was in the hard island state.

this (Russell et al., 2021), but none of our results depend on the precise value assumed. In Swift/XRT observations obtained two days after the ATCA data, 4U 1820–30 is luminous with $L_X \sim 8 \times 10^{37}$ erg s$^{-1}$. These quasi-simultaneous radio/X-ray observations are also plotted in Figure 3.1. The inferred 5.0 GHz flux density was identical to that in the 2015 data, but at an X-ray luminosity a factor of $\sim 6$ higher, where it is in a location typical of soft accreting neutron stars. Migliari et al. (2004) presented earlier quasi-simultaneous data in a comparable soft state, finding the radio flux density was about a factor of $\sim 2$ lower than in the Díaz Trigo et al. (2017) data. We do not include these earlier data in this paper since the system was only significantly detected in an average of seven epochs, and not in any individual epoch (Migliari et al., 2004), due to the lower sensitivity of ATCA prior to its backend upgrade in 2010.

### 2.3.2 X1850–087 in NGC 6712

X1850–087 was an early discovery of a persistent luminous X-ray source in a Galactic globular cluster (Seward et al., 1976), with a typical $L_X \sim 10^{36}$ erg s$^{-1}$ (Figure 2.3). The source shows Type I X-ray bursts (in't Zand et al., 2019), proving a neutron star primary. X1850–087 is a likely ultracompact binary with a suspected 0.014 d (20.6 min) orbital period, derived from an HST ultraviolet time series (Homer et al., 1996).

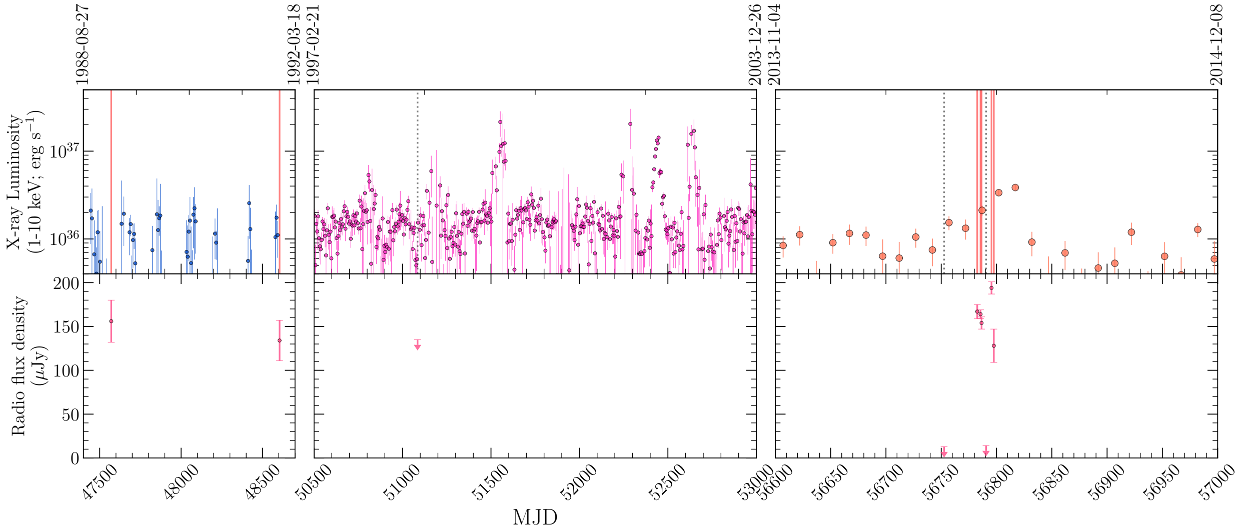

Figure 2.3: Long-term X-ray light curve of X1850–087 (top) with radio flux densities (bottom). The three separate panels show different time ranges observed with different X-ray instruments: Ginga (blue); RXTE (magenta); MAXI (orange), all plotted as 1–10 keV luminosities. Salmon vertical lines correspond to radio detections and grey dashed lines to radio upper limits.

#### 2.3.2.1 2014 Quasi-simultaneous VLA and Swift Data

We obtained VLA observations of NGC 6712 over seven epochs, each of duration 1 or 2 hr, in April and May 2014 shown in Table 2.1. X1850–087 is strongly variable in the radio over this timespan, with a mixture of tight upper limits and clear detections.

First we discuss our quasi-simultaneous VLA and Swift radio and X-ray observations, with the VLA data obtained on 2014 April 5 and the X-ray data on 2014 April 6. The source is not detected with the VLA at either 5.0 or 7.4 GHz during these observations, with $3\sigma$ upper limits of $< 12.9\,\mu$Jy and $< 12.3\,\mu$Jy, respectively. Averaging the subbands gives a $3\sigma$ upper limit of $< 9.0\,\mu$Jy at an average frequency of 6.2 GHz.

The quasi-simultaneous Swift/XRT X-ray observations are well-fit by an absorbed power-law with $\Gamma = 2.30 \pm 0.13$, giving an unabsorbed flux of $(1.6 \pm 0.1) \times 10^{-10}$ erg s$^{-1}$ cm$^{-2}$. This flux corresponds to an X-ray luminosity of $1.2 \times 10^{36}$ erg s$^{-1}$. We note that a photon index of $\Gamma \sim 2.3$ is atypically soft at this X-ray luminosity (Wijnands et al., 2015), perhaps suggesting that the true spectrum is instead a composite that has contributions from both a power law and a thermal disk spectrum. Unfortunately, the quality of the Swift data are not high enough to distinguish between this hypothesis and the simpler single power law. If we try such a two-component fit with the photon index fixed to $\Gamma = 1.7$, both the fit quality and inferred flux are essentially identical, indicating that the presence of a two-component X-ray spectrum is plausible, but unproven. If indeed X1850–087 is in the hard state, then Figure 3.1 shows that this source has the most stringent quasi-simultaneous $3\sigma$ radio continuum upper limit ($L_R \sim 3 \times 10^{28}$ erg s$^{-1}$) for a hard state neutron star LMXB at $L_X 10^{36}$ erg s$^{-1}$.

While X1850–087 is only marginally detected in daily MAXI (4–10 keV) and Swift/BAT (15–50 keV) observations in this time frame, binned light curves do show detections (Figure

| Date<br>(UT) | $\nu_{\rm low}$<br>(GHz) | $S_{\rm low}$<br>($\mu$Jy) | $\nu_{\rm high}$<br>(GHz) | $S_{\rm high}$<br>($\mu$Jy) | $\alpha$ |
|---|---|---|---|---|---|
| 1989 February 19.589 (14.478–14.700) | 4.9 | $156 \pm 24$ (a) | ... | ... | ... |
| 1991 December 15.834 (15.683–15.985) | 4.9 | $134 \pm 23$ (a) | ... | ... | ... |
| 1998 September 29.083 (29.061–29.105) | 4.9 | $< 135$ (a) | ... | ... | ... |
| 2014 April 05.626 (05.590–05.661) | 5.0 | $< 12.9$ | 7.4 | $< 12.3$ | ... |
| 2014 May 05.600 (05.584–05.615) | 5.0 | $167.0 \pm 8.0$ | 7.4 | $202.9 \pm 6.6$ | $+0.50 \pm 0.15$ |
| 2014 May 08.588 (08.552–08.623) | 5.0 | $164.0 \pm 5.0$ | 7.4 | $155.7 \pm 4.6$ | $-0.13 \pm 0.11$ |
| 2014 May 09.497 (09.482–09.512) | 5.0 | $165.3 \pm 6.8$ | 7.4 | $197.0 \pm 6.2$ | $+0.45 \pm 0.13$ |
| 2014 May 13.574 (13.539–13.610) | 5.0 | $< 14.0$ | 7.4 | $< 12.9$ | ... |
| 2014 May 18.492 (18.476–18.507) | 5.0 | $194.2 \pm 7.0$ | 7.4 | $199.1 \pm 7.2$ | $+0.06 \pm 0.13$ |
| 2014 May 20.581 (20.566–20.596) | 5.0 | $127.7 \pm 18.7$ | 7.4 | $155.3 \pm 17.7$ | $+0.50 \pm 0.47$ |

Table 2.2: VLA Radio Observations of X1850–087.
**Note.**
(a) Central frequency 4.9 GHz, not 5.0 GHz.

2.4). These light curves show that there is no meaningful variability in the flux or hardness of X1850–087 in the data surrounding the 2014 April 5–6 radio and X-ray observations, suggesting the quasi-simultaneous Swift/XRT data are representative.

We also delve into the 2014 April 5 radio non-detection by imaging the data in individual 10-min scans, averaging together both basebands in the *uv* plane. The source was undetected in all the individual scans, with a typical per-scan rms of about 9 $\mu$Jy (and hence a per-scan $3\sigma$ limit of $27\mu$Jy). We conclude that the limit in the entire 2 hr block is representative and that the binary is indeed not detected in these radio continuum data at this time.

#### 2.3.2.2 2014 May Data: Detections and Variability

In contrast to the strong radio upper limit in 2014 April, X1850–087 is clearly detected in several other radio observations in 2014 May at $> 10\sigma$ significance (Table **??**). Of the six VLA epochs obtained during May 2014, in five of these X1850–087 has a flux density $> 100$ $\mu$Jy. In one epoch (2014 May 13), X1850–087 is again not detected (with a formal $3\sigma$ upper limit of $< 9.5\mu$Jy at a combined average frequency of 6.2 GHz), but is well-detected in bracketing observations on May 9 and May 18. This demonstrates that the radio flux density of X1850–087 is changing by at least a factor of $\sim 20$ in just a few days.

While there is no Swift/XRT X-ray coverage of these 2014 May epochs, the binned MAXI and Swift/BAT light curves indicate that an X-ray brightening and a transition to a softer state occurred around the time of these 2014 May VLA observations (Figure 2.4). Hence, one interpretation of the overall higher radio flux density from 2014 May 5–9 and May 18–20 is that it is associated with this transition, perhaps due to the launching of discrete ejecta. A challenge to this simple interpretation is the non-detection on May 13, which would require a separate transition to the baseline fainter harder state (or perhaps an intermediate hard state) between May 9 and 13 and a re-flaring to a softer higher state by May 18. As we lack daily Swift/XRT data during this period we cannot definitively rule out this possibility, but it is not supported by the binned MAXI and Swift/BAT light curves, and would also represent phenomenology not previously observed in the Rossi X-ray Timing Explorer (RXTE) light curve for the source (see next subsection).

Absent this fast flaring behavior, we know of no straightforward explanation for such dramatic variability on these timescales in an ultracompact system, which are much longer than the 0.014 d (20.6 min) orbital period but much shorter than, for example, the 100 d superorbital periods observed in some other ultracompact systems such as 4U 1820–30 (Section 3.1).

In the May 13 radio data for X1850–087, as in the April 5 data, the source is not detected in 10-min individual scans during the 2 hour observation block. This is consistent with the idea that any orbital variations—which ought to be averaged out over individual blocks that represent $\sim 6$ orbital periods—are not the primary cause of the variability of X1850–087.

We also imaged the individual scans for the observing blocks adjacent to the May 13 block in which the source was not detected. Each of these is a 1-hr block with five 8-min scans on source. On May 9, there is no evidence for significant variation among the scans. On May 18, X1850–087 is brighter in the last two scans than the first three at a formal level of about $3.5\sigma$ (5.0 GHz flux density of $235 \pm 17\mu$Jy in the last two, compared to $168 \pm 9\mu$Jy in the first three). Given its marginal significance, we do not attach too much import to the change, but if it were a real increase in the flux density, it could be short-term variability due to a recent jet ejection event.

We report spectral indices in Table **??** for our 2014 May observations of X1850–087. The spectral index ranged from inverted (brighter at higher frequencies) to flat, varying on short timescales: between May 5 and May 8 the source changed from an inverted spectral index ($\alpha = +0.50 \pm 0.15$) to a flatter value ($\alpha = -0.13 \pm 0.11$), then quickly back to inverted ($\alpha = 0.46 \pm 0.13$) on May 9, just one day later. The detection on May 18 was likewise flat, with $\alpha = +0.06 \pm 0.13$. We also calculated the per-scan spectral indices on May 18, finding a mean value of $\alpha = -0.04 \pm 0.20$ for the three early scans and $\alpha = +0.30 \pm 0.16$ for the two final scans. This could be consistent with a transition to more inverted emission during the putative flux density increase at the end of the May 18 observing block, though the evidence for a spectral index change is not formally significant. We discuss possible interpretations of the spectral index variations between different epochs in Section 4.2.3.

#### 2.3.2.3 Other Radio and X-ray Data

To improve the time baseline in the radio, we also make use of archival VLA data for X1850–087, reducing all of the C band data taken in the high-resolution (A or B) VLA configurations. This resulted in three additional epochs, all at 4.9 GHz, spanning 1989–1998 (Table **??**). In 1989 February and 1991 December, X1850–087 was clearly detected, with flux densities consistent with our 2014 detections. In 1998 September, the source was not

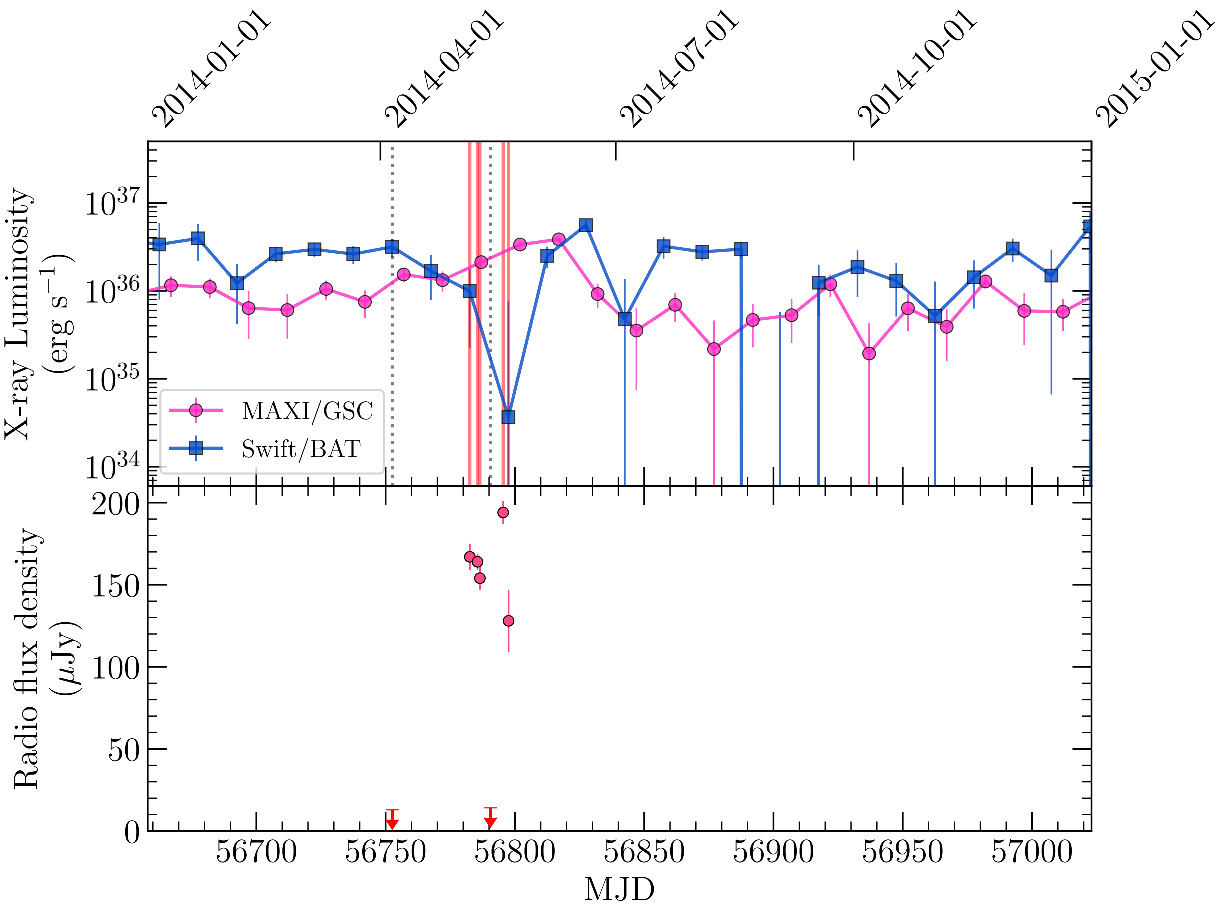

Figure 2.4: 2014 X-ray light curve of X1850–087 (top) with radio flux densities (bottom). Both MAXI (4–10 keV) and Swift/BAT (15–50 keV) X-ray light curves are shown. As in Figure 2.3, salmon vertical lines correspond to radio detections and grey dashed lines correspond to radio upper limits.

detected, but the $3\sigma$ upper limit ($< 135\mu$Jy) is not particularly constraining as to whether order-of-magnitude variability was present in these older data.

Some previous papers on the 1989 February radio detection have claimed that X1850–087 is spatially resolved in these data (Lehto et al., 1990; Machin et al., 1990), which if true would have important implications for its interpretation. In our re-reduction of these data, given the moderate signal-to-noise of the source, we find that either a point source or extended morphology offer reasonable fits. In our substantially deeper 2014 detections while the VLA was in its highest resolution A configuration, we find that in all epochs the morphology of

X1850–087 is consistent with a point source.

There is at least partial X-ray data at these earlier epochs to contextualize these radio detections and limits. A Ginga/ASM (1–20 keV) light curve is available from 1987 March to 1991 October, and while it does not have spectral information, this X-ray light curve shows only modest variability (Figure 2.3). Two epochs of Ginga/LAC data in this time interval, from 1989 April and 1990 Sep, suggest an unabsorbed 1–10 keV luminosity of $L_X \sim 1.8 \times 10^{36}$ erg s$^{-1}$ (Kitamoto et al., 1992), consistent with the Swift/XRT data from 2014.

RXTE/ASM (1–10 keV) offers a well-sampled light curve of X1850–087 from 1995 to 2012, with evidence for a number of distinct episodes of brightening on typical timescales of weeks to months, as well as lower-level variability. In the vicinity of the 1998 September radio upper limit, the source has an X-ray flux typical of the long-term value (Cartwright et al., 2013).

The most notable feature of the long-term X-ray light curve of X1850–087 is that it spends a relatively short amount of time in obvious bright states. As a rough estimate, we use the RXTE/ASM light curve, which has the best sampling and decent sensitivity of the long-term light curves. If we make a somewhat arbitrary designation that the source is in a bright state if the X-ray luminosity is $3 \times 10^{36}$ erg s$^{-1}$, then it spends only $\sim 6\%$ in such bright states (see also Cartwright et al. 2013). This percentage increases to $\sim 15\%$ if a more conservative luminosity of $2 \times 10^{36}$ is used, though Figure 2.3 shows that this value would likely also encompass periods of typical persistent activity outside of a bright state. Hence the long-term X-ray light curve shows that it is unlikely that two random radio continuum observations in 1989 and 1991 would have been taken during this uncommon flaring/bright state purely by chance.

Overall, we conclude that a straightforward flaring/state transition model for the dramatic radio variability of X1850–087 cannot be firmly ruled out. However, such an scenario also does not readily explain the data.

### 2.3.3 XB1832–330 in NGC 6652

XB1832–330 is a persistent X-ray source first associated with the globular cluster NGC 6652 in 1990 (Predehl et al., 1991) and with evidence for Type I X-ray bursts (in't Zand et al., 1998; Mukai & Smale, 2000). Based on its X-ray spectrum and the lack of a bright optical counterpart, it was long argued to be an ultracompact LMXB (e.g., Heinke et al. 2001; Parmar et al. 2001). However, Engel et al. (2012) used Gemini optical photometry to argue for an orbital period of $0.0895 \pm 0.0001$ d (2.15 hr), suggesting instead a low-mass main sequence donor.

Here we report a $3\sigma$ VLA radio upper limit of $< 6.6\mu$Jy at 10 GHz on 2017 May 22. While we have strictly simultaneous Chandra/ACIS-S observations, these are piled up and had to be specially fit (as described in Section 2.3). An absorbed `Nthcomp` model provides a good fit ($\chi^2$/dof $= 199/186 \sim 1.07$) with an unabsorbed X-ray flux of $(1.9 \pm 0.1) \times 10^{-11}$ erg s$^{-1}$ cm$^{-2}$. The system was in the hard state with $\Gamma = 1.62 \pm 0.14$.

The X-ray flux reported above corresponds to a luminosity of $L_X \sim 2 \times 10^{35}$ erg s$^{-1}$. This value is somewhat fainter than that reported for the 2011 Chandra observations of Stacey et al. (2012), and much lower than the $L_X 10^{36}$ erg s$^{-1}$ that the source showed when observed from 1990 through 2010 (e.g., Predehl et al. 1991; Parmar et al. 2001; Sidoli et al. 2008; Cartwright et al. 2013). RXTE/PCA Bulge Scan data[5] suggests that a transition to a fainter state occurred beginning around 2011 February. There is some evidence from HEAO-1 observations that in the late 1970s the luminosity was closer to $\sim 10^{35}$ erg s$^{-1}$

---

[5] `https://asd.gsfc.nasa.gov/Craig.Markwardt//galscan/html/R_1832-330.html`

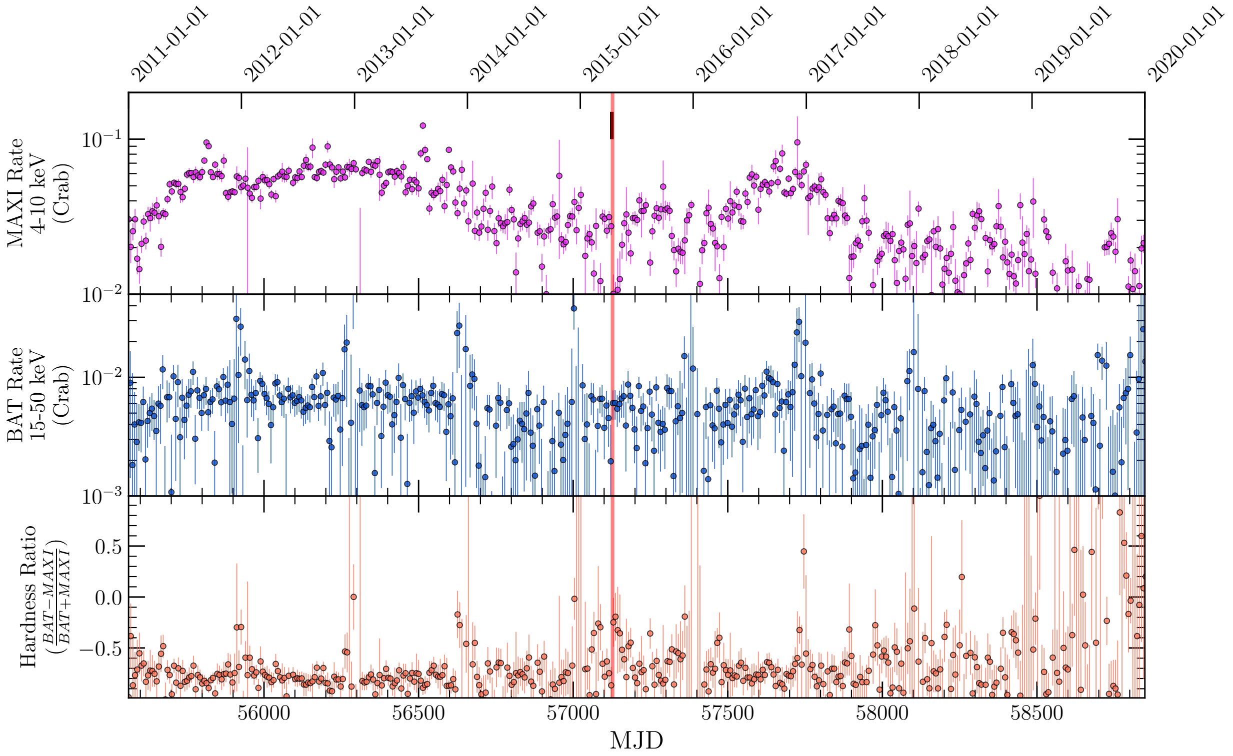

Figure 2.5: Long-term X-ray light curve of 4U 1746–37 from MAXI (4–10 keV; top) and Swift/BAT (15–50 keV; middle), with hardness ratio in the bottom panel. The epoch of our quasi-simultaneous 2015 April Swift/XRT and ATCA data (thick vertical salmon line for radio, short black line for X-ray) are marked.

(Hertz & Wood, 1985), implying that similar persistent luminosity changes have occurred in the past.

Our deep radio upper limit at $L_X \sim 2 \times 10^{35}$ erg s$^{-1}$ puts XB1832–330 among the sources with the most constraining simultaneous radio data at these “low” persistent emission levels.

### 2.3.4 4U 1746–37 in NGC 6441

4U 1746–37 is a persistent atoll X-ray source in NGC 6441, with an orbital period of 0.215 d (5.14 hr) as inferred from RXTE X-ray dips (Bałucińska-Church et al., 2004). The radio data implicitly average over several orbital periods, though the dips have maximal X-ray amplitudes of $\sim$ 25%. The dipping nature of the source suggests an inclination 60°, possibly as high as $\sim 75-80^\circ$.

We report a $3\sigma$ ATCA 5.5 GHz radio upper limit of $< 13.7\mu$Jy on 2015 April 14/15. Quasi-simultaneous Swift X-ray observations on 2015 April 13 are best-fit by a composite `Nthcomp`+`diskbb` model, yielding an unabsorbed X-ray flux of $(8.6 \pm 2.0) \times 10^{-10}$ erg s$^{-1}$ cm$^{-2}$. This spectrum and flux are consistent with that of the soft/banana-like state in which 4U 1746–37 spends most of its time (e.g., Jonker et al. 2000; Muñoz-Darias et al. 2014). The Swift/BAT and MAXI X-ray light curves around the time of the X-ray and radio observations (Figure 2.5) are noisy, requiring coarse 10-day binning, and somewhat difficult to interpret. The single MAXI bin closest in time to the radio observation has a low flux, and combined with the Swift/BAT detection in the corresponding bin, this could suggest the system was in an intermediate hard state. On the other hand, the Swift/BAT flux was no higher than any surrounding bin, and on average the source is in a relatively soft state around this time. Hence we proceed assuming that the system is indeed in the soft/banana state at the time of our radio data.

While 4U 1746–37 shows both bursts and flares, the quasi-simultaneous 2015 April Swift/XRT flux corresponds to an X-ray luminosity of $\sim 2 \times 10^{37}$ erg s$^{-1}$, consistent with a typical non-bursting value for the source (e.g., Christian & Swank 1997).

The non-detection of this source in radio continuum emission is notable: it has one of the most constraining radio upper limits for a soft state neutron star at $L_X > 10^{37}$ erg s$^{-1}$ (Figure 3.1), suggesting either relatively faint radio emission from 4U 1746–37 in this soft state or perhaps the quenching of its jet.

### 2.3.5 GRS 1747–312 in Terzan 6

#### 2.3.5.1 Radio and X-ray Measurements

GRS 1747–312 is a transient LMXB first observed in 1990 by Granat (Pavlinsky et al., 1994). The compact object is a neutron star that shows Type I X-ray bursts (in't Zand et al., 2003b). Observations of X-ray eclipses have allowed the determination of a precise orbital period of 12.360 hr (in't Zand et al., 2003a). GRS 1747–312 has unusually frequent outbursts, clustering with a recurrence time around 4.5 months, though some outbursts occur much more quickly or slowly than this typical value. While the optical companion is unknown—due primarily to the high optical extinction toward Terzan 6—the relatively long orbital period and fast recurrence time suggest a somewhat high mass transfer rate from a subgiant donor (in't Zand et al., 2003a).

Here we report three quasi-simultaneous (within $\sim 1$ d) epochs of radio and X-ray observations of GRS 1747–312. The ephemerides of the X-ray eclipses are known with sufficient precision (in't Zand et al., 2003a) that we can determine with certainty that none of the X-ray data discussed below occur during eclipses. For one of the five VLA epochs (2018 June 3), and for the ATCA observations, there is a partial overlap with the predicted eclipse times. The radio emission at these frequencies (5/7 GHz for VLA; 5.5/9 GHz for ATCA) is unlikely to be eclipsed even during X-ray eclipses (Maccarone et al., 2020), and in any case only a small amount—about 13% of the 2018 June 3 VLA epoch and 4% of the ATCA data—was taken during a predicted eclipse, so does not affect our results or conclusions.

In ATCA observations that began 2015 April 17 (labeled as 1 in Figure 3.1), the binary is well-detected with 5.5 and 9.0 GHz flux densities of $213.3 \pm 5.1\,\mu$Jy and $172.4 \pm 5.2\,\mu$Jy, respectively, implying a radio spectral index $\alpha = -0.43 \pm 0.08$. We use this well-measured spectral slope to infer a 5.0 GHz flux density of $221.1 \pm 6.4\,\mu$Jy. The data quality of all three Swift/XRT observations discussed in this section (including the quasi-simultaneous one obtained on 2015 April 16) is relatively low, and fitting an absorbed power-law to these X-ray data gives a strong degeneracy between $\Gamma$ and $N_H$. The presence of variable dips for this source means that a constant $N_H$ cannot necessarily be assumed. Therefore we have taken the approach of fitting two models to each of the Swift/XRT observations: one with fixed $\Gamma$ and free $N_H$, and the other with both $\Gamma$ and $N_H$ fixed, the latter to the estimated foreground of $1.4 \times 10^{22}$ cm$^{-2}$. Motivated by the typical photon indices for low-mass X-ray binaries at these X-ray luminosities and the spectral fitting results of (Vats et al., 2018) for the source in quiescence, for the models with $\Gamma$ fixed, we assume $\Gamma = 1.7$.

For the 2015 April 16 Swift/XRT data, the free $N_H$ fit has $N_H = 7.8^{+6.4}_{-4.0} \times 10^{22}$ cm$^{-2}$ and an unabsorbed X-ray flux of $5.3^{+4.0}_{-2.4} \times 10^{-12}$ erg s$^{-1}$ cm$^{-2}$, corresponding to $L_X = 2.9^{+2.2}_{-1.3} \times 10^{34}$ erg s$^{-1}$ at the assumed distance of 6.8 kpc. For the fit with both $N_H$ and $\Gamma$ fixed, we find an unabsorbed flux of $2.1^{+1.0}_{-0.8} \times 10^{-12}$ erg s$^{-1}$ cm$^{-2}$ ($L_X = 1.2^{+0.5}_{-0.4} \times 10^{34}$ erg s$^{-1}$). These two flux estimates are consistent within the uncertainties; we plot the former (free $N_H$) fit in Figure 3.1, but none of our conclusions depend on this choice.

At this first quasi-simultaneous epoch, GRS 1747–312 is the most radio-luminous neutron star LMXB ever observed at X-ray luminosities $< 10^{35}$ erg s$^{-1}$, with a 5.0 GHz radio luminosity of $(6.1 \pm 0.2) \times 10^{28}$ erg s$^{-1}$. It sits near the upper envelope of the well-defined black hole radio/X-ray correlation (Figure 3.1).

Two VLA epochs in 2018 were obtained quasi-simultaneously with additional Swift/XRT data. On 2018 March 25 (labeled as 2 in Figure 3.1), GRS 1747–312 is not detected with the VLA at either 5.0 or 7.1 GHz, with $3\sigma$ upper limits of $< 12.9\,\mu$Jy and $< 11.7\,\mu$Jy respectively. We fit the Swift/XRT observations on 2018 March 26 using the two models discussed above:

$\Gamma = 1.7$ and $N_H$ free, or $\Gamma = 1.7$ and $N_H = 1.4 \times 10^{22}$ cm$^{-2}$. For the former model we find $N_H = 3.6^{+4.2}_{-2.1} \times 10^{23}$ cm$^{-2}$ and an unabsorbed X-ray flux of $8.0^{+13.6}_{-4.8} \times 10^{-12}$ erg s$^{-1}$ cm$^{-2}$, equivalent to $L_X = 4.4^{+7.5}_{-2.6} \times 10^{34}$ erg$^{-1}$. For the fixed $N_H$ model, the unabsorbed flux is $1.0^{+0.6}_{-0.4} \times 10^{-12}$ erg s$^{-1}$ ($L_X = 5.5^{+3.3}_{-2.4} \times 10^{33}$ erg$^{-1}$). For this observation, the X-ray fluxes from the two models are not quite consistent within the uncertainties. We conservatively plot the free $N_H$ fit in Figure 3.1, but again none of our conclusions depend on the precise X-ray luminosity plotted for this radio upper limit.

GRS 1747–312 is again detected in the radio on 2018 April 30 (labeled as 3 in Figure 3.1) with 5.0 and 7.1 GHz flux densities of $26.9 \pm 4.3\,\mu$Jy and $32.1 \pm 4.1\,\mu$Jy respectively, and a measured spectral index of $\alpha = +0.51 \pm 0.57$. In quasi-simultaneous Swift/XRT data from 2018 May 1, it is marginally detected, with an unabsorbed X-ray flux from the free $N_H$ model of $0.9^{+1.1}_{-0.6} \times 10^{-12}$ erg s$^{-1}$ cm$^{-2}$ ($N_H = 0.5^{+1.8}_{-0.5} \times 10^{22}$ cm$^{-2}$) and a fixed $N_H$ flux of $(1.3^{+1.2}_{-0.8}) \times 10^{-12}$ erg s$^{-1}$ cm$^{-2}$. Since the former fit yields an $N_H$ below the expected foreground, for this epoch we use the fixed $N_H$ result in Figure 3.1, again emphasizing that this choice does not affect any of our conclusions. This gives $L_X = 7.1^{+6.4}_{-4.4} \times 10^{33}$ erg s$^{-1}$.

The VLA non-detection in March 2018 is more typical of the upper limits or detections for neutron star LXMBs at $L_X$ of $\sim 5 \times 10^{33}$ to $5 \times 10^{34}$ erg s$^{-1}$. However, the VLA detection about a month later (2018 April 30), at a fainter X-ray and radio luminosity than the bright 2015 detection, again approaches the regime more typically occupied by black hole LMXBs. In subsequent VLA epochs, taken from 2018 May 21 to June 3, the source is well-detected at a comparable radio luminosity to the first VLA detection (Table 2.3), also showing modest (less than a factor of $\sim 2$) variability. We have no simultaneous X-ray data at these latter radio epochs. We stack the four detected VLA epochs in the $uv$ plane to get our best estimate of the VLA source position (Table 2.3). The spectral index in the stack is $\alpha = -0.51 \pm 0.28$, entirely consistent with the ATCA value. This suggest a similar origin for the radio continuum emission in both datasets, despite a factor of $\sim 6$ drop in radio luminosity.

As we discuss below for AC 211 in M15 (Section 3.6.1), given the high orbital inclination of GRS 1747–312, it is possible that its unabsorbed X-ray luminosity is being underestimated, which might make GRS 1747–312 somewhat less of an outlier in the radio/X-ray correlation. Mitigating against this possibility is that for GRS 1747–312 the central accretor is visible (unlike the case for AC 211), implying less "extra" obscuration for GRS 1747–312, if any.

| Date (UT) | $\nu_{\rm low}$ (GHz) | $S_{\rm low}$ ($\mu$Jy) | $\nu_{\rm high}$ (GHz) | $S_{\rm high}$ ($\mu$Jy) | $\alpha$ |
|---|---|---|---|---|---|
| 2015 April 18.250 (17.542–18.958) | ATCA/5.5 | $213.3 \pm 5.1$(a) | ATCA/9.0 | $172.4 \pm 5.2$(b) | $-0.43 \pm 0.08$ |
| 2018 March 25.594 (25.557–25.630) | VLA/5.0 | $< 12.9$ | VLA/7.1 | $< 11.7$ | ... |
| 2018 April 30.380 (30.344–30.417) | VLA/5.0 | $26.9 \pm 4.3$ | VLA/7.1 | $32.1 \pm 4.1$ | $+0.47 \pm 0.56$ |
| 2018 May 21.307 (21.271–21.344) | VLA/5.0 | $47.4 \pm 4.2$ | VLA/7.1 | $26.0 \pm 4.3$ | $-1.77 \pm 0.56$ |
| 2018 May 31.416 (31.401–31.432) | VLA/5.0 | $42.5 \pm 6.0$ | VLA/7.1 | $51.3 \pm 6.0$ | $+0.53 \pm 0.50$ |
| 2018 June 03.270 (03.255–03.285) | VLA/5.0 | $38.4 \pm 6.4$ | VLA/7.1 | $31.5 \pm 6.7$ | $-0.63 \pm 0.82$ |
| 2018 April 30–June 3(c) | VLA/5.0 | $38.4 \pm 2.3$(d) | VLA/7.1 | $32.2 \pm 2.5$ (e) | $-0.51 \pm 0.29$ |

Table 2.3: Radio Observations of GRS 1747–312.

**Note.**

(a) ATCA/5.5 GHz ICRS position of 17:50:46.9139(122) –31:16:29.04(42).

(b) ATCA/9.0 GHz ICRS position of 17:50:46.9145(82) –31:16:29.14(28).

(c) A stack of the four detected VLA epochs in the *uv* plane.

(d) VLA/5.0 GHz ICRS position in stack of 17:50:46.9119(35) –31:16:29.202(91).

(e) VLA/7.1 GHz ICRS position in stack of 17:50:46.9112(25) –31:16:29.159(66)

#### 2.3.5.2 Are We Sure We are Detecting GRS 1747–312?

It is worth considering whether we are sure that the radio and X-ray fluxes indeed reflect those of GRS 1747–312. The source was not in X-ray outburst during any of our observations, and the X-ray data were taken outside of eclipse.

While no other luminous X-ray sources are definitively known in Terzan 6, there are some puzzling observations that could be consistent with the existence of sources other than

GRS 1747–312. In a 2009 Suzaku observation, Saji et al. (2016) observe a single source with $L_X \sim 6 \times 10^{34}$ erg s$^{-1}$, but see no evidence for an eclipse at the predicted time for GRS 1747–312, leading them to argue that this X-ray emission might arise from a different source.

Only a single X-ray source is evident in our Swift/XRT images of Terzan 6, and its position is consistent with the Chandra/HRC position of GRS 1747–312 (in't Zand et al., 2003b). But the Swift position is at best only constrained at the level of $\sim$ 2–3, so this association is not definitive in the dense environment of a globular cluster.

The position of the counterpart radio source in our ATCA and VLA observations is much better constrained. Since this source shows radio variability, has a radio spectral slope consistent with a LMXB, and already has a relatively high ratio of radio to X-ray luminosity, it seems fair to assert that this radio emission indeed arises from the same source as in the quasi-simultaneous Swift/XRT observations. The ATCA and VLA positions of the source can be found in Table **??**, where we have conservatively assumed the $1\sigma$ uncertainties to be 10% of the beam. The ATCA and VLA positions are entirely consistent with each other, and the VLA position is about 0.7 from the best-fit Chandra/HRC position[6]. This X-ray position has a formal 95% uncertainty of 0.4 (in't Zand et al., 2003b) based on an astrometric solution from three X-ray sources in the field. Hence, formally our radio continuum position is inconsistent with the Chandra one. Since absolute astrometry with Chandra is challenging, it seems plausible that the uncertainty is slightly underestimated, which could reconcile the positions.

A piece of evidence in favor of this argument is that neither the Chandra/HRC position of GRS 1747–312 nor our radio position are right at the center of the cluster: rather, they

---

[6] This is not due to the proper motion of Terzan 6, which only implies a change of about 0.1 per coordinate between the X-ray epoch 2000 and and radio epochs of 2015–2018 (Vasiliev, 2019).

are northwest of the center in an HST/WFC3 F110W image (corrected to ICRS using Gaia DR2 stars), perhaps $\sim 1.4$–2 from the center and approaching the edge of the core. While it is possible that there are two unrelated X-ray binaries only 0.7 from each other but offset from the cluster center, an unrelated binary could plausibly be located anywhere in the core.

Finally, an XMM observation of Terzan 6 taken when GRS 1747–312 was not in outburst showed evidence for a single X-ray source with $L_X \sim 10^{33}$ erg s$^{-1}$ (assuming our distance of 6.8 kpc). A spectral fit to this source required a two-component model with both a neutron star atmosphere and a hard power law, consistent with ongoing low-level accretion onto a neutron star (Vats et al., 2018). This X-ray luminosity is well below that of our Swift/XRT observations, which range from $L_X \sim 7 \times 10^{33}$ to $4 \times 10^{34}$ erg s$^{-1}$. Hence, to explain our Swift/XRT data, a non-GRS 1747–312 source would need to have a typical luminosity (in both 2015 and 2018) around $L_X \sim 10^{34}$ erg s$^{-1}$. Being in neither quiescence nor full outburst, such luminosities are quite unusual for LMXBs, but are not unexpected for GRS 1747–312 given its very frequent outbursts. A hypothetical non-GRS 1747–312 source would also need to be X-ray and radio variable, as well as being very close to the position of GRS 1747–312. This verges on implausibility, and the most parsimonious explanation—pending, of course, additional X-ray and radio data—is that the only X-ray binary clearly detected thus far in Terzan 6 is indeed GRS 1747–312.

### 2.3.6 Sources in M15: AC 211, X-2, and X-3

Here we discuss the persistent sources AC 211 and M15 X-2 together with the very faint X-ray transient M15 X-3, since all the analysis comes from identical datasets. All the radio flux densities for our VLA data can be found in Table 2.4.

#### 2.3.6.1 AC 211

AC 211 (X2127+119) is an LMXB with a 17.1 hr period (Ilovaisky et al., 1993). It is one of the most famous accretion disk corona sources, where an edge-on inclination leads to the outer disk blocking the view of the central accretion flow, and only scattered emission is observed. The compact object is generally assumed to be a neutron star but due to the obscuration this has not been confirmed, since the normal identification tools (e.g., Type I X-ray bursts) cannot be used. AC 211 is a variable source that shows eclipses and flares (e.g., Hannikainen et al. 2005), with milliarcsecond-scale radio outflows or ejection events observed during outbursts (Kirsten et al., 2014).

AC 211 is detected in all five epochs of radio continuum imaging in 2011 (see Table 2.4) and is strongly variable, with its 5.0 GHz flux density ranging from 271 $\mu$Jy to 794 $\mu$Jy on timescales as short as a few days. Radio eclipses, while a priori unlikely at these frequencies (Maccarone et al., 2020), are one possible explanation for this variability. Unfortunately, the existing ephemerides (Ioannou et al., 2003) extrapolated to the epoch of observation are not of sufficient precision, with a $1\sigma$ uncertainty of 0.23 d. While the absolute phase cannot be ascertained, the better-determined relative phases of the three low flux density epochs ($< 300\mu$Jy) also do not line up, with a spread of $\phi = 0.35$ in the mid-exposure times. Hence, if radio eclipses are the main explanation for the variability, they would need to last for longer than a third of the orbit, which is quite unlikely. Improved ephemerides would allow a test of this scenario.

In the single quasi-simultaneous epoch, we find an unabsorbed Chandra/HRC X-ray flux of $(4.5 \pm 0.1) \times 10^{-10}$ erg s$^{-1}$ cm$^{-2}$ (using the parameters of the power-law model of White & Angelini 2001), equivalent to $(5.7 \pm 0.1) \times 10^{36}$ erg s$^{-1}$, and a 5.0 GHz radio flux density of $292.0 \pm 6.3$ $\mu$Jy. This places it among the more radio-luminous neutron star LMXBs. At the higher, non-simultaneous value of 794 $\mu$Jy, the radio luminosity is a factor of 2.7 higher and hence more typical of stellar-mass black holes than neutron stars, though this higher radio flux density could be associated with a flare rather than steady emission.

It is worth noting that the X-ray luminosity measurement is almost certainly an underestimate, given the obscuration that prevents us from seeing the central source; the true $L_X$ could be at least an order of magnitude higher than we estimate. We indicate this in Figure 3.1 by plotting the $L_X$ measurement as a lower limit. Nonetheless, even at a much higher value of $L_X$, AC 211 would still be the among the most radio-luminous accreting neutron stars observed, especially in the latter non-simultaneous epoch.

One possible explanation is that AC 211 has an intrinsic $L_X$ that is around two orders of magnitude higher than observed and is a "Z source" accreting near the Eddington luminosity. The nearest and best-studied member of this class, Sco X-1, shows rapid variations in radio flux density and spectral index that are somewhat similar to those that we observe in AC 211 (Hjellming et al., 1990; Fomalont et al., 2001).

Another, speculative possibility is that AC 211 contains a black hole rather than a neutron star, which could potentially explain its radio loud nature. This is statistically unlikely, and evidence from optical spectroscopy tends to favor a neutron star primary (van Zyl et al., 2004a,b), but this prospect cannot be definitively ruled out.

#### 2.3.6.2 M15 X-2

White & Angelini (2001) used Chandra data to solve the mystery of why the obscured source AC 211 occasionally showed X-ray bursts that ought not to have been visible: these bursts are associated with a very nearby (separated by $< 3$) luminous LMXB, M15 X-2.

White & Angelini (2001) found an ultraviolet-bright counterpart to M15 X-2 with a 23-min periodicity identified with the orbital period (Dieball et al., 2005), showing that M15 X-2 is an ultracompact X-ray binary—one of only 4 confirmed persistent ultracompact systems known among Galactic globular clusters.

M15 X-2 had bright flaring events in both 2011 and 2013 (Sivakoff et al., 2011; Pooley & Homan, 2013), with X-ray bursts detected during both events (Negoro et al., 2016). The 2011 flare is the one covered by the same five epochs of VLA data as for AC 211. M15 X-2 was strongly variable during this event (see Table **??**), dropping from a 5.0 GHz flux density $\sim 150$ to $64\mu$Jy from 2011 May 22 to May 26, then back up to $205.0 \pm 6.3\mu$Jy on 2011 May 30. When re-visited in late August 2011, only upper limits were found, equivalent to a $3\sigma$ upper limit of $< 12.7\mu$Jy at 5.0 GHz if both non-detection epochs are combined.

This radio time series clearly shows that the data from 2011 May 30 reflect an elevated level of radio emission during the brightening event. These data share the same quasi-simultaneous Chandra/HRC dataset used for AC 211. At this epoch the unabsorbed Chandra flux was $(9.46 \pm 0.03) \times 10^{-10}$ erg s$^{-1}$ cm$^{-2}$ (using the power-law model of White & Angelini 2001), equivalent to $L_X = 1.2 \times 10^{37}$ erg s$^{-1}$. The radio/X-ray luminosity ratio on 2011 May 30 for M15 X-2 is high, close to the upper envelope of other accreting neutron star binaries observed at this X-ray luminosity.

We note that since these Chandra data were obtained with HRC, no spectral information was available to assess the state of M15 X-2 at this epoch. Instead, we analyze a Swift/XRT observation from 2011 May 30 which is strictly simultaneous with this VLA epoch. The Swift data has lower spatial resolution than Chandra and hence also includes AC 211. Since the count rate of AC 211 in the Chandra/HRC data is about 10% of that of M15 X-2, it makes a small but non-negligible contribution to the Swift/XRT spectrum. Using this relative count rate and the power-law spectral model of White & Angelini (2001) for AC 211, we fit a combination of AC 211 and M15 X-2 to the Swift spectrum. We find that M15 X-2 is well-fit by a composite disk (`diskbb`) + power-law model ($\Gamma = 1.6 \pm 0.1$) with an unabsorbed X-ray flux of $(1.04 \pm 0.04) \times 10^{-9}$ erg s$^{-1}$ ($L_X = 1.3 \times 10^{37}$ erg s$^{-1}$). About three quarters of the flux in this band is contributed by the power-law, suggesting that M15 X-2 is closer to the hard state than the soft state at the time of the radio observations that are plotted in Figure 3.1. The radio spectral index on 2011 May 30 was $\alpha = -0.02 \pm 0.12$, consistent with the presence of a compact jet at this epoch (see additional discussion in Section 4.2.1).

For additional context, Figure 2.6 shows the 2011–2014 MAXI and Swift/BAT X-ray light curves for M15. The 2011 and 2013 M15 X-2 flaring events are clearly visible in the MAXI X-ray light curve. The BAT data are noisy even when heavily binned, and AC 211 likely makes a substantial or even dominant contribution to the hard X-ray flux at all epochs, making it difficult to quantitatively interpret the plotted hardness ratio. Given the results of the Swift/XRT spectral analysis above, and that the 2011 May 30 radio data were obtained on the rise to peak, a reasonable interpretation is that these data were taken during a transition from a hard state to a softer one, with the jet not yet quenched.

## 2.4 Discussion

### 2.4.1 X-ray and Radio Luminosity: More Scatter Than Relation

It is well-established that many black hole LMXBs accreting in the low/hard state (below a few percent of the Eddington rate; Maccarone 2003) show a consistent relationship between their luminosities in the X-ray ($L_X$) and the radio ($L_R$) close to $L_R \propto L_X^{0.6-0.7}$ (e.g., Hannikainen et al. 1998; Gallo et al. 2003; Corbel et al. 2013; Gallo et al. 2018, see also

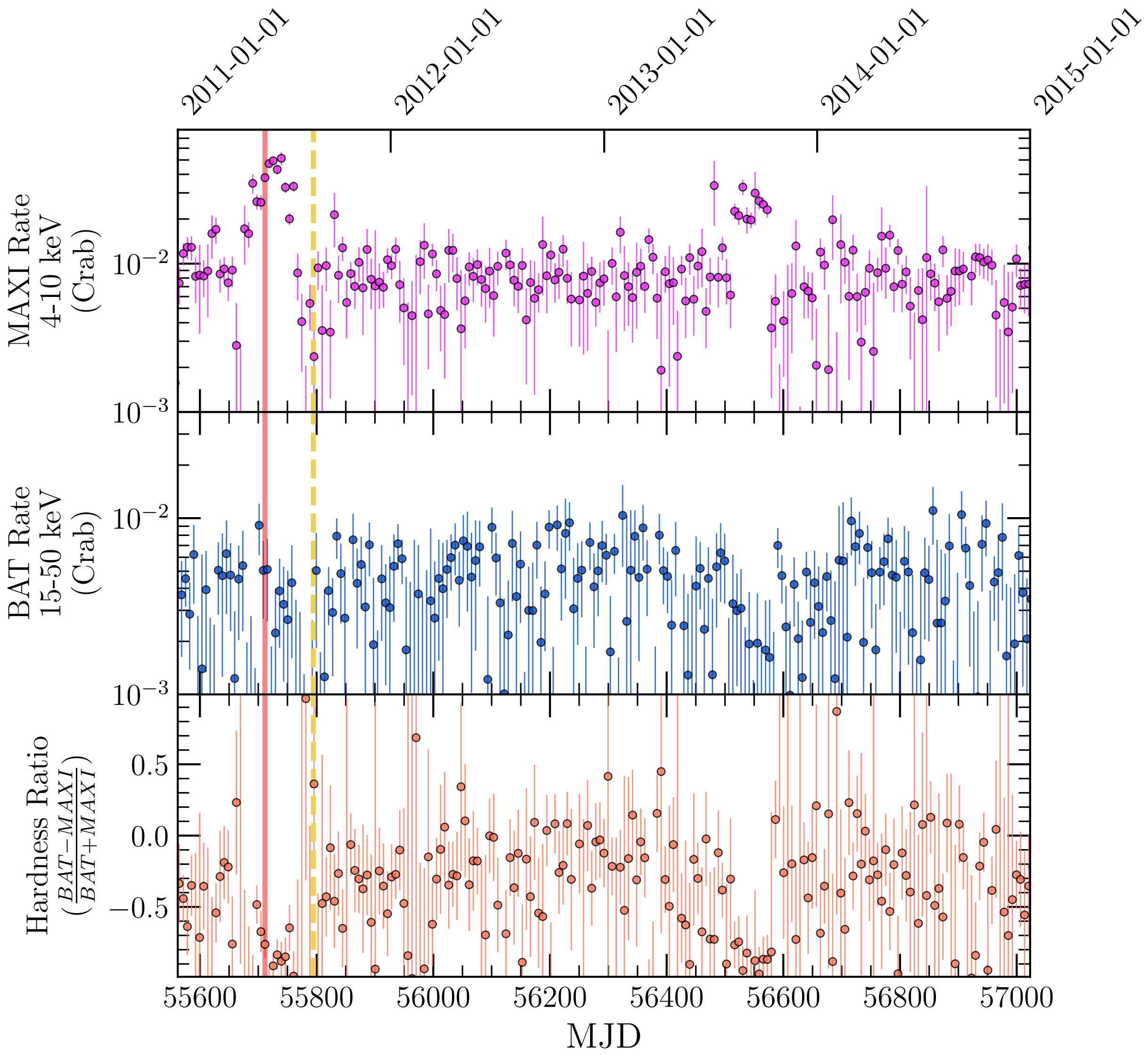

Figure 2.6: 2011–2014 X-ray light curve of M15 (including flux from both AC 211 and M15 X-2) from MAXI (4–10 keV; top) and Swift/BAT (15–50 keV; middle), with hardness ratio in the bottom panel. The 2011 and 2013 flaring events are evidence. The epoch of our simultaneous 2011 May 30 VLA and Swift/XRT data is marked with a thick vertical salmon line. For reference, the second grouping of VLA data (2011 Aug 21/22) is marked with a dashed vertical yellow line; there are no simultaneous Chandra data for these epochs.

Figure 3.1). Not all black holes follow this relation. Some sit on steeper relations, which could be viewed as either being "radiatively efficient" or with suppressed radio emission (e.g., Coriat et al. 2011; Ratti et al. 2012; Huang et al. 2014; Plotkin et al. 2017; Carotenuto et al. 2021; van den Eijnden et al. 2021).

| Source | Date<br>(UT) | $S_{5.0\mathrm{GHz}}$<br>($\mu$Jy) | $S_{7.4\mathrm{GHz}}$<br>($\mu$Jy) | $\alpha$ |
|---|---|---|---|---|
| AC 211 | 2011 May 22.535 (22.521–22.549) | $270.8 \pm 6.4$ | $273.8 \pm 7.5$(a) | $+0.03 \pm 0.11$ |
| | 2011 May 26.503 (26.488–26.518) | $794.2 \pm 7.9$ | $764.8 \pm 6.4$ | $-0.10 \pm 0.03$ |
| | 2011 May 30.512 (30.455–30.568) | $292.0 \pm 6.3$ | $235.5 \pm 7.3$ | $-0.55 \pm 0.10$ |
| | 2011 August 21.377 (21.291–21.383) | $295.9 \pm 5.7$ | $228.7 \pm 6.0$ | $-0.66 \pm 0.08$ |
| | 2011 August 22.438 (22.392–22.485) | $602.5 \pm 5.2$ | $458.3 \pm 4.8$ | $-0.70 \pm 0.03$ |
| M15 X-2 | 2011 May 22.535 (22.521–22.549) | $150.5 \pm 6.4$ | $203.9 \pm 7.5$(a) | $+0.90 \pm 0.17$ |
| | 2011 May 26.503 (26.488–26.518) | $63.6 \pm 7.9$ | $62.6 \pm 6.4$ | $-0.03 \pm 0.42$ |
| | 2011 May 30.512 (30.455–30.568) | $205.0 \pm 6.3$ | $203.7 \pm 7.3$ | $-0.02 \pm 0.12$ |
| | 2011 August 21.377 (21.291–21.383) | $<18.3$ | $<18.0$ | ... |
| | 2011 August 22.438 (22.392–22.485) | $<17.6$ | $<15.1$ | ... |

Table 2.4: VLA Observations of AC 211 and M15 X-2.
**Note.**
(a) Central frequency of 7.0 GHz, not 7.4 GHz.

Migliari & Fender (2006) collected the limited extant radio and X-ray measurements of neutron star X-ray binaries, suggesting that they typically produced jets, but (i) were fainter in the radio than black holes at the same $L_X$, and (ii) possibly followed a steeper radio/X-ray correlation than did black holes. Subsequent studies emerged slowly, since transient neutron star LMXBs often change states quickly and are intrinsically faint.

However, newly available facilities in the last decade have allowed for more successful X-ray and radio follow-up of neutron star LMXBs, especially in the more poorly studied regime $L_X < 10^{36}$ erg s$^{-1}$. To the extent that there is a unifying conclusion from these studies, it is that neutron star LMXBs show an enormous variety of behaviors (Tudor et al., 2017; van den Eijnden et al., 2021). While it is possible to fit a mean radio/X-ray correlation to the hard state accreting neutron stars, which appears to have a slope similar to that for black holes but with a lower normalization (Gallo et al. 2018, see also Figure 3.1), individual systems deviate from this mean relation to a much greater degree than for black holes. Some systems, such as the accreting millisecond pulsar IGR J16597–3704 and the ultracompact system 4U 1543–624, are much fainter in the radio than predicted from this mean relation

(Tetarenko et al., 2018; Ludlam et al., 2019). Others, such as the accreting millisecond pulsar IGR J17591–2342, are likely as radio-loud as accreting black holes over some range in X-ray luminosity, perhaps reaching down to $L_X \sim 4 \times 10^{35}$–$10^{36}$ erg s$^{-1}$ (Russell et al., 2018; Gusinskaia et al., 2020a). The deviations occur not only in normalization but in slope: there is good evidence that in at least in some systems, the radio emission becomes much fainter, or is quenched entirely, at $L_X < 10^{36}$ erg s$^{-1}$ (Gusinskaia et al., 2017, 2020b).

The results from this current paper, combining persistent systems with the outbursting binary GRS 1747–312, provide strong support for this picture of a broad range of behaviors for different neutron star LMXBs. Since these systems are all located in Galactic globular clusters, they also add the crucial element of known distances, which allows firm luminosity measurements that are lacking for many of the field systems.

Perhaps the only hard/island state accreting neutron star in our sample that that sits close to the mean radio/X-ray relation is the ultracompact 4U 1820–30, which does so at $L_X \sim 10^{37}$ erg s$^{-1}$ in Figure 3.1. M15 X-2 (also an ultracompact) appears to have similar radio/X-ray properties to 4U 1820–30 at this epoch, but the situation is slightly more complex, as the M15 X-2 observations may have occurred while the binary was transitioning to a softer state (Section 3.6.2).

GRS 1747–312 is a spectacular outlier. In the 2015 quasi-simultaneous radio/X-ray epoch, it is the most radio-luminous neutron star LMXB ever observed at $L_X < 10^{35}$ erg s$^{-1}$, sitting near the upper envelope of the black hole radio/X-ray correlation (Figure 3.1). In a subsequent quasi-simultaneous epoch in 2018, it has the lowest $L_X$ detection of radio emission for any "normal" neutron star LMXB (i.e., excluding the transitional millisecond pulsars), again sitting close to the black hole radio/X-ray correlation. It shows substantial radio and X-ray variability between different epochs. In a third quasi-simultaneous epoch, it is not detected in the radio, suggesting at least a factor of 15 variability in the radio at these $L_X$ of a few $\times 10^{34}$ erg s$^{-1}$. As discussed below in Section 4.2.3, the radio variability and radio spectral index do not support the idea that the radio emission in GRS 1747–312 originates in a steady compact jet, and another physical mechanism is more likely.

XB 1832–330 is a persistent X-ray source, and its deep radio upper limit at $L_X \sim 2\times10^{35}$ is among the most constraining observed at this $L_X$, comparable to that seen in Aql X-1 during its fading after an outburst (Gusinskaia et al., 2020b). As in Aql X-1, the XB 1832–330 data are consistent either with a steep radio/X-ray correlation for this binary or with a quenching of the jet at this luminosity. X1850–087 is another system in our sample with a deep constraining radio upper limit in the hard state at a relatively high $L_X \sim 10^{36}$ erg s$^{-1}$, but these data may have been taken near the start of an outburst, making their interpretation more challenging; we defer further discussion of this system to Section 4.2.3.

As an accretion disk corona source, the radio properties of AC 211 in M15 are also not straightforward to interpret, but if it is an accreting neutron star, it is rather radio-loud compared to other systems at this $L_X$. One potential explanation, discussed in Section 3.6.1, is that its luminosity is actually near the Eddington limit and its radio/X-ray properties are akin to Z sources such as Sco X-1. Another, less likely possibility is that AC 211 instead contains a black hole, but this is both a priori unlikely and difficult to prove.

A number of recent papers have tried to determine whether there is a simple explanation for the wide variation in radio properties of neutron stars, but have found that the most likely potential explanations, such as the spin rate or magnetic field of the neutron star, cannot readily account for the observed differences (Migliari et al., 2011; Tetarenko et al., 2018; Tudor et al., 2017; van den Eijnden et al., 2021). These globular cluster neutron star LMXBs stress this point even further by widening the range of observed behaviors. All of the

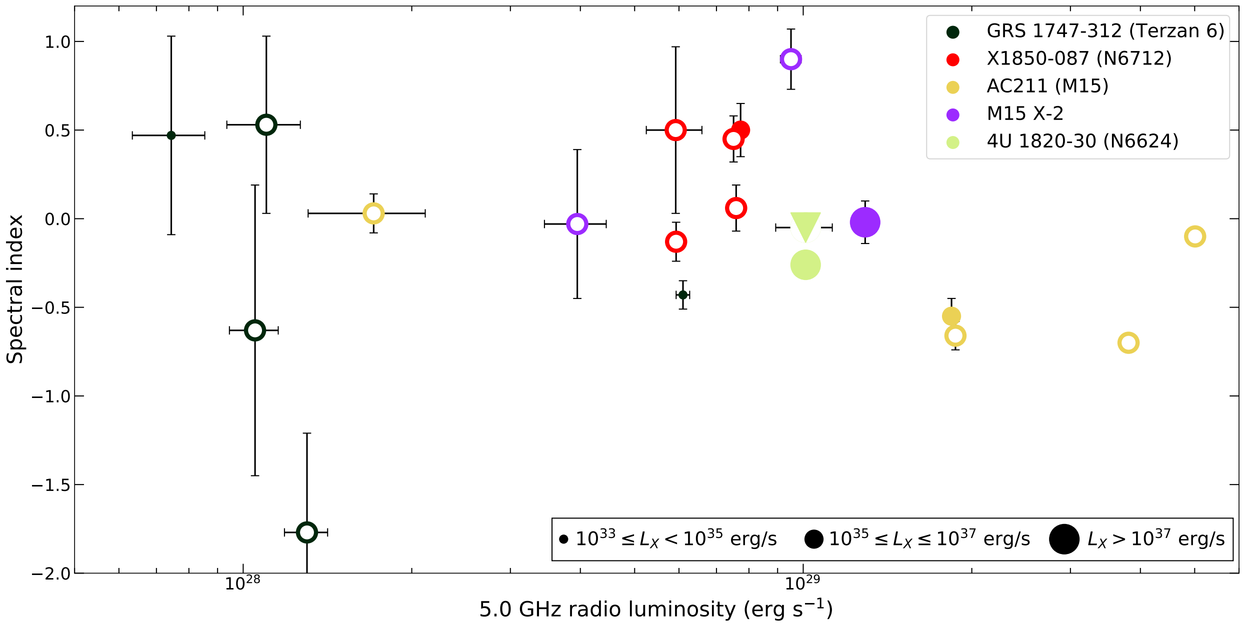

Figure 2.7: The relationship between radio spectral index and radio luminosity at 5.0 GHz. Filled markers have an associated quasi-simultaneous X-ray observation, while unfilled markers do not. The size of the marker indicates an estimate of the X-ray luminosity: small points $10^{33} \leq L_X \leq 10^{35}$ erg s$^{-1}$ , medium points $10^{35} \leq L_X \leq 10^{37}$ erg s$^{-1}$, and the largest points $L_X > 10^{37}$ erg s$^{-1}$. The upside down triangle represents a spectral index upper limit for one epoch of 4U 1820–30. Steady compact jets are expected to consistently show flat to mildly inverted spectral indices $(0\alpha + 0.5)$. Strongly inverted spectral indices $(\alpha > +0.5)$ reflect more optically thick synchrotron emission, while more negative spectral indices (typically $-0.8 < \alpha < -0.4$) represent partially or entirely optically thin synchrotron. As discussed in the text, there may be a weak trend for more negative spectral index at the highest radio luminosity, but this is primarily driven by AC 211.

hard state radio/X-ray measurements here are for “normal” persistent or transient neutron stars; none of these systems are known to be accreting millisecond X-ray pulsars, which are suspected (but not proven) to have higher magnetic fields than other neutron star LMXBs (Patruno & Watts, 2021). Hence these data are consistent with the idea that magnetic field strength is not the primary determinant of radio-loudness for accreting neutron stars.

### 2.4.2 Spectral Indices

The radio emission of neutron star LMXBs is thought to be non-thermal synchrotron radiation. Over some range of frequencies, synchrotron radiation is expected to emit as a power law, with $S_\nu \propto \nu^\alpha$.

The expected value of the spectral index depends on the origin of the synchrotron emission. Within the jet paradigm, flat ($\alpha \sim 0$) to inverted ($\alpha 0$) spectra are generally associated with an optically thick, steady, compact jet in the low/hard X-ray state (Blandford & Königl, 1979; Fender & Kuulkers, 2001). Steeper ($\alpha 0$) spectra suggest less optically thick emission, with $\alpha \sim -0.4$ to –0.8 expected for optically thin synchrotron, as might arise from the ejection of discrete jet blobs during hard to soft X-ray state transitions often observed in black hole LMXBs (e.g., Miller-Jones et al. 2012).

Only a handful of neutron star LMXBs have published high-quality estimates of the radio spectral index in the low/hard state, typically at $L_X < 10^{36}$ erg s$^{-1}$. These are mostly consistent with the flat to inverted spectral index expected for an optically-thick compact jet (Migliari et al., 2010; Miller-Jones et al., 2010; Tetarenko et al., 2016; Gusinskaia et al., 2017; van den Eijnden et al., 2018b). Possible exceptions are SAX J1808.4–3658, which had a mildly negative mean spectral index ($\alpha = -0.24 \pm 0.10$) at $L_X \sim 10^{36}$ erg s$^{-1}$ during its 2015 outburst (Tudor et al., 2017), and IGR J17591–2342, which showed marginal evidence for evolution from a flat/inverted to slightly negative spectral index over the course of an outburst, declining from $L_X \sim 2 \times 10^{36}$ to $\sim 4 \times 10^{35}$ erg s$^{-1}$ (Gusinskaia et al., 2020a). For the four IGR J17591–2342 radio measurements during the fading part of the outburst, the mean spectral index was $\alpha = -0.35 \pm 0.11$, compared to a mean spectral index of $\alpha = +0.17 \pm 0.09$ for the three radio measurements during the initial radio-bright stage of the outburst.

In this paper we have presented spectral index measurements for five globular cluster binaries, most with multiple measurements, representing a substantial increase in neutron star LMXBs with well-measured radio spectral indices.

#### 2.4.2.1 4U1820–30 and M15 X-2

For the 2015 ATCA observation of 4U 1820–30 we find $\alpha = -0.26 \pm 0.05$ in the hard state at $L_X \sim 10^{37}$ erg s$^{-1}$. This well-measured spectral index has a slightly steep value, which could suggest it is partially optically thin at these frequencies. In addition, the 5.0 GHz radio flux density is essentially identical to that observed with ATCA in 2014 when 4U1820–30 was in a brighter ($L_X \sim 8 \times 10^{37}$ erg s$^{-1}$) soft state (Díaz Trigo et al., 2017). We note that when the present paper was close to submission, a new paper appeared with a comprehensive analysis of new and archival radio continuum and X-ray observations of 4U 1820–30 (Russell et al., 2021). Their results are consistent with, but more extensive than, the spectral index analysis in our paper, and suggest a transition from flat-spectrum steady compact jet emission in the low (island) state to steeper, possibly transient emission from jet ejecta in the high (banana) state.

The radio spectral index measurements for M15 X-2 all come from its X-ray brightening event in May 2011. While we do not have X-ray spectral information for the first radio epoch, the radio continuum measurements are consistent with the likely initial presence of a discrete optically thick synchrotron blob ($\alpha = +0.90 \pm 0.17$) which then fades before recovering in radio luminosity to a flat spectrum ($\alpha = -0.02 \pm 0.12$) consistent with a compact jet at $L_X \sim 10^{37}$ erg s$^{-1}$. As discussed in Section 3.6.2, at this latter epoch the system is consistent either being in a hard state or in a transition from a hard state to a soft state on the rise to the peak of the brightening event. We cannot definitively decide between these possibilities with these data: there is no evidence for the jet being quenched in the May 30 VLA observation. Overall, in May 2011 M15 X-2 shows "classic" radio behavior for LMXB in the initial stages of an X-ray flare/outburst.

#### 2.4.2.2 AC 211: A Candidate Z Source

The spectral index data for AC 211 are from the same dataset as M15 X-2. However, the AC 211 data not well-explained by a standard hard/island state accreting neutron star model. In the first two observations (2011 May 22 and 26) the source shows a flat spectral index, consistent with a jet, while its radio luminosity increased by a factor of $\sim 3$ between the first and second epochs. On 2011 May 30 (four days later), a steeper spectrum is observed ($\alpha = -0.55 \pm 0.10$) despite little change in the 5.0 GHz flux density. The next radio data available are three months later, on 2011 August 21, with both the spectrum and flux matching the previous epoch. But only one day later (2011 August 22) the 5.0 GHz flux doubles while the spectrum remains steep. To summarize, AC 211 shows substantial variation in both its radio luminosity and spectral index, but with no clear correlation between these.

Previously published observations of AC 211 also show evidence for variability. A pre-upgrade VLA image of M15 found a 1.4 GHz source with a flux density of $\sim 1.8$ mJy at a position consistent with AC 211 (Kulkarni et al., 1990); this measurement is roughly consistent with the brightest 5.0 GHz flux density we see, assuming an $\alpha = -0.7$ spectral index. However, very long baseline imaging finds a typical flux density of around 200 $\mu$Jy at 1.6 GHz (Kirsten et al., 2014), which would be more consistent with a flat spectral index and a fainter overall flux level. An interpretation of AC 211 as a Z source accreting at close to the Eddington limit would give a straightforward explanation for the variability in the radio flux density and spectral index as due to discrete cases of jet ejection events (e.g., Hjellming et al. 1990; Fomalont et al. 2001). This interpretation appears to offer a more plausible explanation for the high radio luminosity of AC 211 than the speculative idea that the primary is a black hole.

#### 2.4.2.3 The Weirdos: X1850–087 and GRS 1747–312

For X1850–087 the interpretation of its spectral indices are mixed together with our interpretation of its fast radio variability, which is somewhat confusing (Section 3.2). The strongly inverted to flat spectral indices observed from 2014 May 5–9 appear to coincide with an X-ray flare, so can be explained as transient optically thick synchrotron emission. However, the source is undetected in the radio on 2014 May 13 before becoming bright again, with a flat to inverted spectral index, on May 18–20. Since the system was not detected in the radio in an apparently normal hard state ($L_X \sim 10^{36}$ erg s$^{-1}$) on 2014 April 5, one possibility is that this system has no jet in the hard state at this $L_X$, and that it transitioned to the hard (or intermediate hard) state by May 13, before undergoing a fast reflare by May 18 associated with partially optically thick synchrotron emission. This scenario is not generally consistent with previous observations of X1850–087 in the X-ray and radio (Section 3.2) but cannot be ruled out either. The level of X-ray variability observed in X1850–087 and other persistent ultracompact LMXBs is already challenging to explain (e.g., in't Zand et al. 2007; Maccarone et al. 2010; Cartwright et al. 2013), and these new radio results are intriguing, highlighting the need for more coordinated radio and X-ray observations of this source.

The final source with spectral index measurements is GRS 1747–312. It was well-detected in many radio epochs, despite being relatively faint with $L_X \sim 7 \times 10^{33}$ to $4 \times 10^{34}$ erg s$^{-1}$. At the first (and radio-brightest) epoch in 2015, sitting at the upper edge of the black hole radio/X-ray correlation, it had $\alpha = -0.43 \pm 0.08$ in ATCA data, more consistent with optically thin synchrotron than the flat/inverted emission associated with a steady jet. In an average of the 2018 VLA detections, it was fainter, with a mean $\alpha = -0.51 \pm 0.29$, consistent with the previous ATCA epoch. However, the range of values measured in the individual epochs was enormous ($-1.77 \pm 0.56$ to $+0.53 \pm 0.50$) and consistent with an intrinsic spread in the spectral indices, though this cannot be proven with these data due to the large uncertainties on the individual measurements.

The radio spectral indices and extreme radio variability are not consistent with expectations for a steady compact jet. One possibility is that the radio emission is associated with individual luminous discrete ejecta events; in principle it might be possible to image the brightest events with very long baseline interferometry. Other explanations may also be feasible. For example, the transitional millisecond pulsar PSR J1023+0038 is radio-loud in quiescence with a variable spectral index that changes on short timescales, though it is not as radio-loud as GRS 1747–312, and typically has a flatter/inverted spectral index (Deller et al., 2015). For PSR J1023+0038, the radio emission likely comes from non-steady synchrotron bubbles created near the interface between the inner disk and the neutron star (Bogdanov et al., 2018). PSR J1023+0038 is not alone: other confirmed and candidate transitional systems show luminous radio emission in their sub-luminous disk states (Hill et al., 2011; Jaodand, 2019; Li et al., 2020). It is not clear whether the same physical mechanism powers the radio emission in all of these systems, and a more "standard" propeller mechanism, producing a radio outflow, could instead be at play in a subset of them—or in GRS 1747–312.

#### 2.4.2.4 Spectral Index and Radio Luminosity

In Figure 2.7, we show the spectral index of our sources as a function of their 5.0 GHz radio luminosity. More sources are plotted here than in Figure 3.1, since we do not require a simultaneous X-ray measurement to plot them here. Epochs with only radio upper limits are not plotted, since these have no spectral index measurements or constraints.

As discussed for the individual sources above, there is no clear, strong relationship between radio luminosity and spectral index for individual sources or for the sample as a whole. There may be weak evidence for a change at the highest radio luminosities: those with $L_R > 10^{29}$ erg s$^{-1}$ have a mean $\alpha = -0.39 \pm 0.02$, while those below this radio luminosity have a mean $\alpha = +0.01 \pm 0.04$. However, this result is not very robust as it is dominated by the unusual source AC 211 at high luminosities. We also do not see evidence that the relationship between radio luminosity and spectral index varies substantially as a function of broad bins of X-ray luminosity. However, this is also not straightforward to interpret, since we do not have simultaneous X-ray data (and hence proper spectral classification) for each measurement.

## 2.5 Summary

In this paper, we used X-ray and radio data to investigate the relationship between the accretion flow and jet/outflow in six persistently accreting neutron star LMXBs and two other transient sources in Galactic globular clusters. These data represent the largest sample of quasi-simultaneous radio and X-ray observations of persistently accreting neutron star LMXBs in the low/hard state. The location of these sources in the standard radio/X-ray diagram for accreting compact objects broadly follows the results from previous studies of neutron star LMXBs, but with greater extremes of luminous radio emission and constraining upper limits. From the current sample alone there is no evidence for a well-defined correlation between X-ray and radio emission for neutron star LMXBs, but instead a large scatter in properties at all observed $L_X$ values. Nearly all of the sources in our sample with multiple measurements of their radio properties show unusual variability in both their luminosity and radio spectral index. This highlights the need for additional, high-cadence simultaneous radio and X-ray observations of neutron stars, even in nominally persistent systems, to make progress in understanding jets/outflows from accreting neutron stars.

## 2.6 Acknowledgements

We acknowledge support from NSF grant AST-1308124 and NASA grants NNX16AN73G, Chandra-GO7-18032A, Chandra-GO8-19122X, and 80NSSC21K0628. TP is funded by the NSF Graduate Research Fellowship (DGE 1848739). JS acknowledges support from the Packard Foundation. COH is supported by NSERC Discovery Grant RGPIN-2016-04602. GRS is supported by NSERC Discovery Grants RGPIN-2016-06569 and RGPIN-2021-04001.

The National Radio Astronomy Observatory is a facility of the National Science Foundation operated under cooperative agreement by Associated Universities, Inc. The Australia Telescope Compact Array is part of the Australia Telescope National Facility which is funded by the Australian Government for operation as a National Facility managed by CSIRO. The scientific results reported in this article are partially based on on observations made by the Chandra X-ray Observatory. This work made use of data supplied by the UK Swift Science Data Centre at the University of Leicester. This research has made use of data and software provided by the High Energy Astrophysics Science Archive Research Center (HEASARC),

which is a service of the Astrophysics Science Division at NASA/GSFC and the High Energy Astrophysics Division of the Smithsonian Astrophysical Observatory.

*Facilities*: VLA, ATCA, Swift/XRT, Chandra

*Software*: Astropy (Astropy Collaboration et al., 2013), AIPS (Greisen, 2003), CASA (McMullin et al., 2007), CIAO (Fruscione et al., 2006), HEASOFT (NASA High Energy Astrophysics Science Archive Research Center, 2014) Matplotlib (Hunter, 2007), Miriad (Sault et al., 1995), NumPy (Harris et al., 2020), pandas (McKinney, 2010), XSPEC (Arnaud, 1996)

## 2.7 Appendix: Radio Continuum Images

In the appendix, we show our radio continuum images for each of our eight sources (Figures 2.8 and 2.9)

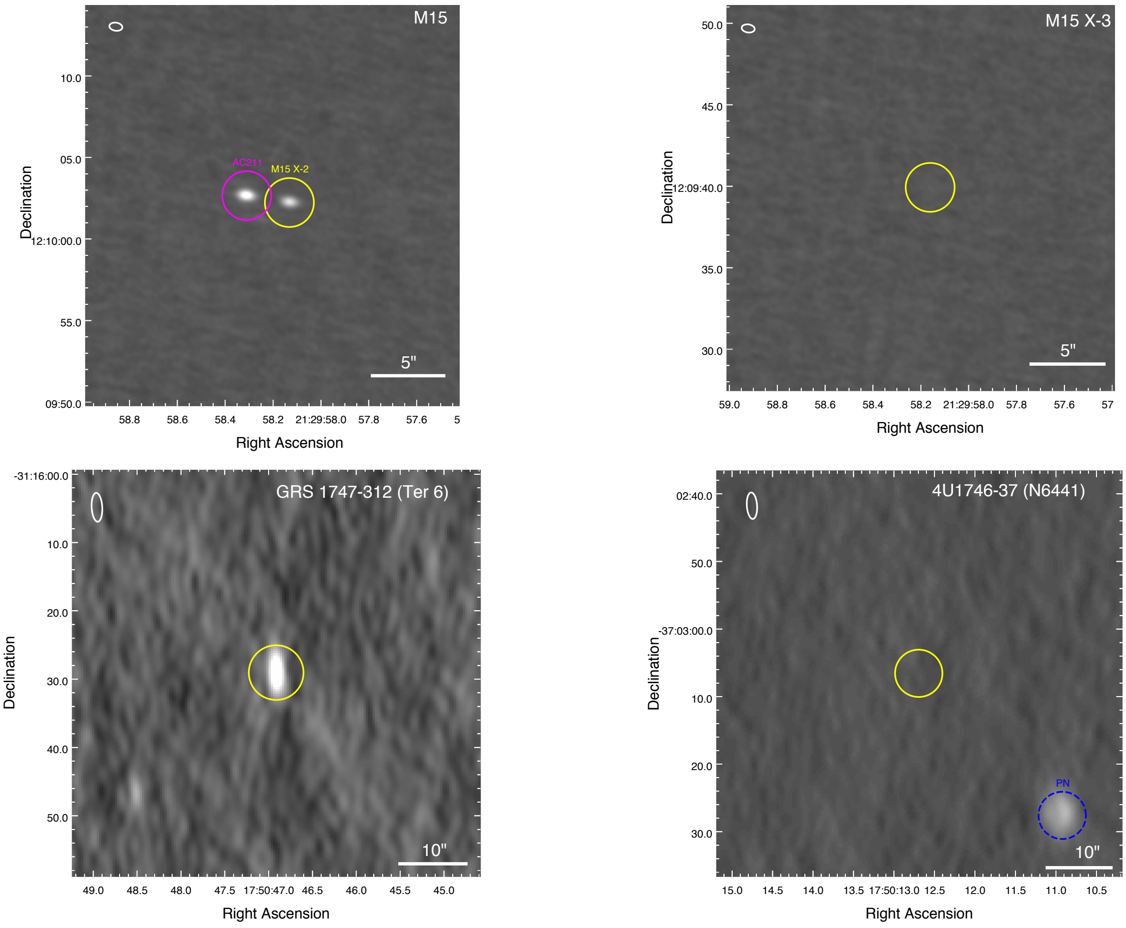

Figure 2.8: Representative radio continuum images of AC 211, M15 X-2, M15 X-3, GRS 1747–312, and 4U 1746–37. Top Left Panel: VLA 5.0 GHz image of M15 X-2 and AC 211, marked in yellow and magenta circles respectively. Top Right Panel: VLA 5.0 GHz image of the location of M15 X-3 (the source is undetected, with a $3\sigma$ upper limit of $< 16.1$ $\mu$Jy). Bottom Left Panel: ATCA 5.5 GHz image of GRS 1747–312 from 2015 April 18. Bottom Right Panel: ATCA 5.5 GHz image of the location of 4U 1746–37 (yellow); the source is undetected with a $3\sigma$ upper limit of $< 13.7$ $\mu$Jy. Here the visible source (circled in blue) is the planetary nebula JaFu 2 (Bond et al., 2020). In the top left corner of each panel, the synthesized beam is shown in white.

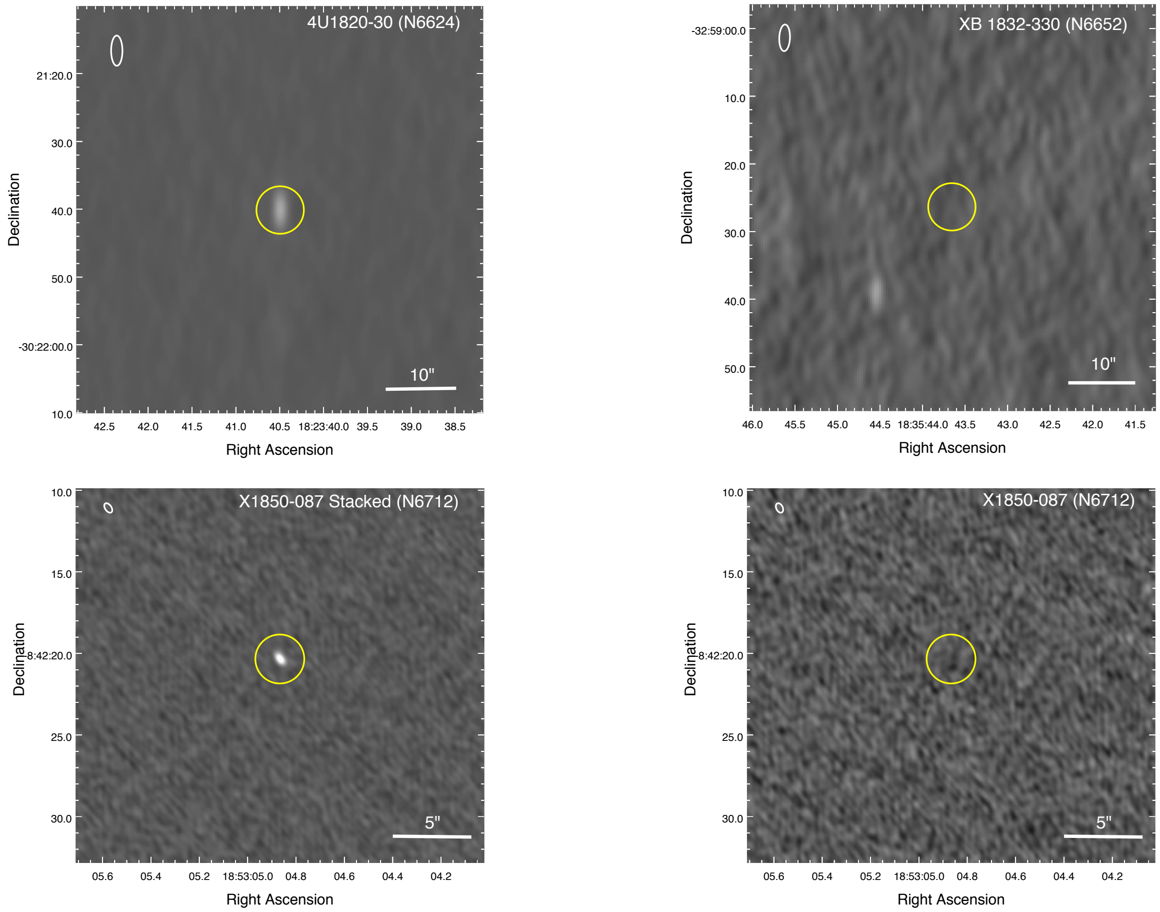

Figure 2.9: Representative radio continuum images of 4U1832–30, XB1832–330, and X1850–087. Top Left Panel: ATCA 5.5 GHz image of 4U1832–30. Top Right Panel: VLA 10 GHz image of XB1832–330. The source is undetected with a $3\sigma$ upper limit of $< 6.6$ $\mu$Jy (the faint source to the southwest is the transitional millisecond pulsar candidate NGC 6652B; Paduano et al. 2021). Bottom Left Panel: VLA 5.0 GHz May 2014 stacked image of X1850–087, with the source well-detected. Bottom Right Panel: VLA 5.0 GHz image of X1850-087 from 2014 April 5. The source is undetected with a $3\sigma$ upper limit of $< 12.9$ $\mu$Jy. Synthesized beams are shown in white at the top left corner in every image.

# Chapter 3

# Tacking the Enigmatic Globular Cluster Ultracompact X-ray Binary X1850–087: Extreme Radio Variability in the Hard State

*"Teresa please sssshhhhhhhh."* —LBC

## 3.1 Introduction

Due to their high stellar densities, globular clusters are known to host an abundant population of dynamically-formed low-mass X-ray binaries (Clark, 1975; Katz, 1975; Ivanova et al., 2007). This is especially true for ultracompact X-ray binaries—a special class of low-mass X-ray binaries with $< 1$ hr orbital periods that have hydrogen-poor donors (typically white dwarfs; Nelson et al. 1986). Of the ten Galactic systems generally accepted as persistently accreting ultracompact X-ray binaries, four are in globular clusters (Seward et al., 1976; Stella et al., 1987; Heinke et al., 2001; Zurek et al., 2009). All of these cluster ultracompact binaries have very short orbital periods in the range $\sim$ 11–21 min and neutron star primaries (Heinke et al., 2013).

Ultracompact X-ray binaries can form via standard common envelope evolutionary channels (see the review of Nelemans & Jonker 2010) or, in clusters, via direct collisions between neutron stars and red giants (Ivanova et al., 2005). Neutron star ultracompact X-ray binaries are of special interest, as their accretion physics is expected to be relatively simple compared to the bulk of low-mass X-ray binaries. After formation, their evolution is primarily driven by gravitational wave emission rather than complex stellar physics (Suvorov, 2021; Chen et al., 2021). Ultracompact binaries with periods 25 min are expected to have high enough accretion rates to keep the disk fully ionized at essentially all times and hence in a state of persistently high luminosity, $L_X \sim 10^{36}$ erg s$^{-1}$. All of the globular cluster-hosted ultracompact X-ray binaries meet this orbital period criterion and show satisfying agreement between the mean predicted and observed mass transfer rates (Heinke et al., 2013). However, they also show both short and long-term variations in their X-ray luminosities that are not well understood (Šimon, 2003; Maccarone et al., 2010).

X1850–087 in NGC 6712 is one of the four persistent ultracompact neutron star X-ray binaries in globular clusters (Seward et al., 1976), with a suspected 20.6-min orbital period (Homer et al., 1996). As part of the MAVERIC radio continuum survey of Galactic globular clusters (Tremou et al., 2018; Shishkovsky et al., 2020; Tudor et al., 2022), X1850–087 was observed over seven epochs, each of 1–2 hour duration, in April and May 2014 (Panurach et al., 2021). In these data an unusual degree of radio variability was observed, with a mixture of stringent upper limits ($< 12 - 15$ $\mu$Jy at 5.0 and 7.4 GHz) and relatively bright detections ($\sim 130 - 200$ $\mu$Jy at the same frequencies). This variability was difficult to interpret owing to the lack of simultaneous X-ray data for most of the radio epochs, other than MAXI and Swift/BAT data that require coarse time binning to detect X1850–087. There was some evidence that X1850–087 brightened in the X-rays (by a factor of $\sim 2$) and became somewhat softer during the timespan of the radio observations, but this does not fully explain the radio variability on timescales of a few days.

Panurach et al. (2021) also analyzed archival VLA observations of X1850–087 from 1989 to 1998, finding radio continuum detections comparably luminous to those in 2014 in two of the three archival epochs. Again there are no simultaneous X-ray data for these older observations. But given that the long-term X-ray light curve of the source from RXTE shows that it is only in an obvious bright state ($L_X 2 - 3 \times 10^{36}$ erg $\mathrm{s}^{-1}$) for $6 - 15\%$ of the time, it would be unlikely to have taken several additional independent radio observations during this uncommon X-ray bright/flaring state. Instead, it suggested that unexpectedly luminous radio continuum emission might be characteristic of X1850–087 at its typical X-ray luminosity of $L_X \sim 10^{36}$ erg $\mathrm{s}^{-1}$.

Since it was clear that a lack of simultaneous or quasi-simultanous X-ray data marred one's ability to interpret the existing radio observations, we undertook a monitoring campaign of X1850-087 that included both radio and X-ray observations, lasting from Feb to June 2022. This paper describes and interprets the results of this campaign.

## 3.2 Data

### 3.2.1 Radio Observations

We obtained new Very Large Array (VLA) observations of X1850-087 over six well-spaced epochs from 2022 February to July as part of NRAO program VLA/22A-111. All observations were made in the most extended A configuration using C band receivers (4.0–8.0 GHz), split into two 2.0 GHz wide subbands centered at 5.0 and 7.0 GHz. We used 3C286 or 3C48 as the flux calibrator and J1832–1035 as the complex gain calibrator for each 30-min observing block.

The data were flagged and calibrated using the standard reduction pipeline in CASA ver.5.6.2 (McMullin et al., 2007) and imaged using CASA's `tclean` feature using the Briggs weighting scheme of robustness 1.

Radio flux density measurements were made using CASA's `imfit` task by fitting a point source model matching the synthesized beam. If the source was not detected at a given epoch and central frequency, we report upper limits at the $3\sigma$ level, where $\sigma$ is defined as the local rms noise. Details of the radio observations and the measured flux densities or upper limits are listed in Table **??**.

### 3.2.2 X-ray Observations

In conjunction with our radio monitoring of X1850-087, we also obtained quasi-simultaneous X-ray data with *Swift*/XRT, with the interval between the radio and X-ray observations ranging from $\sim$ 5 hr to $\sim$ 2 d (see Table **??**). Owing to the high X-ray flux of X1850-087, all *Swift*/XRT observations were made in windowed timing mode. All observations were analyzed using software within the FTOOLS[1] package (Blackburn, 1995). The XRT data were reprocessed using the `xrtpipeline` task. Following standard procedures, light curves and spectra were extracted with `xselect`. Due to a 5 ksec gap in the 2022 May 20 observation, we split it into two different datasets and analyzed them independently. All spectra were grouped to have at least 15 counts per bin so that Gaussian statistics could be used. Spectral fitting was performed using XSPEC version 12.11.1 (Arnaud, 1996).

---

[1] http://heasarc.gsfc.nasa.gov/ftools

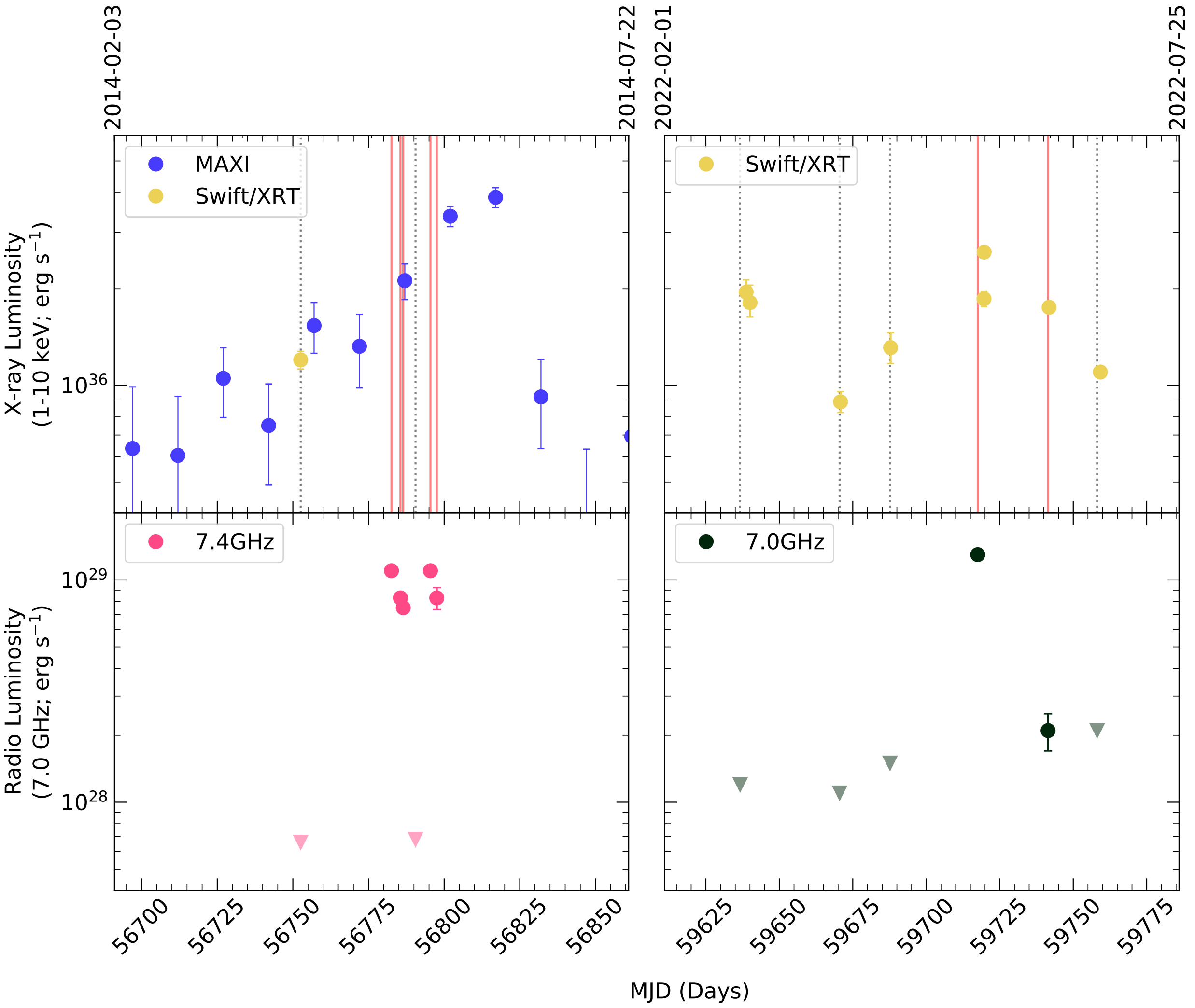

Figure 3.1: 2014 (left panel) and 2022 (right panel) radio and X-ray lightcurves for X1850–087 (see also Panurach et al. 2021). Top row shows X-ray lightcurves from MAXI (blue) and Swift/*XRT* (yellow), all plotted as 1–10keV luminosities. Bottom row shows 7.4 (left in pink; from 2014) and 7.0 GHz (right in black; from 2022) VLA radio luminosity lightcurves. Filled circles represent detections while upside down triangles are $3\sigma$ upper limits. Salmon vertical lines in the top row represents a radio detection while gray dotted lines represented a non-detection.

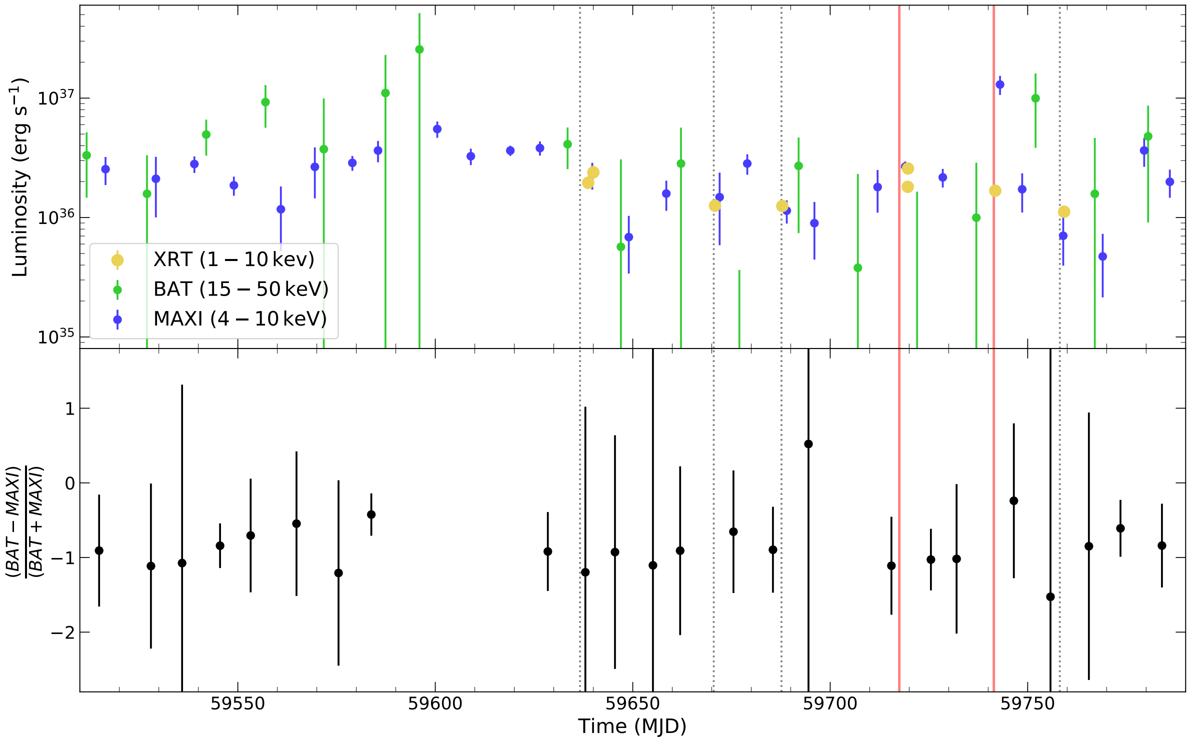

Figure 3.2: Top: X-ray light curves for MAXI (4-10 keV; blue) and *Swift*/BAT (15-50 keV; green) for times surrounding our 2022 VLA data. MAXI data points are binned to 10 days while BAT data are binned to 15 days. Also plotted are the Swift/XRT measurements (1–10 keV; yellow). Dashed vertical grey lines indicate non-detections in our simultaneous VLA observations; the solid vertical red line represents radio detections. Bottom: Hardness ratio light curve for data in top panel.

## 3.3 Results

### 3.3.1 Radio

In the first three observations (2022 Feburary 26, 2022 April 01, and 2022 April 18), X1850-087 was undetected at both 5.0 and 7.0 GHz, with typical $3\sigma$ upper limits in the range 20–30 $\mu$Jy. In the fourth observation, obtained on 2022 May 18, the source was well-detected, with 5.0 and 7.0 GHz flux densities of $212 \pm 9$ and $226 \pm 9\mu$Jy, respectively. For a power-law $S_\nu \propto \nu^\alpha$ with flux density $S_\nu$ at frequency $\nu$, these measurements give a flat to slightly-inverted spectral index of $\alpha = 0.19 \pm 0.17$.

In the next epoch, on 2022 June 11 (24 days later), the source was still detected at 7.0 GHz ($39 \pm 9\mu$Jy), but was about a factor of 6 fainter than on May 18. It was undetected at 5.0 GHz ($3\sigma$ upper limit of $< 32\mu$Jy). Finally, in the last epoch on 2022 June 28, it was not detected in either frequency ($< 40.5$ and $< 39.6\mu$Jy at 5.0 and 7.0 GHz).

For the four epochs without a detection at either frequency, we averaged the subbands together to lower the noise, but still did not detect the source at any of these epochs.

### 3.3.2 X-ray

The source is well-detected with *Swift*/XRT in all of the X-ray epochs. As a starting model, we initially fit each of the observations with a single-component absorbed blackbody disk model with both local and Galactic absorption ($TBabs \times TBabs \times diskbb$). This provided a poor fit across all epochs.

The fits are greatly improved by instead using an absorbed power-law model ($TBabs \times TBabs \times powerlaw$). While the power-law models provide suitable fits, some epochs show minor soft residuals, which we fit with an additional low temperature *diskbb* component. A summary of our spectral results is given in Table **??**. The two-component model (*diskbb+powerlaw*) is only used in observations where the addition of the *diskbb* is statistically significant ($\geq 99\%$ confidence level) relative to the single-component powerlaw model. The power-law component dominates the thermal component in all cases, implying that X1850–087 was always in a hard state during these observations.

We find small but statistically significant variations in the $N_H$ intrinsic to the source in the X-ray spectral fits. Given that previous high signal-to-noise X-ray observations have also found evidence for $N_H$ variations in X1850–087, where they are mooted to arise from a variable disk wind (Sidoli et al., 2005), we think these inferred $N_H$ variations are likely to be real, though as expected the precise value depends on the spectral model fit.

## 3.4 Discussion

### 3.4.1 Emission at Baseline in X1850-087

One of the outstanding questions posed by existing radio observations of X1850-087 is whether the source shows radio emission during its normal persistent hard state at $L_X \sim 10^{36}$ erg s$^{-1}$ (1–10 keV). In April 2014, it was undetected in deep VLA radio continuum observations at this luminosity.

Our new VLA and quasi-simultaneous *Swift* data provide suggestive (but not yet conclusive) evidence that X1850–087 does not have a persistent compact radio jet at its baseline X-ray luminosity. In three of the six new epochs, the source is around $L_X \sim 10^{36}$ erg s$^{-1}$, and there is no detectable radio emission, as was the case for the VLA data taken at a similar $L_X$ in April 2014 (radio upper limit $< 12.9\mu$Jy at 5.0 GHz). An archival VLA non-detection from 1998 provides only a weak radio upper limit ($< 135\mu$Jy at 4.9 GHz), while quasi-simultaneous X-ray data from the Rossi X-ray Timing Explorer show the X-ray luminosity appears close to the mean baseline level at this epoch.

Panurach et al. (2021) also presented results from two even earlier archival VLA observations (from 1989 and 1991), in which X1850–087 is clearly detected at 4.9 GHz in each ($156 \pm 24$ $\mu$Jy and $134 \pm 23$ $\mu$Jy, respectively). Unfortunately, there are no X-ray observations that are even quasi-simultaneous with these archival radio detections, so it is not possible to tell whether they occurred during periods of elevated X-ray luminosity.

While additional simultaneous X-ray and radio observations would be useful, at present there is no countervailing evidence to the statement that X1850–087 does not have a persistent compact radio jet/outflow in its baseline state.

### 3.4.2 Origin of Radio Emission: A Variable Jet?

The May 2014 VLA observations of X1850–087 showed a clear detection of luminous radio emission in five different epochs over a 15-day timespan, mixed in with a single deep radio upper limit 4 days after (and 5 days before) strong detections at a flux density $\sim 20\times$ higher than the $3\sigma$ upper limit (Figure 3.1; bottom left). Unfortunately, no targeted simultaneous X-ray data are available for these epochs, but time-binned MAXI data show evidence for an increase in the X-ray luminosity during this timespan, peaking at $\sim 4 \times 10^{36}$ erg s$^{-1}$ two weeks after the last radio observation (Figure 3.1; top left). Hence it seems generally plausible to suggest that X1850–087 can emit luminous radio emission at $L_X > 2 \times 10^{36}$ erg s$^{-1}$, with the important caveat that the radio non-detection in the midst of the 2014 detections must also be explained.

The 2022 data show a similar variability, though with some unanswered questions. X1850–087 is indeed strongly detected in the radio quasi-simultaneously with the most luminous X-ray emission observed over this timespan, at $L_X = 2.6 \times 10^{36}$ erg s$^{-1}$ in the second *Swift*/XRT observation on 2022 May 20 (Figure 3.1; right). It is still detected in the radio three weeks after this epoch, at a still-elevated X-ray luminosity of $\sim 1.6 \times 10^{36}$ erg s$^{-1}$, but at the lowest radio flux density for any detection ever made of this source: $39 \pm 9\mu$Jy at 7.0 GHz (it was not detected at 5.0 GHz). Given the evidence from 2014 for strong evolution of the radio flux density in X1850–087 over timescales as short as a few days, it seems plausible that the second, fainter detection is due to a radio jet or outflow that is causally unrelated to the bright radio emission seen three weeks previously. However, this cannot be definitively determined with these data.

In all of the 2014 and 2022 radio-detected epochs the radio spectral index is flat to inverted, consistent with partially self-absorbed optically-thick synchrotron emission as expected for a compact jet. Hence one interpretation superficially consistent with the data is that a compact jet is present in X1850–087 in the hard state only at $L_X > 2 \times 10^{36}$ erg s$^{-1}$, which corresponds to an accretion rate of $\sim 3 \times 10^{-10} M_{\odot}$ yr$^{-1}$ (scaling from the results of Heinke et al. 2013). Launching of the jet at around $L_X > 2 \times 10^{36}$ erg s$^{-1}$ could also self-consistently explain the finding in Panurach et al. (2021) that X1850–087 is detected at comparable radio luminosities in archival VLA data from 1989 and 1991. These observations were more difficult to explain in a model where the radio emission was only observable during rarer distinct periods when $L_X > 3 \times 10^{36}$ erg s$^{-1}$ rather than more common fluctuations to $L_X \sim 2 \times 10^{36}$ erg s$^{-1}$ in the normal persistent hard state.

In the jet interpretation, at lower accretion rates the jet is either not launched or is much less luminous than would be expected if the system followed any of the $L_R$–$L_X$ relations proposed for other accreting neutron stars in the hard state. For example, even assuming a relatively steep $L_R \propto L_X^{1.4}$ (Migliari & Fender, 2006), only a factor of 2.5–3.5 radio variability would be expected for X1850–087 in our data, rather than the factor of 20 observed. Hence, in this interpretation a quenching of the jet at *low luminosity* would be favored.

An alternative explanation is that X1850–087 is emitting discrete transient synchrotron blobs, perhaps connected with minor variations in its spectral state or luminosity. While this hypothesis is difficult to fully rule out, in broad strokes it is not consistent with our data. On 2022 May 18, when the source is brightest in the radio with a 7.0 GHz flux density of $226 \pm 9\mu$Jy, the spectral index is $\alpha = +0.19 \pm 0.17$, suggesting partially optically thick synchrotron emission. 24 days later, even though the 7.0 GHz flux density has fallen by a factor of $\sim 6$ to $39 \pm 9\mu$Jy, the spectral index is still inverted with $\alpha 0$, as it is not detected at all in the 5.0 GHz image ($3\sigma$ upper limit $< 31.5\mu$Jy). This behavior is contrary to that expected for an expanding synchrotron blob, which would be expected to become optically thin and hence brighter at lower frequencies as it fades.

The 2014 observations are also more consistent with a compact jet than synchrotron ejecta: in 5 detected epochs, taken over 16 days, the spectral index is always flat to inverted and never optically thin. In addition, in these epochs the 7.0 GHz flux density sits in a narrow range of $\sim 150 - 200\mu$Jy, rather than the broader range that would be expected for expanding blobs.

### 3.4.3 Caveats, Comparisons, and Future Work

We have suggested a scenario that appears to explain the bulk of the observations of X1850–087: a compact jet that produces radio emission is sometimes present in the persistent hard state, but only above a threshold X-ray luminosity of $L_X > 2 \times 10^{36}$ erg s$^{-1}$.

The first caveat to this scenario is that it requires jet launching and quenching to be able to occur on timescales as short as those observed in our 2014 VLA data, 4–5 days.

Jet quenching on such timescales has been observed during hard-to-soft state transitions of neutron star low-mass X-ray binaries (e.g., Miller-Jones et al. 2010), but quenching without a clear state change as we propose for X1850–087 would likely require a different physical mechanism.

Another important uncertainty is whether an accretion rate onto the neutron star in that produces $L_X > 2 \times 10^{36}$ erg s$^{-1}$ is a sufficient condition to produce detectable radio emission from X1850–087 or whether other, perhaps stochastic factors, are also at play. The first 2022 X-ray observation in our dataset (2022 Feb 28) has an inferred $L_X = (2.0 \pm 0.2) \times 10^{36}$ erg s$^{-1}$, with a similar luminosity in X-ray data obtained 1.3 d later, but there is no radio continuum emission detected in the quasi-simultaneous VLA observations. The spectral state of X1850–087 is not too dissimilar between these epochs and those on 2022 May 20 when the system is radio-luminous: formally a thermal disk improves the X-ray spectral fit in the earlier observations and not in the latter ones, but this carries only a small fraction of the X-ray luminosity in the Swift/XRT band, and does not represent strong evidence for a spectral state change. The MAXI and Swift/BAT data also show no clear evidence for spectral variations, though they are coarsely binned in time (Figure 3.2). One possibility is simply that the threshold X-ray luminosity is slightly above $2 \times 10^{36}$ erg s$^{-1}$, such that it is met on 2022 May 20 and not on 2022 Feb 28. Nothing in the 2014 data contradicts this idea—all the radio-bright epochs appear to be associated with $L_X > 2 \times 10^{36}$ erg s$^{-1}$—but this 2014 finding relies on coarsely time-binned MAXI data.

Comparing X1850–087 to other accreting neutron star binaries, we note that similar radio variability and threshold emission behaviors have been found in some other systems, though potentially in different contexts. In Be/X-ray binary system Swift J0243.6+6124, radio emission was only detected above $L_X > 2 \times 10^{36}$ erg s$^{-1}$ (van den Eijnden et al., 2019). Since the neutron star in this binary is inferred to have an extremely high magnetic field of $B \sim 10^{13}$ G (Wilson-Hodge et al., 2018), van den Eijnden et al. (2019) suggested the threshold luminosity was due to a magnetic centrifugal barrier suppressing radio emission at lower accretion rates. While the magnetic field strength of the neutron star in X1850–087 is unknown, an old, at least partially recycled globular cluster neutron star is much more likely to have a lower magnetic field, $B < 10^{10}$ G (e.g., Revnivtsev & Mereghetti 2015), and hence a much lower threshold luminosity. This casts doubt on the relevance of this mechanism for X1850–087.

A few accreting millisecond X-ray pulsars have also shown variability and/or potentially threshold behavior in the hard state. For example, Aql X-1 has a significant number of radio and X-ray studies (Migliari & Fender, 2006; Tudose et al., 2009; Miller-Jones et al., 2010; Gusinskaia et al., 2020b) in which it shows factor of $\sim$ 4 radio variability. Aql X-1 has no radio detections in the hard state at $L_X < 10^{36}$ erg s$^{-1}$, with a range of upper limits of differing depths, along with at mixture of radio detections and upper limits in the range $L_X \sim 10^{36}$ erg s$^{-1}$ to $3 \times 10^{36}$ erg s$^{-1}$. These data could conceivably be consistent with a luminosity threshold for radio emission, but instead also with a steep radio–X-ray relation and radio variability; additional deep simultaneous X-ray and radio data are needed. Two other accreting millisecond X-ray pulsars, SAX J1808.4–3658 and IGR J00291+5934, have been detected in the radio at multiple epochs with $L_X$ between $10^{34}$ and $10^{36}$ erg s$^{-1}$. Hence, these binaries do not evince a clear threshold for radio emission, though they do show radio variability of at least a factor of a few (Tudor et al., 2017).

As potentially a more direct comparison, the ultra-compact X-ray binary 4U 0614+091 has a similar baseline X-ray luminosity and spectral shape to X1850–087, but appears to have a luminous radio jet at this luminosity, albeit with a limited number of clear radio detections (Migliari et al., 2010).

While the addition of six new quasi-simultaneous radio/X-ray epochs has offered an essential new window onto the behavior of X1850–087, none of the previous radio detections of this source had simultaneous targeted X-ray data. It is clear that additional time-intensive quasi-simultaneous radio/X-ray observations of X1850–087 are needed to better characterize the range of its behaviors and test the scenario discussed here. We also highlight the persistent source 4U 0614+091 and the frequently outbursting source Aql X-1 as neutron star binaries for which improved radio characterization in the hard state could be especially revealing.

## 3.5 Acknowledgements

JS acknowledges support from NASA grant 80NSSC21K0628 and the Packard Foundation. TP is supported by the National Science Foundation Graduate Research Fellowship under Grant No. DGE-2039655.

The National Radio Astronomy Observatory is a facility of the National Science Foundation operated under cooperative agreement by Associated Universities, Inc. We acknowledge the use of public data from the Swift data archive.

*Facilities*: VLA, *Swift*/XRT, MAXI

*Software*: Astropy (Astropy Collaboration et al., 2013), CASA (CASA Team et al., 2022), FTOOLS (Blackburn, 1995), MATPLOTLIB (Hunter, 2007), NUMPY (Harris et al., 2020), PANDAS (McKinney, 2010), XSPEC (Arnaud, 1996)

| Radio Observation Date (Midpoint UT) | 5.0GHz Flux Density ($\mu$Jy) | 7.0GHz Flux Density ($\mu$Jy) | X-Ray Date (Midpoint UT) | X-ray Flux (1 - 10 keV) ($10^{-10}$ ergs s$^{-1}$ cm$^{-2}$) |
|---|---|---|---|---|
| 2022 Feb 26 (15:49:37) | $< 30.0$ | $< 22.5$ | 2022 Feb 28 (17:13:08.09) | $2.5 \pm 0.2$ |
| | | | 2022 Mar 2 (00:48:14.12) | $2.4^{+0.3}_{-0.2}$ |
| 2022 Apr 01 (12:13:31) | $< 30.3$ | $< 21.3$ | 2022 Apr 01 (19:32:46.54) | $1.16 \pm 0.09$ |
| 2022 Apr 18 (15:48:18) | $< 32.7$ | $< 29.7$ | 2022 Apr 18 (20:40:28.68) | $1.71^{+0.19}_{-0.18}$ |
| 2022 May 18 (12:03:25) | $212 \pm 8.9$ | $226.2 \pm 8.9$ | 2022 May 20 (15:14:00.12) | $2.43 \pm 0.13$ |
| | | | 2022 May 20 (16:43:32.20) | $3.39 \pm 0.10$ |
| 2022 Jun 11 (10:27:36) | $< 31.5$ | $39.1 \pm 9.0$ | 2022 Jun 11 (18:58:43.63) | $2.28^{+0.09}_{-0.08}$ |
| 2022 Jun 28 (03:20:37) | $< 40.5$ | $< 39.6$ | 2022 Jun 29 (05:32:34.28) | $1.43 \pm 0.06$ |

Table 3.1: 2022 Radio and X-ray Observations.

| Comp | Parameter | Observation ID | | | | | | | |
|---|---|---|---|---|---|---|---|---|---|
| | | Date | | | | | | | |
| | | 15041001 | 15041002 | 15041003 | 15041004 | 15179001a | 15179001b | 15213001 | 15213001 |
| | | 2022 Feb 28 | 2022 Mar 2 | 2022 Apr 1 | 2022 Apr 18 | 2022 May 20 | 2022 May 20 | 2022 Jun 11 | 2022 Jun 29 |
| *TBabs* | $N_{\mathrm{H,\,LoS}}$ ($10^{22}$cm$^{-2}$) | [0.25] | [0.25] | [0.25] | [0.25] | [0.25] | [0.25] | [0.25] | [0.25] |
| *TBabs* | $N_{\mathrm{H,\,int}}$ ($10^{22}$cm$^{-2}$) | $< 0.02$ | $0.09 \pm 0.03$ | $0.19^{+0.09}_{-0.08}$ | $0.08 \pm 0.04$ | $0.07 \pm 0.04$ | $0.05 \pm 0.02$ | $< 0.02$ | $< 0.01$ |
| *powerlaw* | $\Gamma$ | $2.31^{+0.08}_{-0.04}$ | $2.78 \pm 0.13$ | $2.2 \pm 0.2$ | $2.2 \pm 0.1$ | $2.66^{+0.15}_{-0.14}$ | $2.55 \pm 0.08$ | $2.53 \pm 0.05$ | $2.35 \pm 0.05$ |
| | normalization | $0.078^{+0.006}_{-0.002}$ | $0.10^{+0.04}_{-0.02}$ | $0.040^{+0.009}_{-0.007}$ | $0.08 \pm 0.02$ | $0.128^{+0.017}_{-0.015}$ | $0.163^{+0.011}_{-0.010}$ | $0.074 \pm 0.010$ | $0.056 \pm 0.002$ |
| | $f^{tot}_{1-10\,\mathrm{keV}}$ ($10^{-10}$ erg s$^{-1}$ cm$^{-2}$) | $2.05 \pm 0.07$ | $2.09 \pm 0.10$ | $1.16 \pm 0.09$ | $1.40 \pm 0.06$ | $2.43 \pm 0.13$ | $3.39 \pm 0.10$ | $2.05 \pm 0.04$ | $1.43 \pm 0.06$ |
| | $L^{tot}_{1-10\,\mathrm{keV}}$ ($10^{36}$ erg s$^{-1}$) | $1.57 \pm 0.05$ | $1.60 \pm 0.07$ | $0.89 \pm 0.07$ | $1.08 \pm 0.05$ | $1.86 \pm 0.10$ | $2.60 \pm 0.08$ | $1.57 \pm 0.03$ | $1.10 \pm 0.05$ |
| | $\chi^2_{\mathrm{red}}$ (degrees of freedom) | 1.01(231) | 1.08(156) | 0.89(75) | 1.13(168) | 1.26(108) | 1.17(238) | 1.64(341) | 0.94(195) |
| *TBabs* | $N_{\mathrm{H,\,int}}$ ($10^{22}$cm$^{-2}$) | $0.37^{+0.13}_{-0.15}$ | $0.22^{+0.18}_{-0.14}$ | | $0.48^{+0.18}_{-0.19}$ | | | $0.12^{+0.06}_{-0.05}$ | |
| *powerlaw* | $\Gamma$ | $2.50 \pm 0.15$ | $2.6 \pm 0.3$ | | $2.55 \pm 0.19$ | | | $2.28 \pm 0.11$ | |
| | normalization | $0.10 \pm 0.02$ | $0.10^{+0.04}_{-0.02}$ | | $0.08 \pm 0.02$ | | | $0.074 \pm 0.010$ | |
| *diskbb* | $kT$ (keV) | $0.120^{+0.022}_{-0.014}$ | $0.16^{+0.09}_{-0.06}$ | | $0.091^{+0.014}_{-0.010}$ | | | $0.18^{+0.03}_{-0.02}$ | |
| | normalization ($10^4$) | $150^{+760}_{-130}$ | $7.0^{+148}_{-6.9}$ | | $720^{+4860}_{-650}$ | | | $2.8^{+6.8}_{-2.0}$ | |
| | $f^{powerlaw}_{1-10\,\mathrm{keV}}$ ($10^{-10}$ erg s$^{-1}$ cm$^{-2}$) | $2.29 \pm 0.15$ | $2.1^{+0.2}_{-0.3}$ | | $1.64 \pm 0.14$ | | | $2.01^{+0.09}_{-0.08}$ | |
| | $f^{diskbb}_{1-10\,\mathrm{keV}}$ ($10^{-10}$ erg s$^{-1}$ cm$^{-2}$) | $0.25^{+0.11}_{-0.09}$ | $0.30^{+0.11}_{-0.15}$ | | $0.06^{+0.07}_{-0.04}$ | | | $0.27^{+0.05}_{-0.04}$ | |
| | $f^{tot}_{1-10\,\mathrm{keV}}$ ($10^{-10}$ erg s$^{-1}$ cm$^{-2}$) | $2.5 \pm 0.2$ | $2.4^{+0.3}_{-0.2}$ | | $1.71^{+0.19}_{-0.18}$ | | | $2.28^{+0.09}_{-0.08}$ | |
| | $L^{tot}_{1-10\,\mathrm{keV}}$ ($10^{36}$ erg s$^{-1}$) | $2.0 \pm 0.2$ | $1.8 \pm 0.2$ | | $1.31^{+0.15}_{-0.14}$ | | | $1.75^{+0.07}_{-0.06}$ | |
| | $\chi^2_{\mathrm{red}}$ (degrees of freedom) | 0.90(229) | 0.94(154) | | 1.06(166) | | | 1.23(339) | |

Table 3.2: X-ray spectral properties of X1850–087.

**Note.**

The Galactic line-of-sight absorption ($N_{\mathrm{H,\,LoS}}$; values in square brackets) is fixed. All observations are initially fit with an absorbed powerlaw model. In some observations, an additional *diskbb* component significantly (confidence level $>$ 99%) improves the fit. Reported fluxes ($f_{1-10\,\mathrm{keV}}$) and luminosities ($L_{1-10\,\mathrm{keV}}$) are unabsorbed.

# Chapter 4

# The MAVERIC Survey: A Radio Imaging Catalog of Seven Galactic Globular Clusters from Karl G. Jansky Very Large Array

*"I'm going to prove to you I'm allergic to dogs - look."* —JMS

## 4.1 Introduction

In globular clusters' cores, direct encounters involving binaries occur frequently; heavier objects are retained in binaries while lighter objects are ejected (Sigurdsson & Hernquist, 1993). Because of this, theoretical models have predicted that all black holes sank towards the center and created black hole binaries (Spitzer, 1969). However, new theoretical modeling has suggested that this ejection process wasn't completely efficient, and even suggests that black holes could control the internal dynamical evolution of many clusters (Rodriguez et al., 2015). Observational work has now confirmed multiple stellar-mass black holes (and additional candidates) quietly accreting from binary companions in Galactic globular clusters (Strader et al., 2012a; Chomiuk et al., 2013; Miller-Jones et al., 2015; Shishkovsky et al., 2018; Urquhart et al., 2020; Zhao et al., 2020) through their radio continuum emission.

The MAVERIC (Milky-way ATCA/VLA Exploration of Radio-sources in Clusters) Survey is our team's large, radio continuum survey, initially proposed to use the Karl G. Jansky Very Large Array (VLA) to observe the most massive ($> 10^5 M_\odot$) and closest ($<$ 9 kpc) Galactic globular clusters to search for low-accreting stellar-mass black holes and constraining emission from intermediate-mass black holes. The survey has proved useful to study other radio-emitting compact sources in globular clusters including accreting neutron stars in LMXBs and pulsars (Tremou et al., 2018; Shishkovsky et al., 2020; Urquhart et al., 2020; Zhao et al., 2020; Panurach et al., 2021; Tudor et al., 2022). It was originally proposed to observe 35 Galactic globular clusters, however only 28/35 of the sample were completed, most of which were southernly clusters due to limited time in BnA configuration.

Our team proposed a follow-up to our original MAVERIC observations in order to complete and allow homogeneous coverage of our globular cluster sample, and was approved (PI: Shishkovsky; 18A-081) in 2018. Most clusters that were proposed are metal-rich, and doubled the number of metal-rich globular clusters in our sample. Attaining these data were necessary to see how the populations of candidate accreting black holes and other radio-emitting sources vary with metallicity and other cluster properties such as central density.

Here we present imaging for all the seven remaining clusters in the MAVERIC Survey using the VLA, as well as a sample radio source catalog for one of the clusters (NGC 6522). In section 1, we describe the radio observations and the data reduction process. In section 2, we explain our processes of cataloging sources in NGC 6522. Finally in section 3, we discuss our findings and future work in this project.

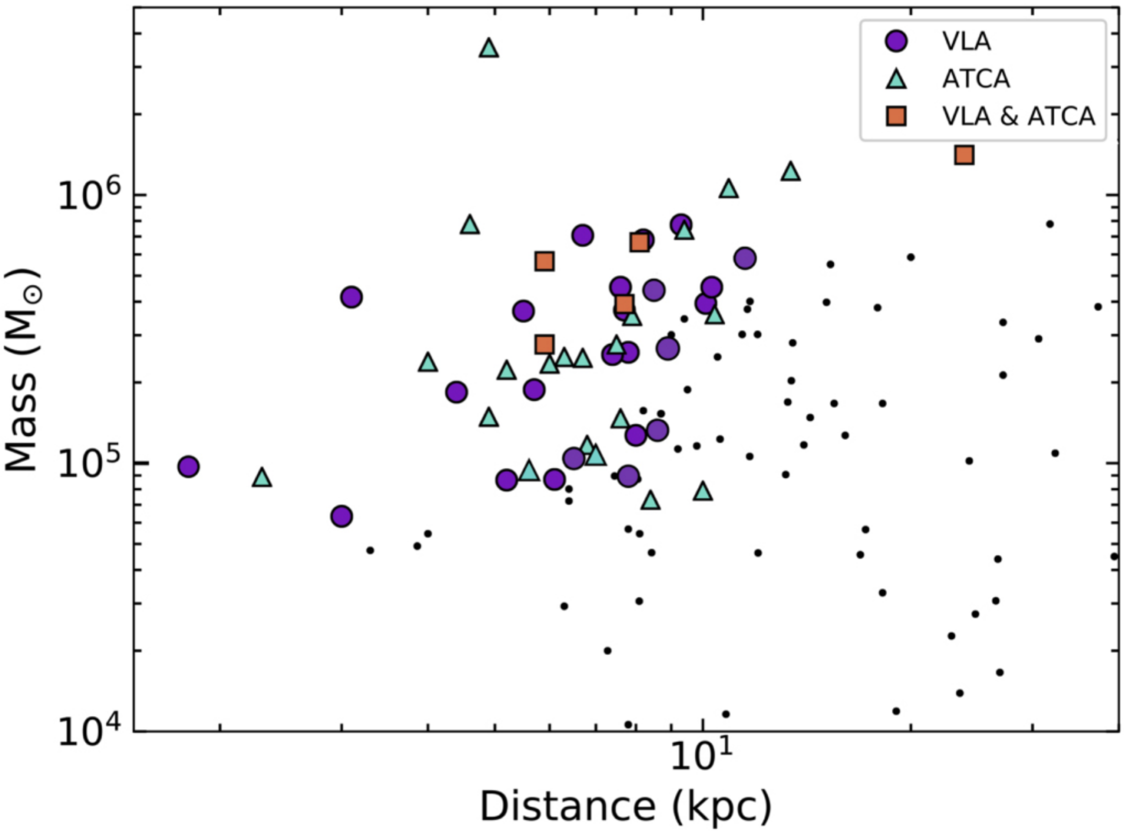

Figure 4.1: Globular cluster mass versus their distances. We show our globular cluster sample for the MAVERIC Survey, including other clusters from Baumgardt & Hilker (2018) in small black markers. Purple circles represent globular clusters taken with the VLA, green triangles represent ATCA observations, while orange squares are clusters that were observed by both. From (Shishkovsky et al., 2020).

## 4.2 Observations and Data Reduction

### 4.2.1 Observations

In 2018, we observed seven globular clusters (Djorg 2, Liller 1, NGC 6522,NGC 6553, NGC 6624, Terzan 1, and Terzan 6) with the VLA as part as the final observations for the MAVERIC Survey. For more information on previous published MAVERIC Survey datasets see Tremou et al. (2018); Shishkovsky et al. (2020) and Tudor et al. (2022). Observations were taken from 2018 March - June in A configuration with C band receivers (4.0 - 8.0 GHz), centered at 2GHz of bandwidth at 5.0 GHz and 7.0 GHz except for NGC 6624 with

X band receivers (8.0 -12.0 GHz) centered at 9.0 GHz and 11.0 GHz. NGC 6624 was observed in the X band due to a known pulsar and persistent radio-bright NS LMXB near the center of the cluster. Observing the cluster in a higher frequency allowed the pulsar to make smaller flux contribution near the center and attaining high resolution as the LMXB was ∼0.5” away from the center. Additionally, higher resolution was also useful in searching for an an intermediate-mass black hole that was previously speculated (Perera et al., 2017) which was later to not be found in our MAVERIC radio observations (Tremou et al., 2018). We primarily used the AGN 1331+305=3C286 as the flux calibrator and a phase calibrator observed in 1.5 - 2 minute intervals alternating with the target source every 5 - 20 minutes. Total observation time for the 7 clusters was 58.25 hours with variation of 1, 1.5, 2 hour for individual epochs which we list in Table **??**.

| Cluster | Date (MJD) | Observation Time (UT) |
|---|---|---|
| Djorg 2 | 2018 April 13 | 12:24:47 - 14:24:22 |
| | 2018 May 01 | 07:27:29 - 09:27:01 |
| | 2018 May 01 | 11:38:18 - 13:37:53 |
| | 2018 May 07 | 06:54:51 - 08:54:22 |
| | 2018 May 18 | 06:29:32 - 08:29:03 |
| | 2018 May 22 | 05:56:17 - 07:55:48 |
| Liller 1 | 2018 March 28 | 11:12:02 - 12:41:40 |
| | 2018 April 09 | 10:03:56 - 11:33:33 |
| N6522 | 2018 April 17 | 08:34:45 - 10:34:20 |
| | 2018 May 22 | 08:07:59 - 10:07:25 |
| | 2018 June 03 | 09:19:03 - 10:18:44 |
| | 2018 June 04 | 05:24:51 - 07:24:24 |
| N6553 | 2018 May 23 | 05:52:15 - 06:52:00 |
| | 2018 May 24 | 06:03:51 - 07:03:33 |
| | 2018 May 25 | 10:11:09 - 12:10:40 |
| | 2018 May 28 | 05:47:45 - 05:47:45 |
| | 2018 May 29 | 05:50:57 - 06:50:37 |
| | 2018 May 29 | 09:52:20 - 11:51:56 |
| | 2018 May 30 | 05:29:37 - 06:29:16 |
| | 2018 May 30 | 09:41:55 - 11:41:31 |
| N6624 | 2018 May 22 | 10:07:34 - 12:07:06 |
| | 2018 May 23 | 11:09:41 - 12:09:26 |
| | 2018 May 24 | 10:03:13 - 12:02:47 |
| | 2018 May 27 | 08:36:04 - 10:35:38 |
| | 2018 May 27 | 10:35:49 - 11:35:30 |
| | 2018 May 28 | 05:47:45 - 06:47:28 |
| | 2018 May 28 | 06:54:22 - 07:54:07 |
| | 2018 May 28 | 10:21:01 - 11:20:41 |
| Terzan 1 | 2018 March 26 | 10:10:23 - 12:28:35 |
| | 2018 March 26 | 12:28:44 - 14:46:59 |
| | 2018 March 27 | 10:34:51 - 12:53:09 |
| | 2018 April 08 | 09:24:18 - 11:42:23 |
| Terzan 6 | 2018 March 25 | 13:07:59 - 15:07:35 |
| | 2018 March 26 | 10:10:23 - 12:28:35 |
| | 2018 March 26 | 12:28:44 - 14:46:59 |
| | 2018 March 28 | 10:34:51 - 12:53:09 |
| | 2018 April 08 | 09:24:18 - 11:42:23 |
| | 2018 April 30 | 08:01:13 - 10:00:47 |
| | 2018 May 21 | 06:15:12 - 08:14:43 |
| | 2018 May 31 | 09:22:40 - 10:22:24 |
| | 2018 June 03 | 05:52:18 - 06:52:00 |

Table 4.1: Table of 18A-081 VLA Radio Observations.

| Cluster | R.A. (J2000) (h:m:s) | Dec. (J2000) (°:':") | Distance (kpc) | Core Radius (") | Half-light Radius (") | Frequency (GHz) | Image RMS (μjy) | Beam$_{Major}$ (") | Beam$_{Minor}$ (") | Beam$_{Angle}$ (degrees) |
|---|---|---|---|---|---|---|---|---|---|---|
| Djorg 2 | 18:01:49.1 | 27:49:33.0 | 7.0 | 19.8 | 63 | 4.9 | 2.3 | 0.86 | 0.44 | 17.5 |
| | | | | | | 7.0 | 2.0 | 0.63 | 0.31 | -19.34 |
| Liller 1 | 17:33:24.56 | 33:23:22.4 | 8.1 | 5.4 | 33.5 | 4.9 | 3.1 | 1.11 | 0.40 | -5.95 |
| | | | | | | 7.0 | 2.8 | 0.77 | 0.29 | -16.13 |
| N6522 | 18:03:34.89 | 30:02:03.2 | 7.7 | 3.0 | 60 | 4.9 | 2.3 | 0.93 | 0.43 | -11.16 |
| | | | | | | 7.0 | 2.0 | 0.65 | 0.31 | -13.25 |
| N6553 | 18:09:17.59 | 25:54:38.0 | 6.0 | 31.8 | 61.8 | 4.9 | 2.0 | 0.74 | 0.48 | 8.08 |
| | | | | | | 7.0 | 2.1 | 0.50 | 0.34 | 4.19 |
| N6624 | 18:23:40.51 | 30:21:39.7 | 8.4 | 3.6 | 14.0 | 8.9 | 1.8 | 0.56 | 0.23 | -16.61 |
| | | | | | | 11.0 | 1.8 | 0.45 | 0.19 | -16.17 |
| Terzan 1 | 17:35:47.20 | 30:28:54.4 | 5.2 | 2.4 | 3.82 | 4.9 | 1.8 | 0.95 | 0.42 | -5.53 |
| | | | | | | 7.0 | 1.6 | 0.65 | 0.30 | -6.09 |
| Terzan 6 | 17:50:46.85 | 31:16:29.3 | 6.8 | 3.0 | 26 | 4.9 | 2.1 | 0.87 | 0.40 | -9.34 |
| | | | | | | 7.1 | 2.2 | 0.61 | 0.29 | -8.98 |

Table 4.2: Clusters centers, distances, and core radius from Tremou et al. (2018). RMS, synthesized beam major-axis, minor axis, and angle for each cluster's subband image.

### 4.2.2 Data Reduction

When receiving our data from radio telescopes, we often obtain measurement sets that have been bombarded with radio-frequency interference (RFI), which are signals that do not come from our desired object. We also need to be sure to correct any effects from the intrument and atmosphere via calibrations. Bright calibrator sources (usually AGNs) are used to determine the solutions to the measurement set as a function of time and frequency which are then applied to the desired target.

For our MAVERIC sample, we removed any RFI and calibrated our data using the VLA's standard reduction pipeline in CASA ver.5.6.2 (CASA Team et al., 2022). The data was then imaged using CASA's `tclean` feature with Briggs weighting scheme of robustness 1 that would offer us a balance in both sensitivity and resolution, where robustness takes a value from -2.0 (close to uniform weighting) to 2.0 (close to natural weighting). We used a cell size of 0.08 and 0.06 arcsec for the 5.0 and 7.0 GHz and 0.04 and 0.03 arcsec for the 9.0 and 11.0 GHz images. Individual subband epochs were later stacked using CASA's `concat` feature which maximizes the sensitivity for each subband and then primary beam corrected using the `impbcor` function.

Self-calibration can be an iterative procedure and it is introduced in radio data reduction if the calibrators gains do not match the antennas' and reduces the image's quality. The procedure is used minimize the difference between the gains by making solutions using the measurement set itself. This is often used in fields that have particularly bright background noise. Clusters Djorg2 and the stacked subband images of NGC 6624 had bright artifacts that were later applied with additional 10 minute solution interval phase self-calibration to improve image quality.

Djorg2 was a special case in particular and had excess artifacts due to multiple bright background sources that was significantly amplified in the stacked subband images. Further phase self-calibration using 30 minute solution interval was added. While this process did not remove all trace of artifacts from the bright sources, it resulted in a satisfactory result of an RMS noise close to that theoretically expected, indicating a successful calibration process.

## 4.3 Source Finding Procedure of NGC 6522

Producing radio catalogs can be challenging feat on its own. Sources in the clusters are both point (size set by the synthesized beam) and extended sources (size set by the emission scales of the source and *uv*-coverage) and we must account for all of them. Here we show our process in creating the catalog of NGC 6522, similar process will eventually be used for all the other clusters in this program.

We use the source extraction software AEGEAN and the associated program BANE (Hancock et al., 2012; Hancock et al., 2018) to find our radio sources in NGC 6522. We searched for sources in the 5.0 and 7.0 GHz primary beam corrected stacked images. The images is first ran through BANE, which outputs an estimated background and RMS fits image that will be used to input in AEGEAN.

The algorithm searches for pixels above a given threshold value to find the sources, then grows this source using pixels above a lower threshold. For our initial search, we provided AEGEAN with a seed value of $5\sigma$ and a flood value of $3\sigma$. All found sources were visually inspected to remove artifacts or bright extended galaxies in the background. The radius of 3.7' from the cluster center was chosen as it is typical half-width half-maximum of the primary beam in the upper-frequency band (7.0 GHz). Globular clusters do extend further out and have radio sources that are outside this radius but these are rare compared to background sources. All globular cluster sources of interest are expected to be point sources. For our selection, we used CASA's `imfit` task by fitting a point source model matching the synthesized beam. The `imfit` reports a flux density and $1\sigma$ error measurement.

Spectral indices are vital for the classification of compact binaries and millisecond pulsars. Millisecond pulsars are known to be steep radio sources where they are brighter at lower frequencies while transitional millisecond pulsars are founded to be more flat but still less radio-bright than other flat-spectrum radio continuum sources like black holes at a given X-ray luminosity. Spectral indices are defined,

$$S_\nu \propto \nu^\alpha$$

where S is the measured flux density, $\nu$ is the frequency at which the observation was taken, and $\alpha$ is the spectral index. For this work we calculate each radio source by using the 5.0 GHz and 7.0 GHz flux densities. If sources were not detected in a particular subband, $3\sigma$ upper limits are used. We used the Bayesian Markov Chain Monte Carlo code, `JAGS` (Plummer, 2012) to fit the flux densities. The code also outputs their flux error measurements or $3\sigma$ upper limits. Positions, measured flux densities and spectral indices listed in Table 4.3.

### 4.3.1 Noteworthy Sources

In this catalog of NGC 6522, we find 4/38 sources within the half-light radius and most likely to associated with the cluster. Source 9 (labeled in Table 4.3) has a spectral index, $\alpha = -1.18^{+0.17}_{-0.17}$, and has no X-ray or Hubble Space Telescope (HST) F625W optical counter part. This could be an as-yet undiscovered pulsar, or a background active galactic nucleus. Source 13 is a known millisecond pulsar, PSR 18033002A (Zhang et al., 2020). We measure a steep spectral index, $-1.37^{+0.29}_{-0.30}$, which is what we expect from a pulsar. Source 27 was only detected in the 5.0 GHz subband image, therefore its spectral index is not well constrained, though it is unlikely to be a flat-spectrum source. There is no X-ray or HST F625W optical counter part, and cannot be classified with current data. Source 38 is the only source in NGC 6522's catalog that is within the cluster core and was detected only in the 7.0 GHz upperband image at 8.0$\mu$Jy. It does not have an X-ray or HST F625W optical counterpart, though a faint optical counterpart would be difficult to detect because of the crowding. Its detection at only 7.0 GHz makes identification as a pulsar unlikely, but beyond this it is hard to classify the source with current data.

## 4.4 Acknowledgements

Thank you to Ryan Urquhart and Bella Molina for helping with the data reduction process of the images and creation of the radio catalog.

The National Radio Astronomy Observatory is a facility of the National Science Foundation operated under cooperative agreement by Associated Universities, Inc.

*Facilities*: VLA

*Software*: CASA (CASA Team et al., 2022)

| # | R.A. (ICRS) (h:m:s) | $\sigma_{R.A.}$ (”) | Dec. (ICRS) (°:’:”) | $\sigma_{Dec.}$ (”) | $S_{5.0GHz}$ ($\mu$jy beam$^{-1}$) | $S_{7.0GHz}$ ($\mu$jy beam$^{-1}$) | $\alpha$ |
|---|---|---|---|---|---|---|---|
| 1 | 18:03:25.099 | 0.01 | -29:59:21.52 | 0.01 | 148.5 ± 3.4 | 102.9 ± 5.3 | $-1.10^{+0.30}_{-0.31}$ |
| 2 | 18:03:31.530 | 0.003 | -30:04:27.77 | 0.01 | 125.9 ± 2.5 | 124.1 ± 2.9 | $-0.04^{+0.08}_{-0.10}$ |
| 3 | 18:03:41.301 | 0.003 | -30:04:07.36 | 0.01 | 86.3 ± 2.5 | 93.5 ± 3.1 | $0.34^{+0.14}_{-0.13}$ |
| 4 | 18:03:24.576 | 0.01 | -30:00:28.32 | 0.01 | 84.9 ± 2.9 | 64.0 ± 3.5 | $-0.84^{+0.19}_{-0.19}$ |
| 5 | 18:03:27.910 | 0.005 | -30:03:19.87 | 0.01 | 76.7 ± 2.4 | 61.0 ± 2.4 | $-0.69^{+0.15}_{-0.15}$ |
| 6 | 18:03:23.566 | 0.01 | -30:01:57.34 | 0.01 | 63.2 ± 2.6 | 45.5 ± 3.0 | $-1.00^{+0.23}_{-0.23}$ |
| 7 | 18:03:41.235 | 0.01 | -30:01:20.73 | 0.01 | 60.1 ± 2.3 | 47.7 ± 2.3 | $-0.71^{+0.19}_{-0.20}$ |
| 8 | 18:03:28.487 | 0.01 | -30:02:17.24 | 0.01 | 57.5 ± 2.3 | 37.6 ± 2.3 | $-1.26^{+0.21}_{-0.23}$ |
| 9 | 18:03:31.415 | 0.01 | -30:01:42.83 | 0.01 | 54.7 ± 2.1 | 51.5 ± 2.1 | $-1.18^{+0.17}_{-0.17}$ |
| 10 | 18:03:19.850 | 0.03 | -30:03:41.35 | 0.07 | 48.4 ± 3.2 | < 15.4 | <-3.28 |
| 11 | 18:03:50.707 | 0.03 | -30:00:54.64 | 0.04 | 45.3 ± 3.2 | < 17.3 | <-3.21 |
| 12 | 18:03:27.522 | 0.01 | -30:00:18.81 | 0.02 | 44.1 ± 2.6 | 37.8 ± 3.1 | $-0.49^{+0.30}_{-0.31}$ |
| 13 | 18:03:35.134 | 0.01 | -30:01:59.66 | 0.02 | 39.7 ± 2.2 | 25.2 ± 2.0 | $-1.37^{+0.29}_{-0.30}$ |
| 14 | 18:03:33.316 | 0.04 | -30:05:05.00 | 0.05 | 35.1 ± 3.0 | < 11.3 | <-3.3 |
| 15 | 18:03:27.683 | 0.06 | -30:03:55.07 | 0.06 | 27.0 ± 2.5 | < 8.4 | <-3.28 |
| 16 | 18:03:27.634 | 0.01 | -30:02:46.96 | 0.02 | 26.7 ± 2.3 | 29.3 ± 2.4 | $0.27^{+0.36}_{-0.35}$ |
| 17 | 18:03:27.702 | 0.06 | -30:03:55.63 | 0.06 | 25.8 ± 2.5 | < 8.4 | <-3.26 |
| 18 | 18:03:50.739 | 0.03 | -30:01:40.08 | 0.06 | 25.5 ± 3.1 | < 14.3 | <-3.04 |
| 19 | 18:03:36.249 | 0.02 | -30:03:27.20 | 0.03 | 24.8 ± 2.2 | 14.8 ± 2.2 | $-1.59^{+0.53}_{-0.56}$ |
| 20 | 18:03:39.521 | 0.02 | -30:03:41.78 | 0.04 | 24.4 ± 2.3 | 18.7 ± 2.5 | $-0.82^{+0.48}_{-0.51}$ |
| 21 | 18:03:35.976 | 0.02 | -29:59:23.44 | 0.04 | 22.6 ± 2.8 | 20.5 ± 3.4 | $-0.37^{+0.30}_{-0.31}$ |
| 22 | 18:03:32.980 | 0.02 | -30:00:59.57 | 0.03 | 21.2 ± 2.2 | 12.4 ± 2.2 | $-1.64^{+0.59}_{-0.63}$ |
| 23 | 18:03:51.105 | 0.02 | -30:01:04.39 | 0.09 | 19.0 ± 3.2 | < 16.4 | <-2.62 |
| 24 | 18:03:36.311 | 0.10 | -29:59:59.76 | 0.07 | 18.8 ± 2.5 | < 8.7 | <-3.10 |
| 25 | 18:03:36.014 | 0.04 | -30:05:26.08 | 0.06 | 18.8 ± 3.1 | < 13.1 | <-2.8 |
| 26 | 18:03:49.061 | 0.11 | -30:00:54.09 | 0.08 | 18.2 ± 2.9 | < 13.7 | <-2.80 |
| 27 | 18:03:37.439 | 0.05 | -30:02:16.64 | 0.07 | 17.5 ± 2.2 | < 6.1 | <-3.21 |
| 28 | 18:03:28.135 | 0.02 | -30:01:43.79 | 0.03 | 17.1 ± 2.3 | 21.6 ± 2.4 | $0.71^{+0.48}_{-0.51}$ |
| 29 | 18:03:47.584 | 0.06 | -30:02:14.09 | 0.10 | 17.0 ± 2.7 | < 10.1 | <-2.93 |
| 30 | 18:03:27.587 | 0.06 | -30:03:10.41 | 0.08 | 16.9 ± 2.4 | < 7.4 | <-3.11 |
| 31 | 18:03:21.844 | 0.05 | -30:01:46.29 | 0.08 | 16.6 ± 2.7 | < 10.4 | <-2.90 |
| 32 | 18:03:32.962 | 0.04 | -30:04:10.40 | 0.07 | 15.8 ± 2.5 | < 8.2 | <-3.0 |
| 33 | 18:03:41.180 | 0.02 | -30:02:21.35 | 0.04 | 14.5 ± 2.3 | 15.7 ± 2.2 | $0.22^{+0.62}_{-0.64}$ |
| 34 | 18:03:46.046 | 0.05 | -30:00:44.06 | 0.06 | 14.2 ± 2.7 | < 10.3 | <-2.77 |
| 35 | 18:03:27.487 | 0.02 | -30:00:18.70 | 0.03 | <9.4 | 20.2. ± 3.1 | >1.08 |
| 36 | 18:03:24.115 | 0.04 | -30:02:13.83 | 0.04 | <7.4 | 17.1 ± 2.9 | >0.95 |
| 37 | 18:03:43.761 | 0.04 | -30:03:08.72 | 0.08 | <7.2 | 15.3 ± 2.7 | >0.88 |
| 38 | 18:03:35.040 | 0.02 | -30:02:05.05 | 0.06 | <6.5 | 8.0 ± 2.0 | >0.16 |

Table 4.3: NGC 6522 radio source catalog provides: the location of each source, 5.0 and 7.0 GHz flux densities or $3\sigma$ upper limit measurements, and spectral index.

## 4.5 Appendix: Stacked Radio Continuum Images of 18A-081

In the appendix, we show our the stacked radio continuum subband images for each of our clusters.

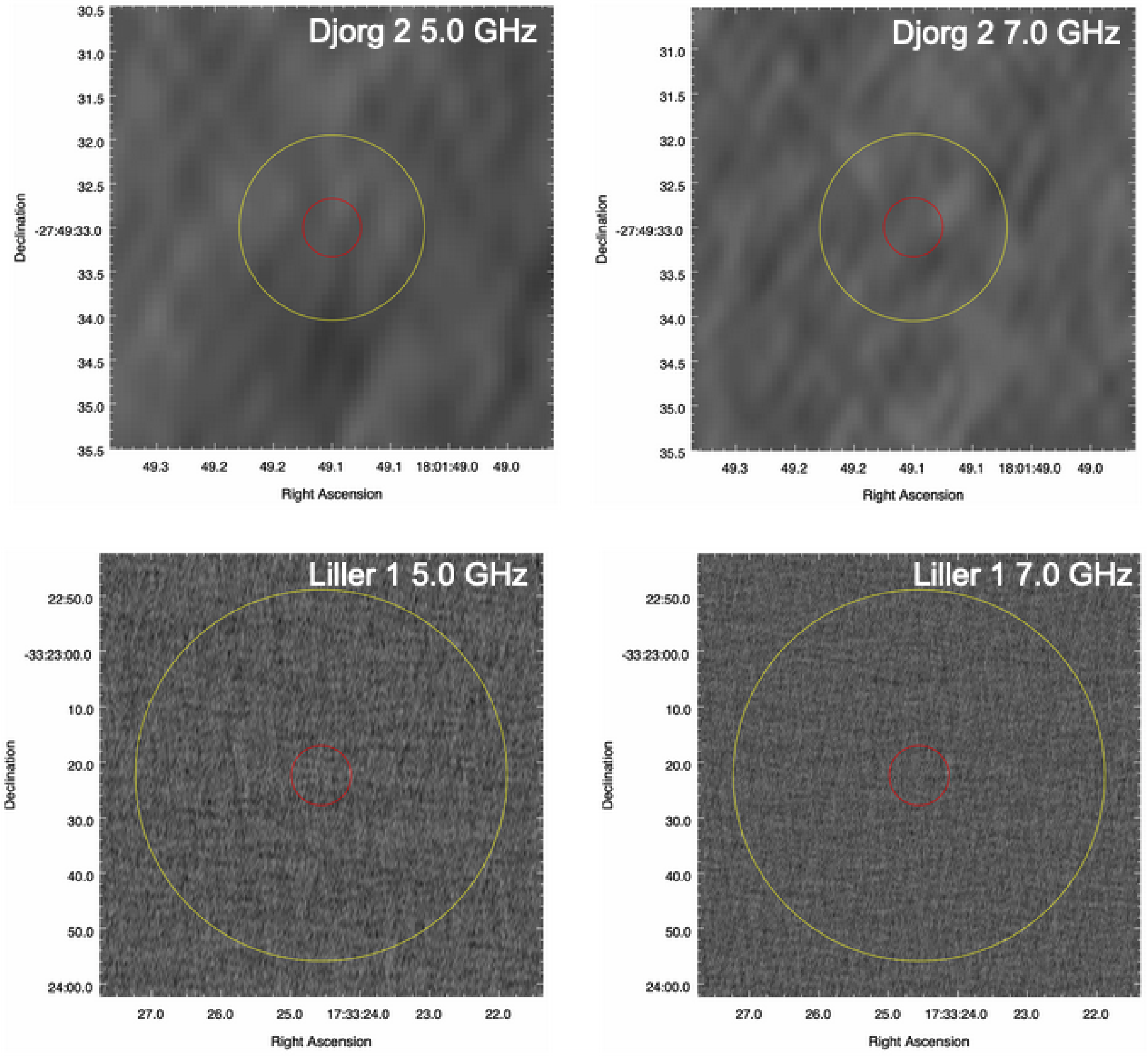

Figure 4.2: Stacked 5.0 GHz (top left) and 7.0 GHz (top right) radio continuum images of Djorg 2 and 5.0 GHz (bottom left) and 7.0 GHz (bottom right) Liller 1. Yellow circle represents each cluster's half-light radius and the red circle represents their core radius.

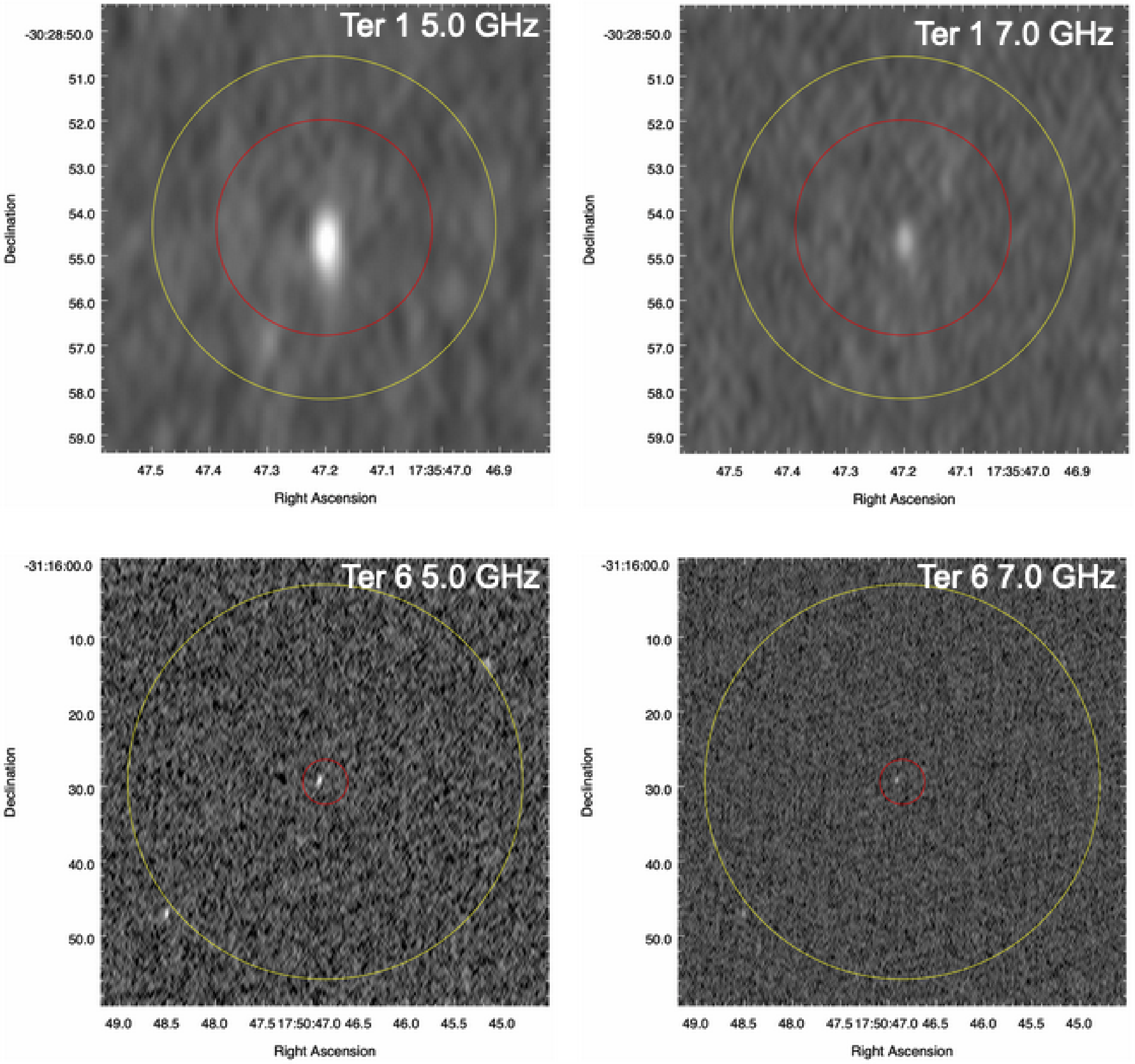

Figure 4.3: Stacked 5.0 GHz (top left) and 7.0 GHz (top right) radio continuum images of Terzan 1 and 5.0 GHz (bottom left) and 7.0 GHz (bottom right) Terzan 6. Yellow circle represents each cluster's half-light radius and the red circle represents their core radius.

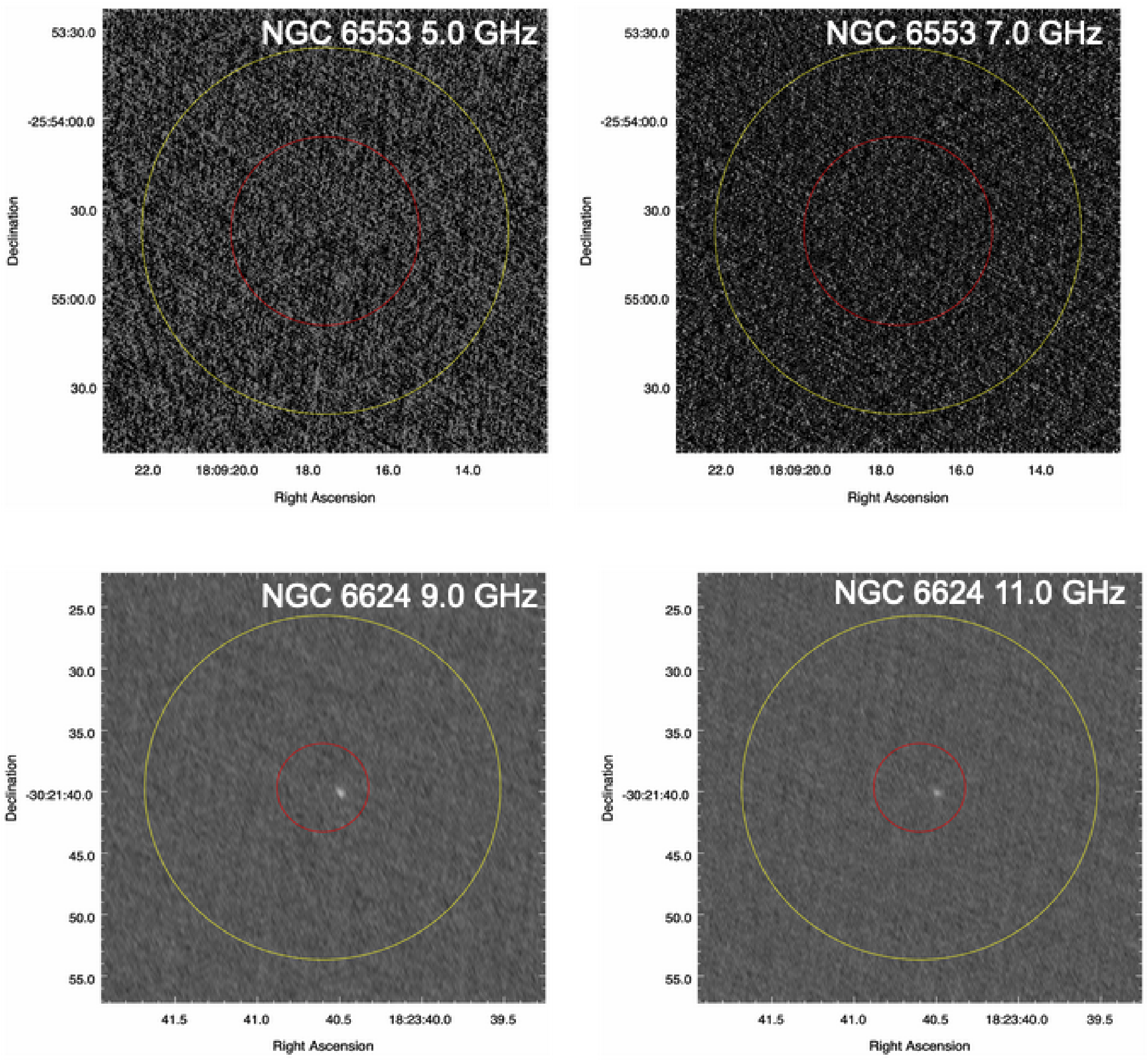

Figure 4.4: Stacked 5.0 GHz (top left) and 7.0 GHz (top right) radio continuum images of NGC 6553 and 9.0 GHz (bottom left) and 11.0 GHz (bottom right) NGC 6624. Yellow circle represents each cluster's half-light radius and the red circle represents their core radius.

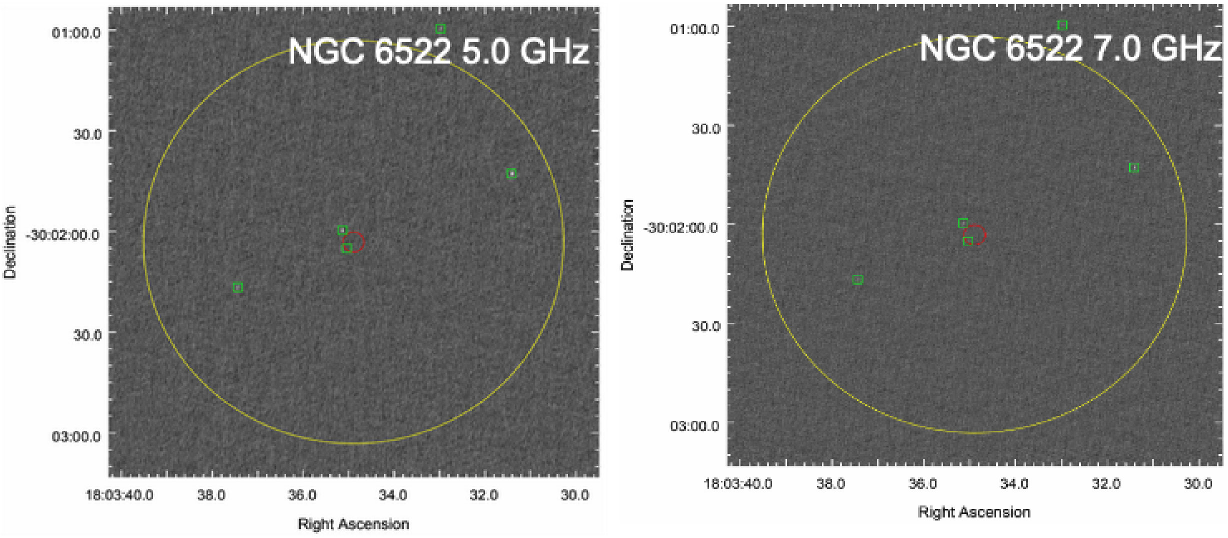

Figure 4.5: Stacked 5.0 GHz (left) and 7.0 GHz (right) radio continuum images of NGC 6522. Yellow circle represents the NGC 6522's half-light radius and red circle represents the core radius. The detected sources from our catalog are represented with the green markers.

# Chapter 5

# Conclusions

LBC: I feel like you had a really good question that you wanted to ask every one. Was it what's your fave Taylor Swift song?

JMS: I did not say that.

## 5.1 Summary

This thesis is aimed at understanding the jet–accretion coupling of accreting neutron stars in Galactic globular clusters using radio and X-ray observations from Karl G. Jansky Very Large Array, Australia Telescope Compact Array, Chandra X-ray Telescope, and *Swift*/X-ray Telescope. In this project, we have analyzed the largest sample of persistently accreting neutron stars and imaged seven globular clusters. In this final chapter, we will summarize our findings and potential future directions.

## 5.2 The MAVERIC Survey: Variable Jet–accretion Coupling in Luminous Accreting Neutron Stars in Galactic Globular Clusters

Chapter two showcases our analysis of six bright, persistently accreting neutron star X-ray binaries and two other transient sources. We used a combination of quasi/strictly-simultaneous observations of deep radio data from the VLA and ATCA telescopes and X-ray data from *Chandra* and *Swift*/XRT. We find that these neutron star X-ray binaries show an even larger range in radio luminosity than previously observed. In particular, in quiescence at $L_X \sim 3\times10^{34}$ erg s$^{-1}$, the confirmed neutron star binary GRS 1747–312 in Terzan 6 sits near the upper envelope of the black hole radio/X-ray correlation, and the persistently accreting neutron star systems AC 211 (in M15) and X1850–087 (in NGC 6712) show unusual radio variability and luminous radio emission. We interpret AC 211 as an obscured "Z source" that is accreting close to the Eddington limit, while the properties of X1850–087 are difficult to explain, and motivate future coordinated radio and X-ray observations. Overall, our results show that neutron stars do not follow a single relation between inflow and outflow, and confirm that their accretion dynamics are more complex than for black holes.

## 5.3 Tacking the Enigmatic Globular Cluster Ultracompact X-ray Binary X1850–087: Extreme Radio Variability in the Hard State

Chapter three details our radio and X-ray monitoring campaign of the persistently accreting ultracompact X-ray binary X8150–087, located in the globular cluster NGC 6712. The source has previously showcased unusual radio continuum variability in 2014 (analysis published in Panurach et al. (2021)). Using the Karl G. Janksy Very Large Array, with simultaneous or quasi-simultaneous *Swift*/X-ray Telescope data obtained at each epoch, we see the system is detected in the radio in two of the six new epochs. When combined with previous data, these results suggest that X1850–087 shows radio emission at a slightly elevated hard state X-ray luminosity of $L_X > 2 \times 10^{36}$ erg s$^{-1}$, but no radio emission in its baseline hard state $L_X \sim 10^{36}$ erg s$^{-1}$. No clear X-ray spectral changes are associated with this factor of 10 radio variability. At all detected epochs X1850–087 has a flat-to-inverted radio spectral index, more consistent with the partially absorbed optically thick synchrotron of a compact jet rather than evolving optically thick to thin emission associated with transient expanding synchrotron blobs. If the radio emission in X1850–087 is indeed due to a compact jet, then it is plausibly being launched and quenched in the hard state on timescales as short as a few days. Future radio monitoring of X1850–087 could help elucidate the conditions under which compact jets are produced around hard state accreting neutron stars.

## 5.4 The MAVERIC Survey: A Radio Imaging Catalog of Seven Galactic Globular Clusters from Karl G. Jansky Very Large Array

Chapter four shows our radio imaging of the final seven globular cluster observations of the MAVERIC Survey. This survey has provided the first deep radio continuum images of accreting compact sources in Galactic globular clusters. We present stacked primary beam corrected images of each cluster that was taken in 2018. We also present a radio source catalog of one of the clusters, NGC 6522 with their radio flux densities and spectral index measurements.

## 5.5 Future Directions

Deep radio observations from our team's MAVERIC Survey has led us to discover intriguing accretion and outflow dynamics of accreting neutron stars in globular clusters. In this thesis, we have shown that accreting neutron stars have behaviors that are not easily explained with standard accretion theory and opens up numerous questions:

*Can neutron stars produce jets at very low accretion rates?* Black holes are shown to be brighter in the X-ray and more radio-loud than neutron stars at almost all accretion rates. At very low accretion rates ($L_X < 10^{34} ergs^{-1}$), neutron stars are absent (shown in the radio/X-ray correlation plane in Figure 1.3) and begs the question of whether these systems can produce jets at these low rates? One possible key in answering this question is using stacked observations of quiescent, transient neutron star X-ray binaries in globular clusters that are readily available in the MAVERIC Survey to see if these sources are detected in our radio continuum images.

*What is the cause of a neutron star's radio variability?* In this thesis, we show that accreting neutron stars can show immense radio variability in both transient and persistently accreting systems. Previous studies have tried to implement physical properties that would explain the wide variety of behaviors we see in accreting neutron star LMXBs but none have been conclusive. Possible high-cadence radio and X-ray observations can aid us in characterizing what is driving this radio variability, as such has done for other neutron star systems like Aql X-1.

*What is the extent of black holes and neutron stars population in globular clusters?* Studying black holes and neutron stars in globular clusters and their connection has many broader implications in astronomy. The detections of binary black hole systems as gravitational wave sources has sparked interests in finding more black holes in globular clusters as dynamical interactions in the core leads to the formation of these systems. Creating theoretical models to produce and predict current properties of globular clusters is vital to understand the origin and possible formation of these systems. Some clusters are known to host many black holes candidates and neutron star systems, therefore continued observations of these compact objects are necessary to understand their relationship with one another.

Answering these questions have long-lasting impacts of the field of neutron stars and compact objects in general, for understanding their accretion behavior and how it impacts the jet production/outflow, and the environments in which they populate in. This thesis only provides a glimpse into the wealth of information from the MAVERIC Survey and provides proof that deep radio studies of compact objects are much needed.

# BIBLIOGRAPHY

# BIBLIOGRAPHY

Alpar M. A., Cheng A. F., Ruderman M. A., Shaham J., 1982, , 300, 728

Andersen B. C., Ransom S. M., 2018, , 863, L13

Arnason R. M., Sivakoff G. R., Heinke C. O., Cohn H. N., Lugger P. M., 2015, , 807, 52

Arnaud K. A., 1996, in ASP Conf. Ser. 101: Astronomical Data Analysis Software and Systems V. p. 17

Astropy Collaboration et al., 2013, , 558, A33

Bahramian A., et al., 2014, , 780, 127

Bahramian A., et al., 2018, Radio/X-ray correlation database for X-ray binaries, doi:10.5281/zenodo.1252036, `https://doi.org/10.5281/zenodo.1252036`

Bałucińska-Church M., Church M. J., Smale A. P., 2004, , 347, 334

Baumgardt H., Hilker M., 2018, , 478, 1520

Bhattacharya D., van den Heuvel E. P. J., 1991, , 203, 1

Blackburn J. K., 1995, in Shaw R. A., Payne H. E., Hayes J. J. E., eds, Astronomical Society of the Pacific Conference Series Vol. 77, Astronomical Data Analysis Software and Systems IV. p. 367

Blandford R. D., Königl A., 1979, , 232, 34

Blandford R. D., Znajek R. L., 1977, , 179, 433

Bloser P. F., Grindlay J. E., Kaaret P., Zhang W., Smale A. P., Barret D., 2000, , 542, 1000

Bogdanov S., et al., 2018, , 856, 54

Bond H. E., Bellini A., Sahu K. C., 2020, , 159, 276

Burrows D. N., et al., 2005, , 120, 165

CASA Team et al., 2022, , 134, 114501

Cadelano M., Ransom S. M., Freire P. C. C., Ferraro F. R., Hessels J. W. T., Lanzoni B., Pallanca C., Stairs I. H., 2018, , 855, 125

Carotenuto F., et al., 2021, ,

Cartwright T. F., Engel M. C., Heinke C. O., Sivakoff G. R., Berger J. J., Gladstone J. C., Ivanova N., 2013, , 768, 183

Chen H.-L., Tauris T. M., Han Z., Chen X., 2021, , 503, 3540

Chomiuk L., Strader J., Maccarone T. J., Miller-Jones J. C. A., Heinke C., Noyola E., Seth A. C., Ransom S., 2013, , 777, 69

Chou Y., Grindlay J. E., 2001, , 563, 934

Christian D. J., Swank J. H., 1997, , 109, 177

Clark G. W., 1975, , 199, L143

Coppejans D. L., Knigge C., 2020, , 89, 101540

Corbel S., Fender R. P., Tzioumis A. K., Nowak M., McIntyre V., Durouchoux P., Sood R., 2000, , 359, 251

Corbel S., Coriat M., Brocksopp C., Tzioumis A. K., Fender R. P., Tomsick J. A., Buxton M. M., Bailyn C. D., 2013, , 428, 2500

Coriat M., et al., 2011, , 414, 677

Davis J. E., 2001, , 562, 575

Deller A. T., et al., 2015, , 809, 13

Díaz Trigo M., Migliari S., Miller-Jones J. C. A., Rahoui F., Russell D. M., Tudor V., 2017, , 600, A8

Dieball A., Knigge C., Zurek D. R., Shara M. M., Long K. S., Charles P. A., Hannikainen D. C., van Zyl L., 2005, , 634, L105

Engel M. C., Heinke C. O., Sivakoff G. R., Elshamouty K. G., Edmonds P. D., 2012, , 747, 119

Fender R., Kuulkers E., 2001, Monthly Notices of the Royal Astronomical Society, 324, 923

Ferraro F. R., D'Amico N., Possenti A., Mignani R. P., Paltrinieri B., 2001, , 561, 337

Fomalont E. B., Geldzahler B. J., Bradshaw C. F., 2001, , 553, L27

Fruchter A. S., Taylor J. H., Backer D. C., Clifton T. R., Foster R. S., 1988, , 331, 53

Fruscione A., et al., 2006, in Society of Photo-Optical Instrumentation Engineers (SPIE) Conference Series. p. 62701V, doi:10.1117/12.671760

Gaia Collaboration et al., 2018, , 616, A1

Gallo E., Fender R. P., Pooley G. G., 2003, , 344, 60

Gallo E., Fender R. P., Miller-Jones J. C. A., Merloni A., Jonker P. G., Heinz S., Maccarone T. J., van der Klis M., 2006, , 370, 1351

Gallo E., Degenaar N., van den Eijnden J., 2018, , 478, L132

Galloway D. K., Özel F., Psaltis D., 2008, , 387, 268

Gehrels N., et al., 2004, , 611, 1005

Greisen E. W., 2003, in Heck A., ed., Astrophysics and Space Science Library Vol. 285, Information Handling in Astronomy - Historical Vistas. p. 109, doi:10.1007/0-306-48080-8˙7

Grindlay J., Gursky H., Schnopper H., Parsignault D. R., Heise J., Brinkman A. C., Schrijver J., 1976, , 205, L127

Gusinskaia N. V., et al., 2017, , 470, 1871

Gusinskaia N. V., et al., 2020a, , 492, 1091

Gusinskaia N. V., et al., 2020b, , 492, 2858

Hancock P. J., Murphy T., Gaensler B. M., Hopkins A., Curran J. R., 2012, , 422, 1812

Hancock P. J., Trott C. M., Hurley-Walker N., 2018, Publications of the Astronomical Society of Australia, 35, e011

Hannikainen D. C., Hunstead R. W., Campbell-Wilson D., Sood R. K., 1998, , 337, 460

Hannikainen D. C., Charles P. A., van Zyl L., Kong A. K. H., Homer L., Hakala P., Naylor T., Davies M. B., 2005, , 357, 325

Harris C. R., et al., 2020, Nature, 585, 357

Heinke C. O., Edmonds P. D., Grindlay J. E., 2001, , 562, 363

Heinke C. O., Grindlay J. E., Lloyd D. A., Edmonds P. D., 2003, , 588, 452

Heinke C. O., Cohn H. N., Lugger P. M., 2009, , 692, 584

Heinke C. O., Ivanova N., Engel M. C., Pavlovskii K., Sivakoff G. R., Cartwright T. F., Gladstone J. C., 2013, , 768, 184

Hertz P., Wood K. S., 1985, , 290, 171

Hewish A., Bell S. J., Pilkington J. D. H., Scott P. F., Collins R. A., 1968, , 217, 709

Hill A. B., et al., 2011, , 415, 235

Hjellming R. M., et al., 1990, , 365, 681

Hobbs G., Lorimer D. R., Lyne A. G., Kramer M., 2005, , 360, 974

Homer L., Charles P. A., Naylor T., van Paradijs J., Auriere M., Koch-Miramond L., 1996, , 282, L37

Huang C.-Y., Wu Q., Wang D.-X., 2014, , 440, 965

Hulse R. A., Taylor J. H., 1975, , 195, L51

Hunter J. D., 2007, Computing In Science & Engineering, 9, 90

Ilovaisky S. A., Auriere M., Koch-Miramond L., Chevalier C., Cordoni J.-P., Crowe R. A., 1993, , 270, 139

Ioannou Z., van Zyl L., Naylor T., Charles P. A., Margon B., Koch-Miramond L., Ilovaisky S., 2003, , 399, 211

Ivanova N., Rasio F. A., Lombardi Jr. J. C., Dooley K. L., Proulx Z. F., 2005, , 621, L109

Ivanova N., Heinke C. O., Rasio F., 2007, Proceedings of the International Astronomical Union, 3, 316–320

Ivanova N., Heinke C. O., Rasio F. A., Belczynski K., Fregeau J. M., 2008, , 386, 553

Jaodand A. D., 2019, PhD thesis, University of Amsterdam

Jonker P. G., van der Klis M., Homan J., Wijnands R., van Paradijs J., Méndez M., Kuulkers E., Ford E. C., 2000, , 531, 453

Jonker P. G., Wijnands R., van der Klis M., 2004, , 349, 94

Katz J. I., 1975, , 253, 698

Kiel P. D., Hurley J. R., Bailes M., Murray J. R., 2008, , 388, 393

King I. R., Anderson J., Cool A. M., Piotto G., 1998, , 492, L37

Kirsten F., Vlemmings W., Freire P., Kramer M., Rottmann H., Campbell R. M., 2014, , 565, A43

Kitamoto S., Tsunemi H., Roussel-Dupre D., 1992, , 391, 220

Kulkarni S. R., Narayan R., Romani R. W., 1990, , 356, 174

Kuulkers E., den Hartog P. R., in't Zand J. J. M., Verbunt F. W. M., Harris W. E., Cocchi M., 2003, , 399, 663

Lasota J.-P., 2001, , 45, 449

Lehto H. J., Machin G., McHardy I. M., Callanan P., 1990, , 347, 49

Li K.-L., Strader J., Miller-Jones J. C. A., Heinke C. O., Chomiuk L., 2020, , 895, 89

Ludlam R. M., et al., 2019, , 883, 39

Lyne A. G., et al., 1990, , 347, 650

Maccarone T. J., 2003, , 409, 697

Maccarone T. J., Long K. S., Knigge C., Dieball A., Zurek D. R., 2010, , 406, 2087

Maccarone T. J., van den Eijnden J., Russell T. D., Degenaar N., 2020, , 499, 957

Machin G., Lehto H. J., McHardy I. M., Callanan P. J., Charles P. A., 1990, , 246, 237

McKinney W., 2010, in van der Walt S., Millman J., eds, Proceedings of the 9th Python in Science Conference. pp 51 – 56

McMullin J. P., Waters B., Schiebel D., Young W., Golap K., 2007, in Shaw R. A., Hill F., Bell D. J., eds, Astronomical Society of the Pacific Conference Series Vol. 376, Astronomical Data Analysis Software and Systems XVI. p. 127

Merloni A., Heinz S., di Matteo T., 2003, , 345, 1057

Migliari S., Fender R. P., 2006, , 366, 79

Migliari S., Fender R. P., Rupen M., Wachter S., Jonker P. G., Homan J., van der Klis M., 2004, , 351, 186

Migliari S., et al., 2010, , 710, 117

Migliari S., Miller-Jones J. C. A., Russell D. M., 2011, , 415, 2407

Miller-Jones J. C. A., et al., 2010, , 716, L109

Miller-Jones J. C. A., et al., 2012, , 421, 468

Miller-Jones J. C. A., et al., 2015, , 453, 3918

Muñoz-Darias T., Fender R. P., Motta S. E., Belloni T. M., 2014, , 443, 3270

Mukai K., Smale A. P., 2000, , 533, 352

NASA High Energy Astrophysics Science Archive Research Center 2014, HEAsoft: Unified Release of FTOOLS and XANADU, Astrophysics Source Code Library (ascl:1408.004)

Negoro H., et al., 2016, , 68, S1

Nelemans G., Jonker P. G., 2010, , 54, 87

Nelson L. A., Rappaport S. A., Joss P. C., 1986, , 304, 231

Paduano A., et al., 2021, ,

Panurach T., et al., 2021, , 923, 88

Papitto A., et al., 2013, , 501, 517

Parmar A. N., Oosterbroek T., Sidoli L., Stella L., Frontera F., 2001, , 380, 490

Patruno A., Watts A. L., 2021, Astrophysics and Space Science Library, 461, 143

Pavlinsky M. N., Grebenev S. A., Sunyaev R. A., 1994, , 425, 110

Perera B. B. P., et al., 2017, , 468, 2114

Plotkin R. M., et al., 2017, , 848, 92

Plummer M., 2012, JAGS: Just Another Gibbs Sampler, Astrophysics Source Code Library, record ascl:1209.002 (ascl:1209.002)

Pooley D., Homan J., 2013, The Astronomer's Telegram, 5490, 1

Pooley D., et al., 2003, , 591, L131

Predehl P., Hasinger G., Verbunt F., 1991, , 246, L21

Priedhorsky W., Terrell J., 1984, , 284, L17

Prodan S., Murray N., 2012, , 747, 4

Radhakrishnan V., Srinivasan G., 1982, Current Science, 51, 1096

Rappaport S., Nelson L. A., Ma C. P., Joss P. C., 1987, , 322, 842

Ratti E. M., et al., 2012, , 423, 2656

Revnivtsev M., Mereghetti S., 2015, , 191, 293

Roberts M. S. E., 2013, in van Leeuwen J., ed., IAU Symposium Vol. 291, Neutron Stars and Pulsars: Challenges and Opportunities after 80 years. pp 127–132 (`arXiv:1210.6903`), doi:10.1017/S174392131202337X

Rodriguez C. L., Morscher M., Pattabiraman B., Chatterjee S., Haster C.-J., Rasio F. A., 2015, Physical Review Letters, 115, 051101

Rushton A. P., et al., 2016, , 463, 628

Russell T. D., Degenaar N., Wijnands R., van den Eijnden J., Gusinskaia N. V., Hessels J. W. T., Miller-Jones J. C. A., 2018, , 869, L16

Russell T. D., et al., 2021, arXiv e-prints, p. arXiv:2107.12491

Saji S., et al., 2016, , 68, S15

Sault R. J., Teuben P. J., Wright M. C. H., 1995, in Shaw R. A., Payne H. E., Hayes J. J. E., eds, Astronomical Society of the Pacific Conference Series Vol. 77, Astronomical Data Analysis Software and Systems IV. p. 433 (`arXiv:astro-ph/0612759`)

Seward F. D., Page C. G., Turner M. J. L., Pounds K. A., 1976, , 175, 39P

Shakura N. I., Sunyaev R. A., 1973, , 24, 337

Shishkovsky L., et al., 2018, , 855, 55

Shishkovsky L., et al., 2020, , 903, 73

Sidoli L., La Palombara N., Oosterbroek T., Parmar A. N., 2005, Astronomy and Astrophysics, 443, 223

Sidoli L., La Palombara N., Oosterbroek T., Parmar A. N., 2008, , 488, 249

Sigurdsson S., Hernquist L., 1993, , 364, 423

Sivakoff G. R., Heinke C. O., Miller-Jones J. C. A., Altamirano D., Kuulkers E., Morii M., 2011, The Astronomer's Telegram, 3393, 1

Smak J., 1984, , 34, 161

Spitzer Lyman J., 1969, , 158, L139

Stacey W. S., Heinke C. O., Cohn H. N., Lugger P. M., Bahramian A., 2012, , 751, 62

Stella L., Priedhorsky W., White N. E., 1987, , 312, L17

Strader J., Chomiuk L., Maccarone T. J., Miller-Jones J. C. A., Seth A. C., 2012a, , 490, 71

Strader J., Chomiuk L., Maccarone T. J., Miller-Jones J. C. A., Seth A. C., Heinke C. O., Sivakoff G. R., 2012b, , 750, L27

Strohmayer T. E., et al., 2019, , 878, L27

Suvorov A. G., 2021, , 503, 5495

Tetarenko A. J., et al., 2016, , 460, 345

Tetarenko A. J., et al., 2018, , 854, 125

Tremou E., et al., 2018, , 862, 16

Tudor V., et al., 2017, , 470, 324

Tudor V., et al., 2022, ,

Tudose V., Fender R. P., Linares M., Maitra D., van der Klis M., 2009, , 400, 2111

Urquhart R., et al., 2020, , 904, 147

Vasiliev E., 2019, , 484, 2832

Vats S., Wijnands R., Parikh A. S., Ootes L., Degenaar N., Page D., 2018, , 477, 2494

Verner D. A., Ferland G. J., Korista K. T., Yakovlev D. G., 1996, , 465, 487

White N. E., Angelini L., 2001, , 561, L101

Wijnands R., van der Klis M., 1998, , 394, 344

Wijnands R., Degenaar N., Armas Padilla M., Altamirano D., Cavecchi Y., Linares M., Bahramian A., Heinke C. O., 2015, , 454, 1371

Wilms J., Allen A., McCray R., 2000, , 542, 914

Wilson-Hodge C. A., et al., 2018, The Astrophysical Journal, 863, 9

Ye C. S., Kremer K., Chatterjee S., Rodriguez C. L., Rasio F. A., 2019, , 877, 122

Ye C. S., Kremer K., Rodriguez C. L., Rui N. Z., Weatherford N. C., Chatterjee S., Fragione G., Rasio F. A., 2022, , 931, 84

Zdziarski A. A., Wen L., Gierliński M., 2007, , 377, 1006

Zhang L., et al., 2020, , 905, L8

Zhao Y., et al., 2020, , 493, 6033

Zurek D. R., Knigge C., Maccarone T. J., Dieball A., Long K. S., 2009, , 699, 1113

in't Zand J. J. M., Verbunt F., Heise J., et al. 1998, , 329, L37

in't Zand J. J. M., et al., 2003a, , 406, 233

in't Zand J. J. M., Strohmayer T. E., Markwardt C. B., Swank J., 2003b, , 409, 659

in't Zand J. J. M., Jonker P. G., Markwardt C. B., 2007, , 465, 953

in't Zand J. J. M., Kries M. J. W., Palmer D. M., Degenaar N., 2019, , 621, A53

Šimon V., 2003, , 405, 199

van Paradijs J., 1996, , 464, L139

van Zyl L., Charles P. A., Arribas S., Naylor T., Mediavilla E., Hellier C., 2004a, , 350, 649

van Zyl L., Ioannou Z., Charles P. A., Naylor T., 2004b, , 428, 935

van den Berg M., 2020, in Bragaglia A., Davies M., Sills A., Vesperini E., eds, Vol. 351, Star Clusters: From the Milky Way to the Early Universe. pp 367–376 (`arXiv:1910.07595`), doi:10.1017/S1743921319007981

van den Eijnden J., Degenaar N., Russell T. D., Miller-Jones J. C. A., Wijnands R., Miller J. M., King A. L., Rupen M. P., 2018a, , 473, L141

van den Eijnden J., Degenaar N., Russell T. D., Wijnands R., Miller-Jones J. C. A., Sivakoff G. R., Hernández Santisteban J. V., 2018b, Nature, 562, 233–235

van den Eijnden J., Degenaar N., Russell T. D., Hernández Santisteban J. V., Wijnands R., Miller-Jones J. C. A., Rouco Escorial A., Sivakoff G. R., 2019, , 483, 4628

van den Eijnden J., et al., 2021, arXiv e-prints, p. arXiv:2107.05286